



저작자표시-동일조건변경허락 2.0 대한민국

이용자는 아래의 조건을 따르는 경우에 한하여 자유롭게

- 이 저작물을 복제, 배포, 전송, 전시, 공연 및 방송할 수 있습니다.
- 이차적 저작물을 작성할 수 있습니다.
- 이 저작물을 영리 목적으로 이용할 수 있습니다.

다음과 같은 조건을 따라야 합니다:



저작자표시. 귀하는 원저작자를 표시하여야 합니다.



동일조건변경허락. 귀하가 이 저작물을 개작, 변형 또는 가공했을 경우에는, 이 저작물과 동일한 이용허락조건하에서만 배포할 수 있습니다.

- 귀하는, 이 저작물의 재이용이나 배포의 경우, 이 저작물에 적용된 이용허락조건을 명확하게 나타내어야 합니다.
- 저작권자로부터 별도의 허가를 받으면 이러한 조건들은 적용되지 않습니다.

저작권법에 따른 이용자의 권리는 위의 내용에 의하여 영향을 받지 않습니다.

이것은 [이용허락규약\(Legal Code\)](#)을 이해하기 쉽게 요약한 것입니다.

[Disclaimer](#)

이학박사 학위논문

**Study of Chemical Reactions on  
Graphene Surface using Infrared  
Scattering-type Scanning Near-field  
Optical Microscopy**

적외선 산란형 근접장 주사 광학 현미경을 이용한  
그래핀 표면 위 화학반응 연구

지도교수 : 김 지 환

2020 년 11 월

서울대학교 대학원  
화학부 물리화학전공

정 규 일

# Study of Chemical Reactions on Graphene Surface using Infrared Scattering-type Scanning Near-field Optical Microscopy

지도교수 김 지 환

이 논문을 이학박사 학위논문으로 제출함  
2020 년 11 월

서울대학교 대학원  
화학부 물리화학전공  
정 규 일

정규일의 이학박사 학위논문을 인준함  
2020 년 11 월

위 원 장            홍 병 희            (인)

부위원장            김 지 환            (인)

위 원            류 순 민            (인)

위 원            이 남 기            (인)

위 원            임 종 우            (인)

# **Abstract**

## **Study of Chemical Reactions on Graphene Surface using Infrared Scattering-type Scanning Near-field Optical Microscopy**

**Gyouil Jeong**

**Department of chemistry, Physical chemistry**

**Seoul National University**

This thesis focuses on chemical reaction on graphene surface using atomic force microscopy (AFM) based infrared-scattering type scanning near field optical microscopy (IR-sSNOM).

Various studies have been conducted for the unique physical and chemical properties of graphene surface. Accompanied by such advancements, particularly, multi-layer graphene was spotlighted for its facile tunability of bandgap that can be controlled by stacking angles, external electric field, or chemical doping. However, the general technique used to analyze graphene surface, such as Infrared spectroscopy, has fatal limitation. It is impossible to study nanoscopic chemical reactions on graphene surface due to Abbe's diffraction limit. Regretfully, Raman spectroscopy, which is most commonly used for graphene analysis, also has many

limitations. Moreover, this tool only perceives changes of the D, G and 2D band spectra hence fails to capture direct chemical reaction product information.

From this point of view, I have two main reasons to pursue this study. First, as a technical point of view, IR-sSNOM is known for its high sensitive nano resolution. It is possible to get IR spectrum of graphene domain less than 10  $\mu\text{m}$ . Additionally, there is no big limitation in sample condition unlike scanning tunneling microscope. In this respect, this technique is ideal tool to analyze graphene surface reaction. Secondly, graphene surface reaction study is worth to investigate as application of electronic graphene as well as prototypical model for organic chemistry. Form this model system study, it is possible to understand pi-pi interactive mechanisms but also catalytic mechanisms of graphene. I believe studying graphene surface reaction will bring new insight to chemistry field

**Keyword:** Infrared scattering-type scanning near-field optical microscopy, Plasmon, Graphene, Moiré-pattern, Redox reaction, CO<sub>2</sub> intercalation

**Student Number:** 2014-21226

## - Table of contents -

### **Chapter 1: Introduction to scattering-type scanning near-field optical microscopy**

- 1.1 Diffraction limit in classical optical microscopy
- 1.2 Nanoscale imaging
- 1.3 Scattering-type near-field optical microscopy
- 1.4 Point-dipole Modeling for IR s-SNOM
- 1.5 Interferometric detection
  - 1.5.1 Homodyne interferometric detection
  - 1.5.2 Pseudo-heterodyne detection
- 1.6 References

### **Chapter 2: Introduction to graphene surface chemistry**

- 2.1 Graphene Raman spectroscopy
- 2.2 Graphene surface chemistry
- 2.3 Moiré-patterned graphene
- 2.4 Reference

### **Chapter 3: Nanoscale visualization of multilayer graphene**

#### **Mapping of Bernal and non-Bernal stacking domains in bilayer graphene using infrared nanoscopy**

- 3.1.1 Introduction
- 3.1.2 Experiment
- 3.1.3 Results and discussion

3.1.4 Conclusion

3.1.5 Reference

**Narrow infrared resonance of commensurate-incommensurate transition for tetramer graphene on hexagonal boron nitride**

4.1.1 Introduction

4.1.2 Experiment

4.1.3 Results and discussion

4.1.4 Conclusion

**Chapter 4: Studies of selective chemical reaction on graphene surface**

**Stacking-specific reversible oxidation of bilayer graphene**

5.1.1 Introduction

5.1.2 Experiment

5.1.3 Results and discussion

5.1.4 Conclusion

5.1.5 Reference

**Infrared nano-spectroscopy study on oxidized graphene surface**

6.1.1 Introduction

6.1.2 Experiment

6.1.3 Results and discussion

6.1.4 Conclusion

7.1.5 Reference

**Reversible multilayer CO<sub>2</sub> loading in bilayer graphene**

7.1.1 Introduction

- 7.1.2 Experiment
- 7.1.3 Results and discussion
- 7.1.4 Conclusion
- 7.1.5 Reference

## **Chapter 1:**

# **Introduction to scattering-type scanning near-field optical microscopy**

## 1.1 Diffraction limit in classical optical microscopy

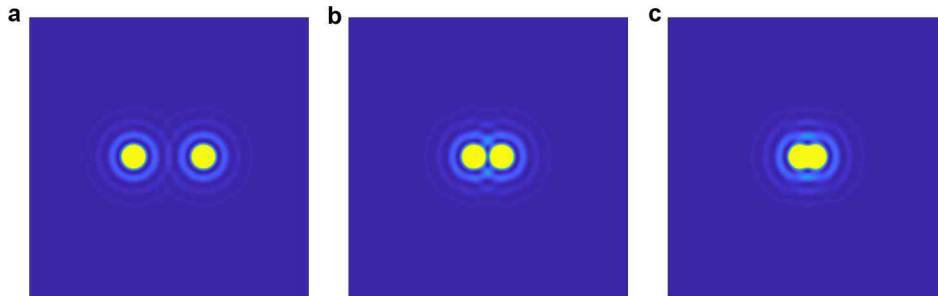


**Figure 1.1.** Abbe diffraction limit on spatial (optical) resolution of general light microscopy. **a**, resolvable two light sources. **b**, Rayleigh's criteria. **c**, Sparrow's criteria resolution limit.

Conventional optical microscopy uses propagating electromagnetic waves such as visible light to investigate samples. Usually, this image is visualized with the help of lenses or objectives. In general case, the image we get can be much larger than the original object actual size, revealing small specific characteristic feature that cannot be seen by human eye. At the end of the 19th century, to analyze this phenomenon, E. Abbe and Lord Rayleigh derived a criterion for the diffraction-limited spatial resolution of an optical microscope<sup>1</sup>.

$$\Delta x_{min} = 0.61 \frac{\lambda}{n \sin \xi} = 0.61 \frac{\lambda}{N_A}$$

Where,  $\Delta x$  is minimum distance between the two image point sources (object) at which they can still be unambiguously resolved.  $\lambda$  is the wavelength of

the light used for imaging, and  $\xi$  is the half-angle of the light cone detected by the objective.  $N_A = n \sin(\theta)$  is the numerical aperture and  $n$  is the refractive index of the medium surrounding. If we use largest NA objectives (oil  $n=1.51$ ), maximum spatial resolution of conventional optical imaging systems is  $\Delta x_{min} \cong \lambda/2$ , which for visible light is around  $\Delta x_{min} \cong 300\sim 400 \text{ nm}$ . If light of the mid-infrared spectral regime, such as quantum cascade laser, is used, spatial resolution is at least in the order of several micrometers.

## 1.2 Nanoscale imaging

To investigate samples that are smaller than the spatial resolution limit of optical microscopy, a variety of techniques have been developed. There are two approaches to overcome limit<sup>2,3</sup>. One is to use smaller wavelength such as electrons and ions for imaging. These light is much smaller than size of an atom, enabling atomic resolution imaging. However, these techniques still have diffraction limit, also have critical drawback, which is that these techniques require higher energy to achieve high resolution. Too large energy often leads to sample damaging<sup>4</sup>. Also these systems usually require high vacuum condition. For biochemistry field, fluorescence microscopy<sup>2,5,6</sup> has been developed to overcome the diffraction limit. In general, dye molecules labelling<sup>7</sup> such as fluorescent markers allow for selective mapping of different sample components. Conventionally, Fluorescent markers can be excited by certain wavelength and usually emit lower energy light. By combining complicated illumination and detection optics systems with confocal fluorescence

microscopy<sup>8</sup>, fluorescence imaging below diffraction limit can be achieved. However, these techniques require dye molecules and could possibly lead to sample contamination. Another kind of special microscopy techniques that enables to break the limitation are Scanning Probe Microscopy. The first SPM tool name is scanning Tunneling Microscopy (STM) and was invented in 1982<sup>9,10</sup>. In STM, a sharp metallic tip is used with a potential and scanned across sample surface with typical distances of less than 1 nm. Commonly, they detect tunneling current between the tip and the sample when the tip is close to the sample surface. However, this technique requires conductive sample<sup>10</sup>. To overcome this limitation and to detect variety samples, Atomic Force Microscopy (AFM) was developed<sup>11,12</sup>. This AFM is also uses a sharp tip like STM. During scanning sample surface, this technique extract mechanical interaction forces between tip and sample by distance control system. (feedback system) For this reason, long flexible cantilever is suitable for AFM. Figure 1.1 provides a schematic illustration of a typical AFM setup.

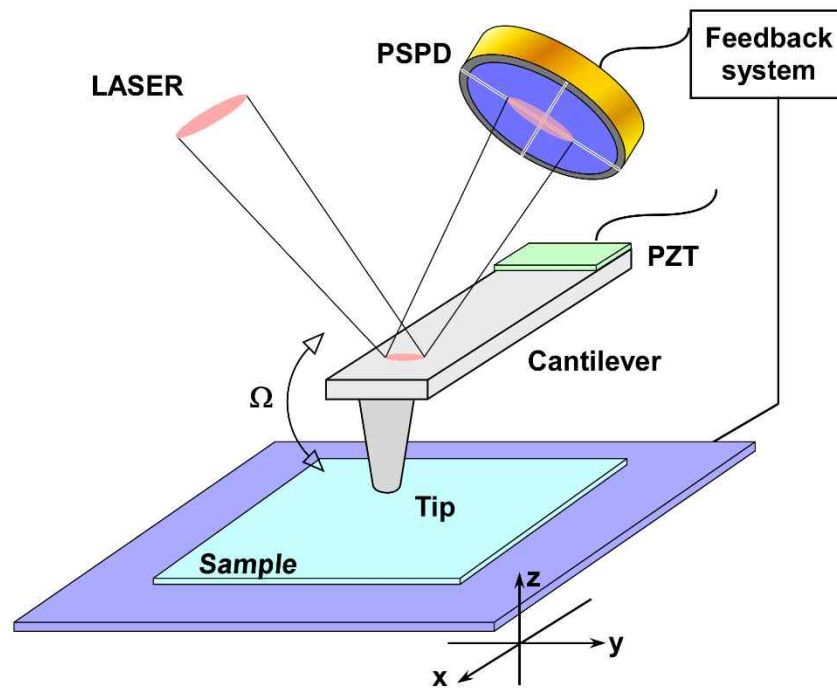


**Figure 1.2. Illustration of a typical AFM setup.** A light reaching at the cantilever edge is deflected to PSPD. This deflected signal is used in a feedback loop to control AFM tip distance from the sample surface.

When an AFM tip approaches to a sample surface, there are two main important interaction forces<sup>13</sup>. One is attractive force and another is repulsive force. If the tip and the sample is not too close, attractive coulomb forces occurs, causing the cantilever to bend towards the sample, but if the tip and the sample are extremely close together, repulsive forces arise mainly from Pauli repulsion or ionic repulsion, causing the cantilever to bend in the opposite direction. Through detecting these subtle variations of AFM tip with position-sensitive photodiode, AFM can be controlled while scanning the tip across the sample. As most widely used AFM operation is tapping mode, the tip mounted on a cantilever oscillates at a mechanical resonance  $\Omega$  (typically in the range of 10-300 kHz). When the AFM tip oscillates at its resonance frequency, the oscillating system is very sensitive to external influences.

Furthermore, when tip and sample come close, AFM tip's oscillating amplitude diminishes. Via assistance of a feedback-system, tip oscillation amplitude can be controlled. However, regrettably, such microscopes allow only topographical knowledge of sample surface.

### 1.3 Scattering-type near-field optical microscopy

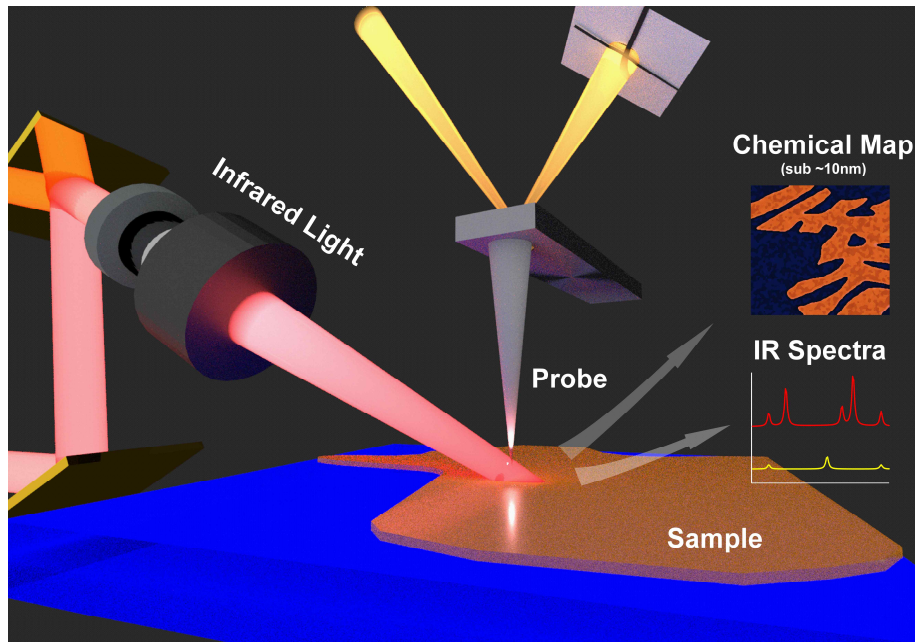
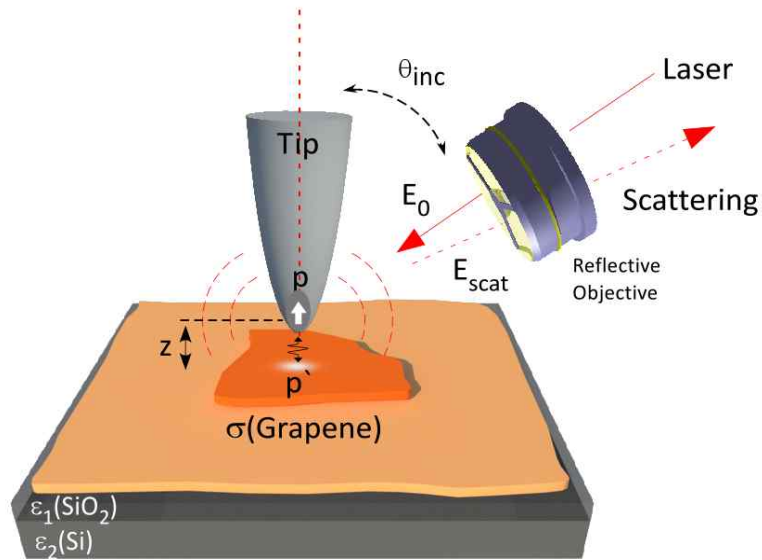


Figure 1.3. Schematic of infrared-scattering-type scanning near-field optical microscopy (IR-sSNOM) measurement.

To overcome these limitations and to get sub-wavelength resolution in optical fields, it is important to probe high spatial frequencies (more 600 kHz) contained in evanescent (near-field) waves<sup>14,15</sup>. To obtain near-field, a AFM tip has to be brought close to the sample surface at least 100 nm. The crucial thing is that the probe need to be located smaller than a wavelength because evanescent waves only exist near the sample surface. Scanning probe microscopy technique<sup>16</sup> is able to bring probe close enough to the surface to detect evanescent wave. As mentioned above, this microscope tools can control the nonmetric distance between the probe and the surface. From this adoption, scanning near-field optical microscopy<sup>17-19</sup> (SNOM) can be developed which can go beyond the diffraction limit barrier in

optical microscopy.

## 1.4 Point-dipole modeling for IR s-SNOM



**Figure 1.4. Illustration of coupled with tip–sample dipole model system.** This model is assumed that the AFM tip is supposed a small sphere with an infinitely small dipole and the tip dipole moment is  $p$  at height  $z$  above the sample surface. This tip dipole creates a mirror dipole of dipole moment.

Figure 2. sketches the essence of our sSNOM model. The conical or pyramid-shaped tip is mostly polarized along its principal axis. Thus, we assume that only the out-of-plane tensor component ( $\alpha_{zz}$ ) is non-zero. The tip-end, which is modeled as a nanosphere has a polarizability ( $\alpha$ )<sup>20</sup> of

$$\alpha = 4\pi a^3 (\epsilon_{\text{tip}} - \epsilon_1) / (\epsilon_{\text{tip}} + 2\epsilon_1) \dots (1)$$

where the  $\epsilon_{\text{tip}}$ , and  $\epsilon_1$  are dielectric constants of tip-end and vacuum, respectively. A p-polarized LASER light ( $\vec{E}_0(\vec{r})$ ) is incident on the tip sample junction system at an incident angle of  $\theta_{\text{inc}} = 60^\circ$  and with the photon momentum of  $\vec{k}_{\text{inc}}$ . The polarized light component of far-field scattering is gathered along the incident opposite direction (backward scattering).

The tip-dipole excitation can take place either directly, or via the reflection from the sample surface. Therefore, the end of AFM tip affected the incident field as:

$$\vec{E}_{\text{nc}} = (1 - r_p(\theta_{\text{inc}})e^{i2k_z \cos \theta_{\text{inc}}})\vec{E}_0(\vec{r}_{\text{tip}}) \dots (2)$$

where the  $r_p(\theta_{\text{inc}})$  is the Fresnel reflection coefficient of the sample for an incident angle of  $\theta_{\text{inc}}$  (p-polarized light). Furthermore, we can evaluate the Fresnel coefficient of graphene / SiO<sub>2</sub> / Si sample:

$$r_p = \frac{Z_1 C - Z_2 S - \sigma_r \pi \alpha C}{Z_1 C + Z_2 S + \sigma_r \pi \alpha C} \dots (3)$$

Where  $C = \cos \varphi - i \frac{Z_3}{Z_1} \sin \varphi$ ,  $S = -i \sin \varphi + \frac{Z_2}{Z_1} \cos \varphi$  and  $\varphi = k_{2z} d$ . The  $Z_i = \frac{2\pi}{\lambda} \cdot \frac{\epsilon_i}{k_{iz}}$  are the admittance of  $i = 1$  (vacuum), 2 (SiO<sub>2</sub>) and 3 (Si) media, and the  $k_{iz}$  are the out-of-plane wavevectors in  $i$ 'th media:  $k_{\vec{k}}(q) = \sqrt{\epsilon_i(\omega/c)^2 - q^2}$  ( $\text{Im}[k_{\vec{k}}] > 0$  and  $\text{Re}[k_{\vec{k}}] > 0$ ) where  $q$  and  $\omega$  are the in-plane photon momentum vector and angular frequency of light, respectively. The  $\sigma_r$  is the in-plane optical conductivity of graphene,  $\sigma$ , normalized by unit conductivity,  $\sigma_0 = \alpha/4$ . The  $\alpha$  is the fine-structure constant.

If We can assume that graphene sample is placing upon a monolithic SiO<sub>2</sub> substrate with infinite thickness, the Fresnel coefficient ( $r_p$ ) is can be simplified to:

$$r_p = -\frac{\varepsilon_2 k_{1z} - \varepsilon_1 k_{2z} + \frac{4\pi\sigma}{\omega} k_{1z} k_{2z}}{\varepsilon_2 k_{1z} + \varepsilon_1 k_{2z} + \frac{4\pi\sigma}{\omega} k_{1z} k_{2z}} \dots (4)$$

As we expand the in-plane photon momentum,  $q$ , we should pay attention that the Fresnel coefficients (eqns (3) and (4)) converges to -1. This arise from the dominant in-plane optical conductivity of graphene.

Through the dipole-image dipole interaction, the tip-dipole can be interact with the sample. This degree of interaction between tip-dipole and sample dipole can be calculated using the Green's dyadic operator,  $\vec{G}$  and the resulting effective tip dipole moment is:

$$\vec{p} = \vec{\alpha} \cdot \vec{E}_{inc}(\vec{r}_{\vec{p}}) \cdot \left(1 - \vec{\alpha} \cdot \vec{G}(\vec{r}_{\vec{p}}, \vec{r}_{\vec{p}})\right)^{-1} \dots (5)$$

The  $\vec{G}$  is consist of two terms. One is free-space ( $\vec{G}_f$ ) and the othwe is reflection ( $\vec{G}_r$ ) components. The self-interaction of the tip ( $\vec{G}(\vec{r}_{\vec{p}}, \vec{r}_{\vec{p}})$ ) is included into its polarizability in free space (see Eq. (1)). Taking the smallness of the tip radius of curvature into account, I can neglect the radiation corrections. Thus, I can include only the reflection part of the Green's function in Eq. (6), i. e.,  $\vec{G}(\vec{r}_{\vec{p}}, \vec{r}_{\vec{p}}) = \vec{G}_r(\vec{r}_{\vec{p}}, \vec{r}_{\vec{p}})$ . Recalling that the tip is polarizable only along the z-axis, the only nonzero dipole component is the z-component:

$$\vec{p} = \alpha_{zz} \cdot E_{nc,z}(\vec{r}_{\vec{p}}) \cdot \left(1 - \alpha_{zz} \vec{G}(\vec{r}_{\vec{p}}, \vec{r}_{\vec{p}})\right)^{-1} \dots (6)$$

The  $G_{r,zz}(\vec{r}_{\vec{p}}, \vec{r}_{\vec{p}})$  is calculated numerically:

$$\vec{G}_{r,zz}(\vec{r}_{\vec{p}}, \vec{r}_{\vec{p}}) = I(z) = \frac{i}{4\pi} \int_0^\infty dq r_q \frac{q^3}{k_{1z}} e^{i2k_{1z}z} \dots (7)$$

The integral of eqn (8), referred to as a weight function, determines the bounds of q's that is sampled by sSNOM probe through  $r_p(q)$ . Overall scattering except for near-field amplitude can be calculated

$$E_{scat,p} = A(1 - r_p(\theta_{nc}) e^{2ik_0 z \cos \theta_{nc}})^2 \cdot (1 - \alpha_{zz} I(z))^{-1} \dots (8)$$

where A is a constant of the position of detector. In case of the s-SNOM measurement, the amplitude signal is processed by a lock-in amplifier to eliminate unwanted signal.

The combinational signal between the  $E_{scat}$  and the demodulated signal  $s_n$  is:

$$s_n = |s_n| e^{i\psi_n} = \frac{1}{2\pi} \int_0^{2\pi} E_{scat}(z + \delta z \cos \psi) e^{i\psi} d\psi \dots (9)$$

Where z is average tip-sample distance, and  $\delta z$  is the amplitude of vertical tip-oscillation, respectively.

## 1.5 Interferometric detection

### 1.5.1 Homodyne interferometric detection

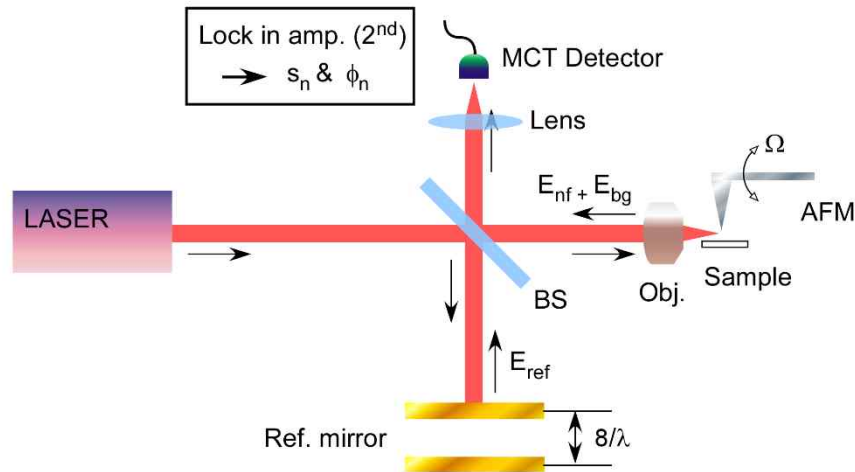


**Figure 1.5. Schematic of the homodyne interferometric detection technique.** The LASER is passing through the beam splitter (BS) and is divided into two beams. The one is reflected by reference metal mirror which is accurately controlled with in nanometer scale by piezo actuator at the forward or backward positions. Another one is focused by objective at end of AFM tip. The detected signal which is interfered with each other is derived by the lock-in amplifier for amplitude and phase of near-field signal.

Most of the scattered near-field signal ( $E_{nf}$ ) from an AFM tip sample junction is too small to detect because of large background signal ( $E_{bg}$ ). To suppress large background signal and to enhance the near-field signal intensity, the IR-sSNOM is required for interferometric amplification techniques. In general IR-sSNOM experiments, homodyne detection is powerful enough and mostly used. The major concept of homodyne detection is that the small near-field signal is interfered with reference beam ( $E_{ref}$ ) that is split off from the sample beam path by a beam splitter. Figure 1.6 It is efficient to amplify when reference beam is larger than the

large background signal. There are three beams interfered at the detector:  $E_{nf}$ ,  $E_{bg}$  and  $E_{ref}$ . Generally,  $E_{ref}$  should be larger than  $E_{bg}$  so that the modulated reference beam dominates the uncontrollable background signal.

The interference equation reads as below:

$$\begin{aligned} I &\propto E_{tot} E_{tot}^* = (E_{nf} + E_{bg} + E_{ref})(c.c.) \\ &= E_{nf}^2 + E_{bg}^2 + E_{ref}^2 + E_{bg}E_{ref}^* + E_{bg}^*E_{ref} + E_{nf}E_{bg}^* + E_{nf}^*E_{bg} + E_{nf}E_{ref}^* \\ &\quad + E_{nf}^*E_{ref} \end{aligned}$$

The  $E_{nf}$  term is too small to detect so that can be considered as negligible.

The next four terms do not relate to near field so that also, can be neglected and are thus not modulated at harmonics of the tip oscillation frequency ( $\sim$ kHz). In addition, the following two terms are negligible because reference beam,  $E_{ref}$  is tremendously larger than background signal,  $E_{bg}$ . The remaining terms can be written as such.

$$I \propto 2|E_{nf}||E_{ref}|\cos(\Delta\emptyset)$$

Where  $\Delta\emptyset$  is the relative phase between the near field light and the reference beam.

As the next step, measurement is taken at two different position of  $\Delta\emptyset$  which is

available to pull out both a value proportional to  $|E_{nf}|$  and the value of  $\Delta\phi$ .

Consider two measurements taken at some unknown  $\Delta\phi$  and  $\Delta\phi - \frac{\pi}{2}$ .

$$I_1 \propto 2|E_{nf}||E_{ref}| \cos(\Delta\phi)$$

$$I_2 \propto 2|E_{nf}||E_{ref}| \cos\left(\Delta\phi - \frac{\pi}{2}\right) = 2|E_{nf}||E_{ref}| \sin(\Delta\phi)$$

$$I_1^2 + I_2^2 \propto |E_{nf}|^2, \text{ and } \left(\frac{I_2}{I_1}\right) = \Delta\phi$$

Eventually, by measuring two certain point value and calculating the aforementioned calculations, it is possible to disassemble a value for the amplitude and phase of the near field.

### 1.5.2 Pseudo-heterodyne detection

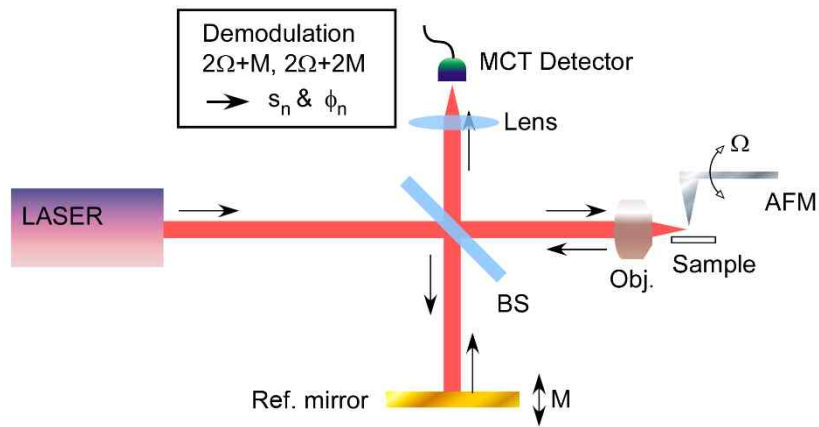


**Figure 1.6. Schematic of the pseudo-heterodyne detection technique.** the reference mirror is oscillated at frequency  $M$  for frequency modulation. Scattered near field ( $E_{nr}$ ) is modulated at frequencies  $\Omega$  to suppress background signal.

Pseudo-heterodyne detection is similar to homodyne detection in terms of utilizing a reference arm to amplify the weak near field signal. However, in pseudo-heterodyne detection, reference mirror is sinusoidally modulated. This modulation is executed by voltage applied to piezo where reference mirror is mounted. The modulated reference field formula is as follows.

$$E_{ref} = |E_{ref}| e^{j\varphi_{ref} + j\gamma \cos(Mt)} + c.c.$$

$\gamma$  is the modulated oscillating amplitude of reference mirror and  $\varphi_r$  denote original phase of the reference field.  $M$  is usually hundreds hertz oscillating frequency of the reference mirror.

To utilize the Jacobi-Anger expansion, the signal can be expressed as

$$E_r = |E_r| \sum_{m=-\infty}^{\infty} J_m(\gamma) e^{(jm M t + j\varphi_{ref} + j\frac{m\pi}{2})}$$

where,  $J_m(\gamma)$  and  $m$  denote Bessel function of the first kind and an integer. The  $m$  must be a non-zero integer in order to pull out the near-field from the background noise. The detected total interference near field signal can be expressed as,

$$\begin{aligned} I &\propto E_{tot} E_{tot}^* = (E_{nf} + E_{bg} + E_{ref})(c.c.) \\ &= E_{nf}^2 + E_{bg}^2 + E_{ref}^2 + E_{nf}E_{ref}^* + E_{bg}^*E_{ref} + E_{nf}E_{bg}^* + E_{nf}^*E_{bg} + E_{nf}E_{ref}^* \\ &\quad + E_{nf}^*E_{ref} \\ &= E_{nf}^2 + E_{bg}^2 + E_{ref}^2 + E_{nf}E_{bg}^* + E_{nf}^*E_{bg} \\ &\quad + 2 \sum_{m=-\infty}^{\infty} J_m(\gamma) |E_{bg}| |E_{ref}| e^{jm M t} \cos\left(\varphi_{bg} - \varphi_{ref} - \frac{m\pi}{2}\right) \\ &\quad + 2 \sum_{m=-\infty}^{\infty} J_m(\gamma) |E_{nf}| |E_{ref}| e^{jm M t} \cos\left(\varphi_{nf} - \varphi_{ref} - \frac{m\pi}{2}\right) \end{aligned}$$

As mentioned above, the sSNOM only needs amplified near field signal. The amplified near field signal can expand into the follows form

$$I \propto |F_n| |E_{nf}| |E_{ref}| \sum_{n=-\infty}^{\infty} \sum_{m=-\infty}^{\infty} J_m(\gamma) e^{j(n\Omega + m M)t} \cos \left( \varphi_{nf} + \varphi_n - \varphi_{ref} - \frac{m\pi}{2} \right)$$

From this interference signal, it is simple to extract only near field signal using a lock-in detection technique at the frequency of  $n\Omega + mM$ .

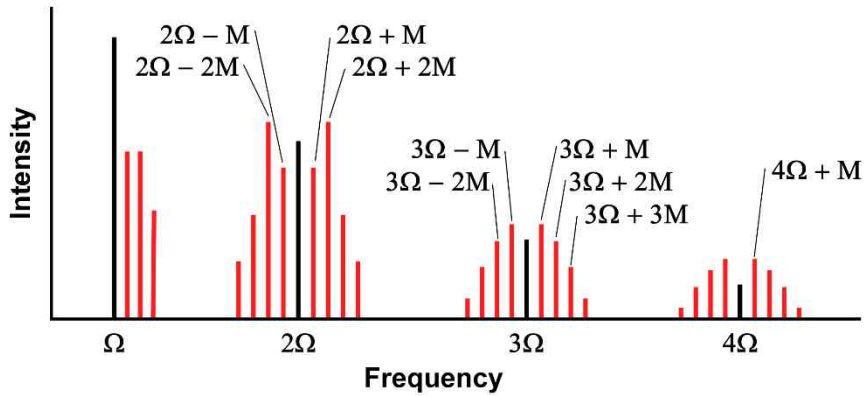


**Figure 1.7. Schematic representation of the modulated signal.** The harmonic frequency signals are split into sidebands at intervals of reference mirror frequency  $M$ .

Looking at the above equation, intensity signal is transformed to trigonometric sine and cosine at regular intervals of frequency  $m$ . Experimentally, it must be recommended that  $m$  must be small enough to get a large  $J_m(\gamma)J_m(g)$  with a certain value of  $\gamma$ . It is effective to amplify the output signal and it possible to pull out lock-in signal at the frequency of  $2\Omega + M$  ( $m = 1$ ) and at  $2\Omega + 2M$  ( $m = 2$ ). From this selection, signal at  $2\Omega + M$  and  $2\Omega + 2M$  can be expressed respectively as

$$I_{2\Omega+M} \propto |F_2| |E_{nf}| |E_{ref}| J_1(\gamma) \sin(\varphi_{nf} + \varphi_2 - \varphi_{ref})$$

$$I_{2\Omega+2M} \propto |F_2| |E_{nf}| |E_{ref}| J_2(\gamma) \cos(\varphi_{nf} + \varphi_2 - \varphi_{ref})$$

Owing to  $I_{2\Omega+M}$  and  $I_{2\Omega+2M}$  are two orthogonal terms, magnitude and phase can be easily extracted as

$$I_{2\Omega+M}^2 + I_{2\Omega+2M}^2 \propto |E_{nf}|^2, \quad \arctan\left(\frac{I_{2\Omega+2M}}{I_{2\Omega+M}}\right) = \Delta\phi$$

The main strength of pseudo-heterodyne is that it is possible to obtain the amplitude and phase of the near field in a single scan while homodyne detection not available. However, pseudo-heterodyne has critical disadvantage. Numerous actual near field signal can be neglected regrettably. Because, each side band of tip harmonic peak possess sample information about scattered near field signal while lock in amplifier processes only two of sidebands among a number of sidebands.

## 1.6 References

- 1 Dedecker, P., Hofkens, J. & Hotta, J.-i. Diffraction-unlimited optical microscopy. *Materials Today* **11**, 12-21, doi:[https://doi.org/10.1016/S1369-7021\(09\)70003-3](https://doi.org/10.1016/S1369-7021(09)70003-3) (2008).
- 2 Beyond the diffraction limit. *Nature Photonics* **3**, 361-361, doi:[10.1038/nphoton.2009.100](https://doi.org/10.1038/nphoton.2009.100) (2009).
- 3 Huang, B., Babcock, H. & Zhuang, X. Breaking the diffraction barrier: super-resolution imaging of cells. *Cell* **143**, 1047-1058, doi:[10.1016/j.cell.2010.12.002](https://doi.org/10.1016/j.cell.2010.12.002) (2010).
- 4 Cleff, C. et al. Stimulated-emission pumping enabling sub-diffraction-limited spatial resolution in coherent anti-Stokes Raman scattering microscopy. *Physical Review A* **87**, 033830, doi:[10.1103/PhysRevA.87.033830](https://doi.org/10.1103/PhysRevA.87.033830) (2013).
- 5 Jia, S., Han, B. & Kutz, J. N. Example-Based Super-Resolution Fluorescence Microscopy. *Scientific Reports* **8**, 5700, doi:[10.1038/s41598-018-24033-7](https://doi.org/10.1038/s41598-018-24033-7) (2018).
- 6 Leung, B. & Chou, K. Review of Super-Resolution Fluorescence Microscopy for Biology. *Applied spectroscopy* **65**, 967-980, doi:[10.1366/11-06398](https://doi.org/10.1366/11-06398) (2011).
- 7 Zwettler, F. U. et al. Molecular resolution imaging by post-labeling expansion single-molecule localization microscopy (Ex-SMLM). *Nature Communications* **11**, 3388, doi:[10.1038/s41467-020-17086-8](https://doi.org/10.1038/s41467-020-17086-8) (2020).
- 8 Denkova, D. et al. 3D sub-diffraction imaging in a conventional confocal configuration by exploiting super-linear emitters. *Nature Communications* **10**, 3695, doi:[10.1038/s41467-019-11603-0](https://doi.org/10.1038/s41467-019-11603-0) (2019).
- 9 Binnig, G. & Rohrer, H. Scanning tunneling microscopy. *Surface Science* **126**, 236-244, doi:[https://doi.org/10.1016/0039-6028\(83\)90716-1](https://doi.org/10.1016/0039-6028(83)90716-1) (1983).
- 10 Binnig, G. & Rohrer, H. Scanning tunneling microscopy---from birth to adolescence. *Reviews of Modern Physics* **59**, 615-625, doi:[10.1103/RevModPhys.59.615](https://doi.org/10.1103/RevModPhys.59.615) (1987).
- 11 Ohnesorge, F. & Binnig, G. True Atomic Resolution by Atomic Force

- Microscopy Through Repulsive and Attractive Forces. *Science* **260**, 1451-1456, doi:10.1126/science.260.5113.1451 (1993).
- 12 Binnig, G., Quate, C. F. & Gerber, C. Atomic Force Microscope. *Physical Review Letters* **56**, 930-933, doi:10.1103/PhysRevLett.56.930 (1986).
- 13 Hinterdorfer, P. & Dufrêne, Y. F. Detection and localization of single molecular recognition events using atomic force microscopy. *Nature Methods* **3**, 347-355, doi:10.1038/nmeth871 (2006).
- 14 Zeng, Y. et al. Manipulating Evanescent Waves in a Gradient Waveguide. *Physical Review Applied* **13**, 064049, doi:10.1103/PhysRevApplied.13.064049 (2020).
- 15 Taitt, C. R., Anderson, G. P. & Ligler, F. S. Evanescent wave fluorescence biosensors: Advances of the last decade. *Biosens Bioelectron* **76**, 103-112, doi:10.1016/j.bios.2015.07.040 (2016).
- 16 Wilde, Y. D. & Lemoine, P. A. Review of NSOM Microscopy for Materials. *AIP Conference Proceedings* **931**, 43-52, doi:10.1063/1.2799414 (2007).
- 17 Synge, E. H. XXXVIII. A suggested method for extending microscopic resolution into the ultra-microscopic region. *The London, Edinburgh, and Dublin Philosophical Magazine and Journal of Science* **6**, 356-362, doi:10.1080/14786440808564615 (1928).
- 18 Synge, E. H. XXIII. An application of piezo-electricity to microscopy. *The London, Edinburgh, and Dublin Philosophical Magazine and Journal of Science* **13**, 297-300, doi:10.1080/14786443209461931 (1932).
- 19 Pohl, D. W., Denk, W. & Lanz, M. Optical stethoscopy: Image recording with resolution  $\lambda/20$ . *Applied Physics Letters* **44**, 651-653, doi:10.1063/1.94865 (1984).
- 20 Ghimire, A., Shafran, E. & Gerton, J. M. Using a Sharp Metal Tip to Control the Polarization and Direction of Emission from a Quantum Dot. *Scientific Reports* **4**, 6456, doi:10.1038/srep06456 (2014).

## **Chapter 2:**

### **Introduction to**

### **graphene surface chemistry**

## 2.1 Graphene Raman spectroscopy

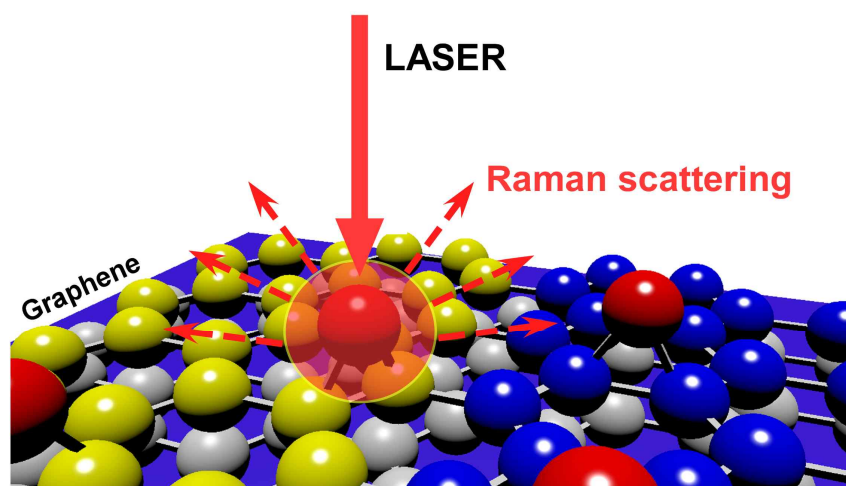


Figure 2.1. Schematic illustration of Raman scattering from the oxygen molecules adsorbed onto bilayer graphene.

Raman Spectroscopy uses relatively simple experimental equipment and can be analyzed non-destructively. In addition, Raman spectroscopy enables high-resolution analysis that is not possible with general IR spectroscopy. Using this Raman spectroscopy, it is also possible to analyze the lattice structure<sup>1</sup>, electronic<sup>2</sup>, optical<sup>2</sup>, and phonon<sup>3</sup> of carbon materials. Three-dimensional (3-d) diamond<sup>4</sup> and graphite, graphene (2-d), carbon nanotubes<sup>5</sup> (1-d), and fullerenes<sup>6</sup> (0-d) can be measured. Numerous progress research has been made in graphene field using Raman spectroscopy over the past period. In addition to general graphene research, it has been used in application fields such as doping<sup>7</sup>, strain<sup>8</sup> (stress), disorder<sup>9</sup>, chemical functionalization<sup>10</sup>, thermal conductivity<sup>11</sup>, magnetic field<sup>12</sup> and interlayer coupling<sup>13</sup>. Compared to the Raman process of other molecules, intensity of

graphene Raman spectroscopy with the resonance process is tremendously larger than that of other molecules. Mainly, this graphene Raman spectroscopy checks the R, D, G, 2D bands representatively. Changes of graphene are detected through variations of peak intensities, peak position and line shapes.

More specifically, the R (R') band<sup>14</sup> is visible when two or more layers of graphene are overlapped at an abnormal angle. The position can be seen from several positions (about  $1300\text{cm}^{-1}$  and  $1680\text{cm}^{-1}$ ) depending on the overlapping angle. The D band is a Forbidden transition<sup>15</sup>, which is not visible in perfect graphene. However, when a defect occurs, it is visible from the  $1360\text{cm}^{-1}$  position. The changes in graphene surface, such as doping, can be identified. The G band is a typical vibration motion of graphene and is seen from the  $1625\text{cm}^{-1}$ . In the case of this G band, two states are degenerated<sup>16,17</sup>. Consequently, it appears as one peak. When an influence such as doping, stain or oxidation is applied to graphene, it may appear as two peaks. The 2D band is the overtone mode<sup>18</sup> of the D band and this band is measured at  $2450\text{cm}^{-1}$ . The number of layers of graphene can be distinguished by the ratio of the G band and the 2D band<sup>19</sup>. Additionally, the order of graphene layers can be distinguished by the 2D band shape<sup>20</sup>.

## 2.2 Graphene surface chemistry

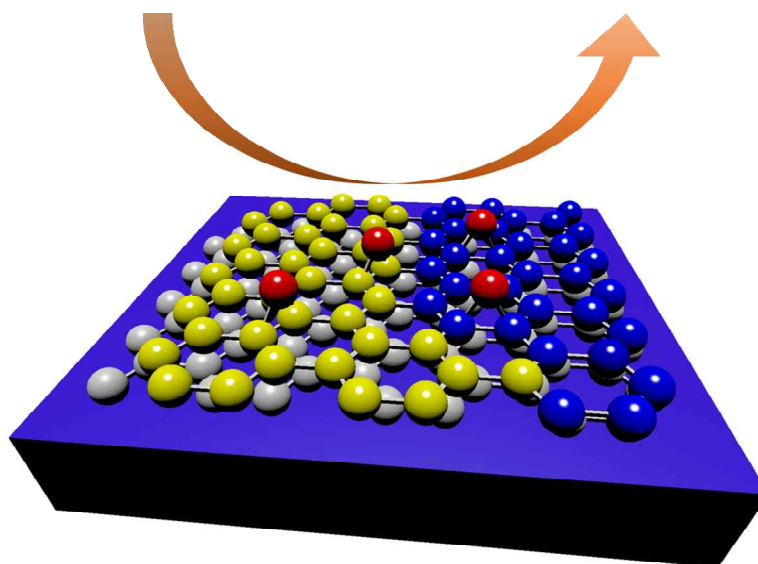


**Figure 2.2. Schematic of chemical reaction of graphene surface.** Oxidation reaction of two kind of stacking structure bilayers graphene on  $\text{SiO}_2$  substrates.

Graphene is a two-dimensional structure with carbon atoms arranged in a honeycomb lattice and is already known to be a unique properties including electronic<sup>21</sup>, optical<sup>22</sup>, thermal<sup>23</sup>, and mechanical<sup>24</sup> properties. To be easily used these unusual properties in various fields, several synthetic methods<sup>25-27</sup> of graphene-based carbon materials have been introduced. The most notable is the CVD synthesis<sup>25,28</sup> on metal substrates, an interdisciplinary technique expected to connect the academic field and industry. Besides these unique characteristics and synthesis method, there is an interesting point about graphene. it can have unique properties if the 2D structure of graphene is changed by other element such as metal<sup>29</sup>, liquids<sup>30</sup>, semiconductors<sup>31</sup>, polymers<sup>32</sup>, biomaterials<sup>33</sup>, and even ion<sup>34</sup>. In other words,

properties of graphene can be changed through physisorption<sup>35</sup> and chemical reactions such as functionalization<sup>36</sup>. On the contrary, it is also possible to know a change of the graphene surface through the change of graphene characteristics. And there are a lot of advantages that most of all, it is possible to study pi-pi interactive mechanisms<sup>37</sup> and catalytic mechanisms<sup>38</sup> through these mutual relationships graphene and changes in the surface of graphene.

However, the analytical tools used to study of chemical reaction on surface of graphene are very limited. The most commonly used technique when observing such a phenomenon is Raman spectroscopy, which detects changes in graphene itself. Alteration of graphene or graphene surface are generally detected via changes in the D, G and 2D band. Therefore, there is a large limit to the method of seeing changes in graphene itself in this way. In addition, the limit of this technique is also glaringly obvious. Since the spatial resolution is up to several hundred nanometers, there is a big limitation on graphene research. For these reasons, the need for other special spectroscopic techniques has emerged.

## 2.3 Moiré-pattern graphene

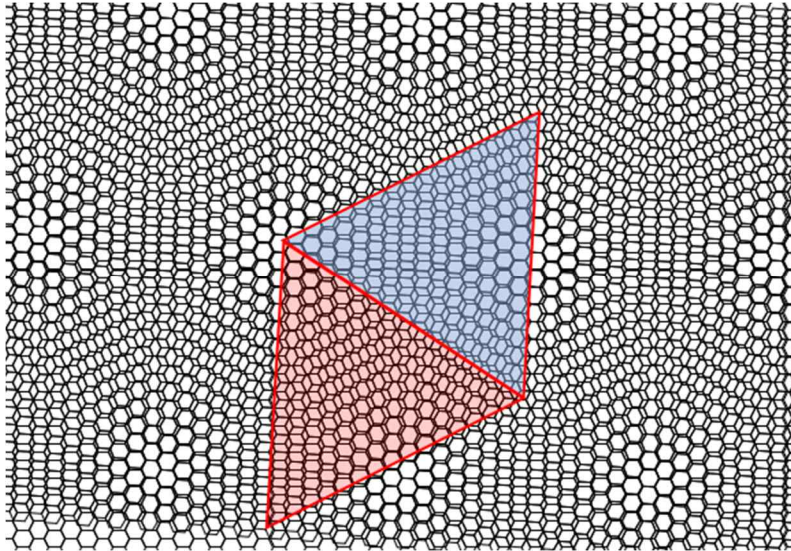


**Figure 2.3. Schematics of Moiré-pattern Graphene.** Pattern that occurs when two graphenes are overlapped. The smallest unit cell of Moiré-pattern Graphene is triangular structures.

When two relatively similar structures overlap, a new pattern is created. This pattern is called moiré-pattern<sup>39</sup>, also this word is derived from the mohair in French. When two sheets of graphene with repeating unit cells overlap, a moiré-pattern is created. Interestingly, moiré-patterned graphene may exhibit unusual properties<sup>40-42</sup> other than previously known. These distinctive properties in stacked graphene layers can be tuned by manipulating a twisted angle.

Among these moiré-patterned graphene, moiré superlattices in van der Waals (vdW) stacks of graphene and hexagonal boron nitride (h-BN) layers are tremendous attractive materials as they show superior electronic properties<sup>43,44</sup> like superconducting phase<sup>45</sup>. The main reason for this unique property is known to be the

interplay between atomic structure and electron correlations. The field of research related to this is called the twistrionics<sup>46,47</sup>, and active research is ongoing. Remarkable result is that when two layers are overlapped at specific magic angles the moiré pattern shows unique properties such as superconductivity. Also, if graphene is overlapped with a magic angle, a sharp peak associated with band-flattening near the charge-neutrality point is shown when the two van Hove singularities<sup>48,49</sup> (VHS) in the density of states (DOS) of each monolayer are merged in the angle. Also, recent studies reported that moiré flat bands are made even two Bernal stacking bilayer graphene overlapped with a specific small angle, which is twisted double bilayer graphene<sup>50-53</sup> (tDBG).

## 2.4 References

- 1 Usachov, D. Y. *et al.* Raman Spectroscopy of Lattice-Matched Graphene on Strongly Interacting Metal Surfaces. *ACS Nano* **11**, 6336-6345, doi:10.1021/acsnano.7b02686 (2017).
- 2 Wu, J.-B., Lin, M.-L., Cong, X., Liu, H.-N. & Tan, P.-H. Raman spectroscopy of graphene-based materials and its applications in related devices. *Chemical Society Reviews* **47**, 1822-1873, doi:10.1039/C6CS00915H (2018).
- 3 Cong, X. *et al.* Probing the acoustic phonon dispersion and sound velocity of graphene by Raman spectroscopy. *Carbon* **149**, 19-24, doi:<https://doi.org/10.1016/j.carbon.2019.04.006> (2019).
- 4 Krishnan, R. S. Raman Spectrum of Diamond. *Nature* **155**, 171-171, doi:10.1038/155171a0 (1945).
- 5 Hümmer, T. *et al.* Cavity-enhanced Raman microscopy of individual carbon nanotubes. *Nature Communications* **7**, 12155, doi:10.1038/ncomms12155 (2016).
- 6 Dwivedi, N. *et al.* Ultrathin Carbon with Interspersed Graphene/Fullerene-like Nanostructures: A Durable Protective Overcoat for High Density Magnetic Storage. *Scientific Reports* **5**, 11607, doi:10.1038/srep11607 (2015).
- 7 Lee, J. E., Ahn, G., Shim, J., Lee, Y. S. & Ryu, S. Optical separation of mechanical strain from charge doping in graphene. *Nature Communications* **3**, 1024, doi:10.1038/ncomms2022 (2012).
- 8 Neumann, C. *et al.* Raman spectroscopy as probe of nanometre-scale strain variations in graphene. *Nature Communications* **6**, 8429, doi:10.1038/ncomms9429 (2015).
- 9 Eckmann, A. *et al.* Probing the Nature of Defects in Graphene by Raman Spectroscopy. *Nano Letters* **12**, 3925-3930, doi:10.1021/nl300901a (2012).
- 10 Vecera, P. *et al.* Precise determination of graphene functionalization by in situ Raman spectroscopy. *Nature Communications* **8**, 15192, doi:10.1038/ncomms15192 (2017).

- 11 Malekpour, H. *et al.* Thermal Conductivity of Graphene Laminate. *Nano Letters* **14**, 5155-5161, doi:10.1021/nl501996v (2014).
- 12 Berciaud, S., Potemski, M. & Faugeras, C. Probing Electronic Excitations in Mono- to Pentalayer Graphene by Micro Magneto-Raman Spectroscopy. *Nano Letters* **14**, 4548-4553, doi:10.1021/nl501578m (2014).
- 13 Havener, R. W., Zhuang, H., Brown, L., Hennig, R. G. & Park, J. Angle-Resolved Raman Imaging of Interlayer Rotations and Interactions in Twisted Bilayer Graphene. *Nano Letters* **12**, 3162-3167, doi:10.1021/nl301137k (2012).
- 14 Berciaud, S., Ryu, S., Brus, L. E. & Heinz, T. F. Probing the Intrinsic Properties of Exfoliated Graphene: Raman Spectroscopy of Free-Standing Monolayers. *Nano Letters* **9**, 346-352, doi:10.1021/nl8031444 (2009).
- 15 Carozo, V. *et al.* Raman Signature of Graphene Superlattices. *Nano Letters* **11**, 4527-4534, doi:10.1021/nl201370m (2011).
- 16 Henni, Y. *et al.* Rhombohedral Multilayer Graphene: A Magneto-Raman Scattering Study. *Nano Letters* **16**, 3710-3716, doi:10.1021/acs.nanolett.6b01041 (2016).
- 17 Gupta, A., Chen, G., Joshi, P., Tadigadapa, S. & Eklund. Raman Scattering from High-Frequency Phonons in Supported n-Graphene Layer Films. *Nano Letters* **6**, 2667-2673, doi:10.1021/nl061420a (2006).
- 18 Cong, C., Yu, T., Saito, R., Dresselhaus, G. F. & Dresselhaus, M. S. Second-Order Overtone and Combination Raman Modes of Graphene Layers in the Range of 1690–2150  $\text{cm}^{-1}$ . *ACS Nano* **5**, 1600-1605, doi:10.1021/nn200010m (2011).
- 19 Budde, H. *et al.* Raman Radiation Patterns of Graphene. *ACS Nano* **10**, 1756-1763, doi:10.1021/acs.nano.5b06631 (2016).
- 20 Frank, O. *et al.* Raman 2D-Band Splitting in Graphene: Theory and Experiment. *ACS Nano* **5**, 2231-2239, doi:10.1021/nn103493g (2011).
- 21 Ma, T. *et al.* Tailoring the thermal and electrical transport properties of graphene films by grain size engineering. *Nature Communications* **8**, 14486, doi:10.1038/ncomms14486 (2017).
- 22 Li, Z. Q. *et al.* Dirac charge dynamics in graphene by infrared spectroscopy. *Nature Physics* **4**, 532-535, doi:10.1038/nphys989 (2008).

- 23 Balandin, A. A. Thermal properties of graphene and nanostructured carbon materials. *Nature Materials* **10**, 569-581, doi:10.1038/nmat3064 (2011).
- 24 Falin, A. et al. Mechanical properties of atomically thin boron nitride and the role of interlayer interactions. *Nature Communications* **8**, 15815, doi:10.1038/ncomms15815 (2017).
- 25 Zhou, H. et al. Chemical vapour deposition growth of large single crystals of monolayer and bilayer graphene. *Nature Communications* **4**, 2096, doi:10.1038/ncomms3096 (2013).
- 26 Ma, W. et al. Interlayer epitaxy of wafer-scale high-quality uniform AB-stacked bilayer graphene films on liquid Pt3Si/solid Pt. *Nature Communications* **10**, 2809, doi:10.1038/s41467-019-10691-2 (2019).
- 27 Kairi, M. I., Khavarian, M., Bakar, S. A., Vigolo, B. & Mohamed, A. R. Recent trends in graphene materials synthesized by CVD with various carbon precursors. *Journal of Materials Science* **53**, 851-879, doi:10.1007/s10853-017-1694-1 (2018).
- 28 Petrone, N. et al. Chemical Vapor Deposition-Derived Graphene with Electrical Performance of Exfoliated Graphene. *Nano Letters* **12**, 2751-2756, doi:10.1021/nl204481s (2012).
- 29 Giovannetti, G. et al. Doping Graphene with Metal Contacts. *Physical Review Letters* **101**, 026803, doi:10.1103/PhysRevLett.101.026803 (2008).
- 30 Belyaeva, L. A. et al. Liquids relax and unify strain in graphene. *Nature Communications* **11**, 898, doi:10.1038/s41467-020-14637-x (2020).
- 31 Neumaier, D., Pindl, S. & Lemme, M. C. Integrating graphene into semiconductor fabrication lines. *Nature Materials* **18**, 525-529, doi:10.1038/s41563-019-0359-7 (2019).
- 32 Kwon, S.-J. et al. Extremely stable graphene electrodes doped with macromolecular acid. *Nature Communications* **9**, 2037, doi:10.1038/s41467-018-04385-4 (2018).
- 33 Han, S., Sun, J., He, S., Tang, M. & Chai, R. The application of graphene-based biomaterials in biomedicine. *Am J Transl Res* **11**, 3246-3260 (2019).
- 34 Wang, G. et al. Seamless lateral graphene p–n junctions formed by selective in situ doping for high-performance photodetectors. *Nature Communications* **9**, 5168, doi:10.1038/s41467-018-07555-6 (2018).

- 35 Kumar, S. & Parekh, S. H. Linking graphene-based material physicochemical properties with molecular adsorption, structure and cell fate. *Communications Chemistry* **3**, 8, doi:10.1038/s42004-019-0254-9 (2020).
- 36 Englert, J. M. et al. Covalent bulk functionalization of graphene. *Nature Chemistry* **3**, 279-286, doi:10.1038/nchem.1010 (2011).
- 37 Wang, W., Zhang, Y. & Wang, Y. B. Noncovalent  $\pi\cdots\pi$  interaction between graphene and aromatic molecule: structure, energy, and nature. *J Chem Phys* **140**, 094302, doi:10.1063/1.4867071 (2014).
- 38 Zhang, C. et al. Catalytic mechanism of graphene-nickel interface dipole layer for binder free electrochemical sensor applications. *Communications Chemistry* **1**, 94, doi:10.1038/s42004-018-0088-x (2018).
- 39 Gustafsson, M. G. L. Surpassing the lateral resolution limit by a factor of two using structured illumination microscopy. *Journal of Microscopy* **198**, 82-87, doi:10.1046/j.1365-2818.2000.00710.x (2000).
- 40 Polini, M. & Koppens, F. H. L. Plasmons in moiré superlattices. *Nature Materials* **14**, 1187-1188, doi:10.1038/nmat4496 (2015).
- 41 Finney, N. R. et al. Tunable crystal symmetry in graphene–boron nitride heterostructures with coexisting moiré superlattices. *Nature Nanotechnology* **14**, 1029-1034, doi:10.1038/s41565-019-0547-2 (2019).
- 42 Alexeev, E. M. et al. Resonantly hybridized excitons in moiré superlattices in van der Waals heterostructures. *Nature* **567**, 81-86, doi:10.1038/s41586-019-0986-9 (2019).
- 43 Liu, L. et al. Bottom-up growth of homogeneous Moiré superlattices in bismuth oxychloride spiral nanosheets. *Nature Communications* **10**, 4472, doi:10.1038/s41467-019-12347-7 (2019).
- 44 Moore, A. L. & Shi, L. Emerging challenges and materials for thermal management of electronics. *Materials Today* **17**, 163-174, doi:https://doi.org/10.1016/j.mattod.2014.04.003 (2014).
- 45 Wang, L. et al. Correlated electronic phases in twisted bilayer transition metal dichalcogenides. *Nature Materials* **19**, 861-866, doi:10.1038/s41563-020-0708-6 (2020).

- 46 Carr, S. et al. Twistronics: Manipulating the electronic properties of two-dimensional layered structures through their twist angle. *Physical Review B* **95**, 075420, doi:10.1103/PhysRevB.95.075420 (2017).
- 47 Cao, Y. et al. Unconventional superconductivity in magic-angle graphene superlattices. *Nature* **556**, 43-50, doi:10.1038/nature26160 (2018).
- 48 Jones, A. J. H. et al. Observation of Electrically Tunable van Hove Singularities in Twisted Bilayer Graphene from NanoARPES. *Advanced Materials* **32**, 2001656, doi:10.1002/adma.202001656 (2020).
- 49 Liao, L. et al. van Hove Singularity Enhanced Photochemical Reactivity of Twisted Bilayer Graphene. *Nano Letters* **15**, 5585-5589, doi:10.1021/acs.nanolett.5b02240 (2015).
- 50 Shen, C. et al. Correlated states in twisted double bilayer graphene. *Nature Physics* **16**, 520-525, doi:10.1038/s41567-020-0825-9 (2020).
- 51 He, M. et al. Symmetry breaking in twisted double bilayer graphene. *Nature Physics*, doi:10.1038/s41567-020-1030-6 (2020).
- 52 Haddadi, F., Wu, Q., Kruchkov, A. J. & Yazyev, O. V. Moiré Flat Bands in Twisted Double Bilayer Graphene. *Nano Letters* **20**, 2410-2415, doi:10.1021/acs.nanolett.9b05117 (2020).
- 53 Culchac, F. J., Del Grande, R. R., Capaz, R. B., Chico, L. & Morell, E. S. Flat bands and gaps in twisted double bilayer graphene. *Nanoscale* **12**, 5014-5020, doi:10.1039/C9NR10830K (2020).

## **Chapter 3:**

# **Nanoscale visualization of multilayer graphene**

### 3.1 Mapping of Bernal and non-Bernal stacking domains in bilayer graphene using infrared nanoscopy

- It has been submitted as a paper.

#### 3.1.1 Introduction

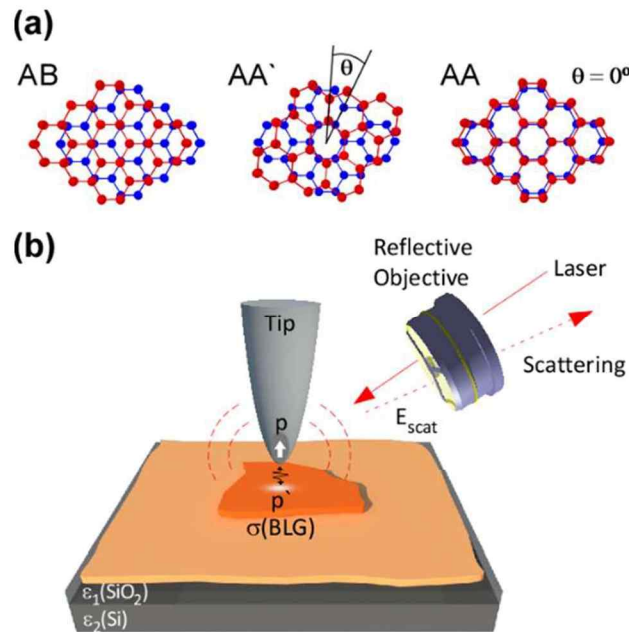


**Figure 3.1.1 Schematic illustration of possible stacking structures of bilayer graphene and IR-sSNOM setup** (a) Possible stacking structures of bilayer graphene (BLG): AB (Bernal), AA' (twisted bilayer graphene), and AA. The angle  $\theta$  is the crystallographic angle between the two graphene layers ( $\theta = 0^\circ \sim 30^\circ$ ). (b) Schematic of infrared-scattering-type scanning near-field optical microscopy (IR-sSNOM) measurement: the  $p$  and  $p'$  are the tip-dipole and its image on sample surface, respectively. The scattering amplitude is influenced by the local optical properties of the sample, including optical conductivity of graphene ( $\sigma$ ) and dielectric constants of substrate materials ( $\epsilon_1(\text{SiO}_2)$  and  $\epsilon_2(\text{Si})$ ).

Stacking orders in multi-layer graphene control band-structures, resulting in potentially useful stacking-specific electrical and opto-electric properties<sup>1-7</sup>. Particularly, the bilayer graphene (BLG), the simplest multilayer graphene<sup>8</sup>, can assume (Figure 3.1.1a) stable AB-stacking (Bernal) structure, in which half of carbon

atoms of the second layer lie directly over the center of a hexagon in the first graphene layer and the other half of carbon atoms lie above the carbon atoms of the first layer, or a meta-stable AA'-stacking structure (twisted bilayer graphene, tBLG), in which the crystallographic axes of the two layers have an arbitrary angle ( $\theta = 0^\circ \sim 30^\circ$ ). The chemical vapor deposition (CVD) method provides large-area BLG samples<sup>9</sup> with AB and AA' stacking domains, offering an excellent opportunity to explore how the stacking structures influence optical and opto-electronic properties. However, such CVD-BLG samples are usually made of co-existing domains with various stacking structures, necessitating microscopy techniques that can identify such domains.

While electron microscopy<sup>9-12</sup> and scanning tunneling microscopy<sup>13</sup> reveal atomic resolution stacking structures of graphene, they are limited to the samples on conducting substrates or to the ones in free-standing conditions. Raman spectroscopy<sup>14-16</sup> reveals the stacking domains of BLG through the characteristic spectral signatures of G and 2D peaks, yet its spatial resolution is limited to  $\sim 1 \mu\text{m}$ , and in some cases spectrum-structure correlation is not uniquely determined. The far-field infrared (IR) spectroscopy delivers information<sup>3, 5</sup> on stacking orders through the stacking-specific IR-conductivity spectra.<sup>4, 5</sup> Unfortunately, the spatial resolution ( $5 \sim 10 \mu\text{m}$ ) of conventional IR spectro-microscopy is insufficient to spatially resolve the co-existing stacking domains.

Here we show that infrared scattering-type scanning near-field optical microscopy (IR-sSNOM)<sup>17-30</sup> can visualize and characterize the Bernal and non-Bernal stacking domains in BLG. In IR-sSNOM (see Figure 1b and Method section), light excites an oscillating dipole ( $\mathbf{p}$ ) at the tip-end, and the tip-dipole interacts with

its own image ( $p'$ ) via dipole-dipole coupling. The amplitude of image-dipole is determined by the local optical properties (including the local conductivity of graphene,  $\sigma$ , and dielectric constants of substrate materials (in this case  $\text{SiO}_2$  and Si)). As such, the scattering amplitude from the tip-sample junction (the IR-sSNOM amplitude) carries local optical properties of the sample. Because both the intra- and inter- band optical conductivities of BLG depends on local stacking structures, IR-sSNOM images can reveal the local stacking structures of BLG.

### 3.1.2 Experiment

**Materials (CVD bilayer graphene)** - Graphene films were synthesized on 25  $\mu\text{m}$  thick copper foils through the CVD method<sup>31</sup>, using methane (50 s.c.c.m.) and hydrogen (5 s.c.c.m.) gas with vacuum pumping ( $\sim 1.5$  mtorr) at 1000  $^{\circ}\text{C}$  for  $\sim 2$  hours. Methane was used only during the growth stages of graphene and was not used during the cooling process. Poly(methyl methacrylate) (PMMA) was spin-coated on top of graphene and the copper foil was etched in an ammonium persulfate solution (20 mM with distilled water). The achieved monolayer graphene films were transferred onto  $\text{SiO}_2$  (thickness of 285 nm) / Si substrates. The monolayer covers nearly all area of the  $\text{SiO}_2/\text{Si}$  substrate, and bilayer domains appear as islands with an average radius of  $\sim 10$   $\mu\text{m}$ .

**Measurement** - We use the side-illuminated IR-sSNOM<sup>17-30</sup> (Figure 1b), consisting of a tapping-mode atomic force microscope (AFM), infrared lasers (an infrared HeNe at  $\lambda = 3.39$  and a quantum cascade laser at  $\lambda = 10.0$   $\mu\text{m}$ ), a Michelson interferometer, and infrared detectors (an InSb detector for  $\lambda = 3.39$   $\mu\text{m}$ , and a mercury cadmium telluride (MCT) detector for  $\lambda = 10.0$   $\mu\text{m}$ ) cooled with liquid-nitrogen. A PtIr coated AFM tip (Nanosensors, PPP-NCHPt) is dithered near the resonance frequency of an AFM- cantilever ( $\Omega \sim 300$  kHz) with a full amplitude of 20  $\sim$  100 nm above the sample surface. Linearly polarized (p-polarized with respect to the sample surface) light from the laser is focused on the tip-sample junction with an angle of  $30^{\circ}$  with respect to the sample surface via a Schwarzschild objective lens. Scattered light from the tip-sample junction is collected by the same objective lens. The collected light is homodyne-amplified and detected by the IR-detector, and the detected signal is lock-in filtered at the 2<sup>nd</sup> harmonic ( $2\Omega \sim 600$  kHz) of the tip

oscillation to give the intensity ( $|s_2|^2$ ) and phase ( $\phi_2$ ) of the demodulated complex amplitude. Micro-Raman spectroscopy measurements (an excitation wavelength of 514.5 nm) are carried out on the sample to determine the number of layers (n) and to cross-confirm the stacking domain assignment in BLG.

### 3.1.3 Results and discussion

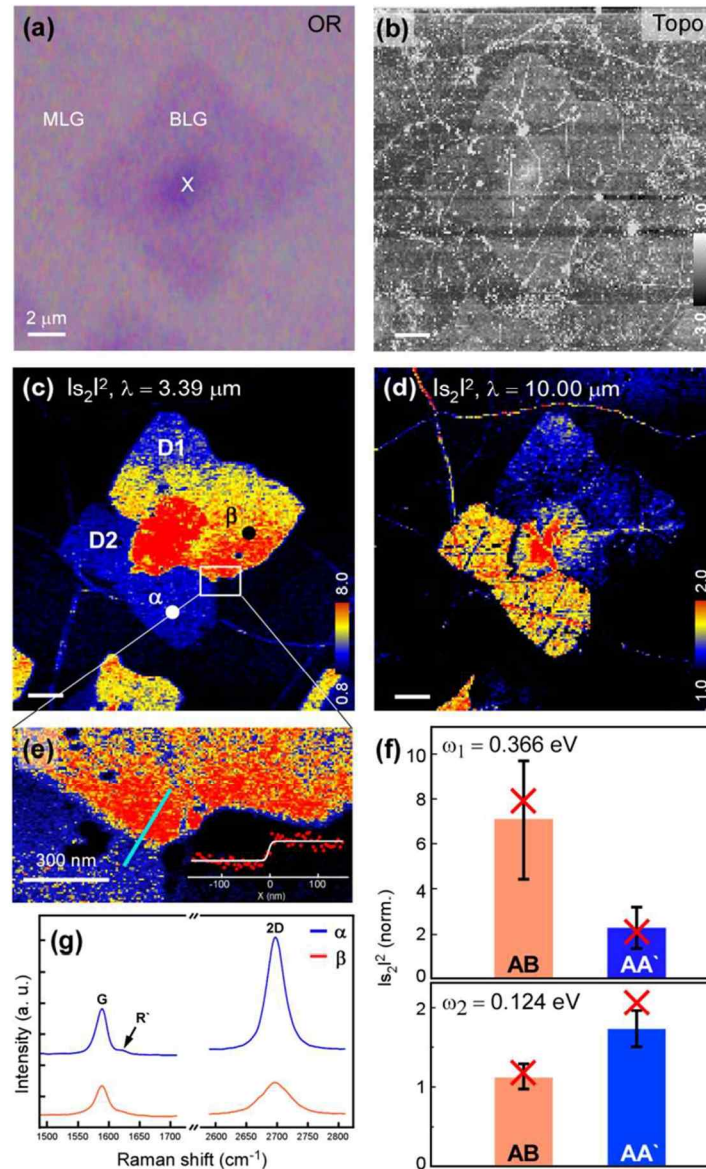


**Figure 3.1.2 Stacking dependent IR-sSNOM images of BLGs.** (a) Far-field white-light reflection image (OR). Entire sample surface is covered by mono-layer graphene (MLG) and bilayer graphene (BLG) islands are formed on top of the MLG. At the centers of BLG islands are thicker ( $n > 2$ ) graphene layers (X). (b) AFM Topography. (c) & (d) IR-sSNOM intensity ( $|s_2|^2$ ) images of BLG obtained with IR light at  $\lambda = 3.39 \mu\text{m}$  (c) and at  $\lambda = 10.00 \mu\text{m}$  (d), revealing two domains (D1 and D2). The wire-like features in Figures 2c and d outside of BLG-regions originate from the wrinkle structures (compare IR-sSNOM and the topography images). For images (a) ~ (d) scale bars represent  $2 \mu\text{m}$  length scale. The gradation of color in D1 (blue to red) is an experimental error caused by the slow drift of laser focus onto the

tip, giving intensity gradient along the slow scanning-axis (vertical direction in image). **(e)** Zoom-in scan of square-marked region of BLG in **(c)**. Inset shows the line-profile sampled along the line (light blue) in image **(e)**, and the fit to a sigmoidal function, providing full transitional width of 38 nm. The **(f)** Domain- specific IR-sSNOM contrasts at two different photon energies. The error bars represent both the intensity variation within individual images and also sample-to-sample variation. Red crosses (x) represent IR-sSNOM model contrasts for AB-BLG and AA-BLG

Figures 3.1.2a-d compare the optical reflection (OR), AFM topography (Topo), and IR-sSNOM intensity ( $|s_2|^2$ , wavelengths of 3.39  $\mu\text{m}$  and 10.00  $\mu\text{m}$ ) images of a CVD-grown BLG island on a  $\text{SiO}_2/\text{Si}$  substrate. In this sample, entire sample surface is covered with mono-layer graphene (MLG) and the BLG islands are grown as an additional layer on top of the MLG. At the centers of each island are thicker multilayer graphene domains (denoted as X). In this work, the IR-sSNOM intensity of BLG shown is normalized to that of MLG/ $\text{SiO}_2/\text{Si}$  to facilitate the comparison with IR-sSNOM model intensities described below. While the OR and AFM images show homogeneous profiles of BLG, the IR-sSNOM intensity map at  $\lambda = 3.39 \mu\text{m}$  (with a photon energy  $\omega_1 = 0.366 \text{ eV}$ ) (Figure 3.1.2c) shows bright and dark domains (D1 and D2 in Figure 3.1.2c). With IR light at  $\lambda = 10.0 \mu\text{m}$  (with a photon energy  $\omega_2 = 0.124 \text{ eV}$ ), IR-sSNOM image of BLG also reveal the same domain structures, but with intensity contrasts that are complementary to the ones obtained at  $\omega_1$  (compare Figures 3.1.2c and d).

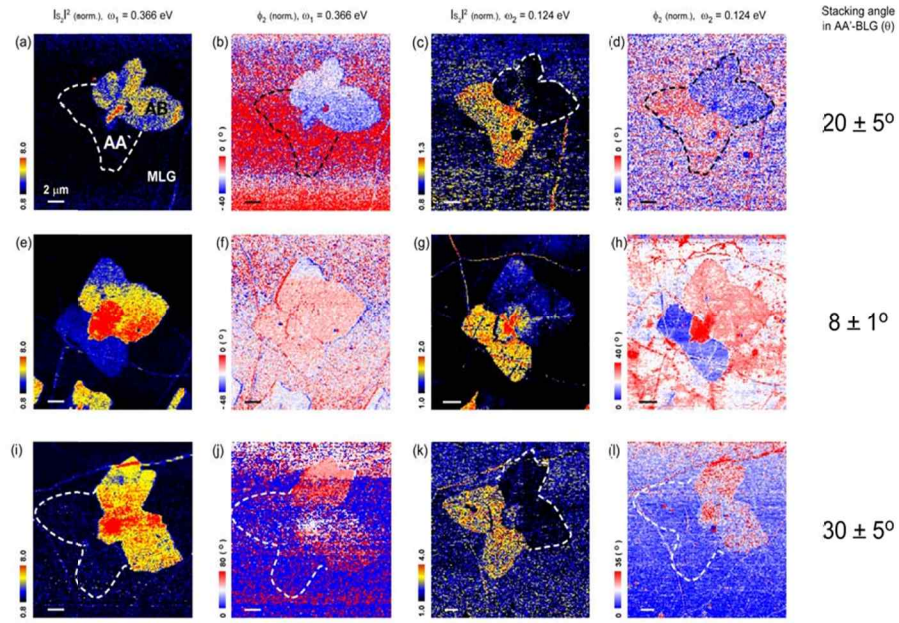


**Figure 3.1.3.** Examples of IR-sSNOM intensity ( $|s_2|^2$ ) and phase ( $\phi_2$ ) images of BLG obtained with IR light at  $\omega_1 = 0.366$  eV and  $\omega_2 = 0.124$  eV. The scale bars correspond to 2  $\mu\text{m}$ . Last column shows the stacking angles ( $\theta$ ) of AA'-BLG in each image, estimated from the Raman spectra.

Such features are consistently observed in all of the BLG samples we have examined (see Figure 3.1.3). In particular, two types of domains are recognized: the domains with pronounced IR-sSNOM intensities ( $|s_2|^2 = 4 \sim 9$ ) at  $\omega_1$ , and the ones with weak IR-sSNOM intensities ( $|s_2|^2 < 2$ ) at  $\omega_2$ . The IR-sSNOM contrasts for the two types of domains are found to be reversed at  $\omega_2$  (see Figure 3.1.2f). We assign that the former is the AB-stacked BLG (AB-BLG), and the latter is the AA'-BLG with arbitrary stacking angles.

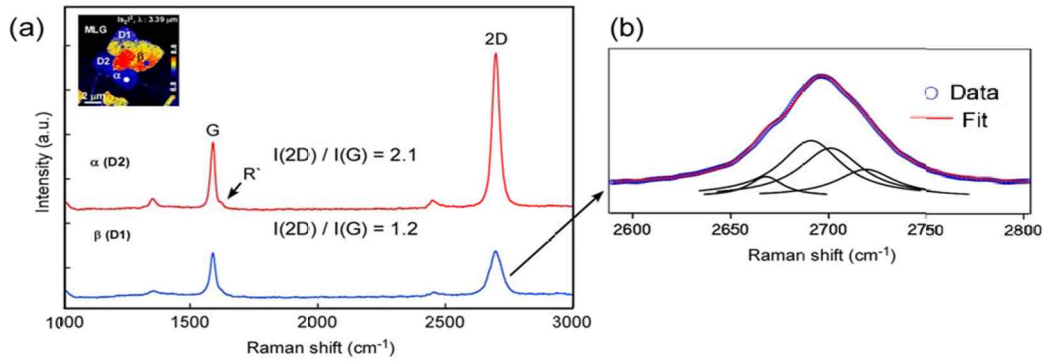


**Figure 3.1.4. Comparison of Raman spectra of different stacking structures BLG (a)** The Raman spectra of a BLG on SiO<sub>2</sub>/Si substrate (excitation wavelength of  $\lambda_{ex} = 514.5$  nm) obtained from the D1 ( $\beta$ ) and D2 ( $\alpha$ ) regions of BLG shown in Figure 3.1.2c of main text. **(b)** Line-shape analysis of 2D peak of  $\beta$  (D1), showing characteristic line-shape for AB-BLG.

From a separate Raman spectroscopic measurement (intensity ratios of G and 2D peaks, and the line-shape analysis on 2D peak<sup>32-37</sup>; see Figure 3.1.2g and Figure 3.1.4) on BLG domains, we confirm that the bright and dark domains at  $\omega_1$  are AB-BLG (D1 in Figure 3.1.2c) and AA'-BLG with various stacking angles (D2 in Figure 3.1.2c; for the domain D2 in Figure 3.1.2c, Raman spectrum indicates the stacking angle of  $\theta = 8 \pm 1^\circ$ ), respectively. The IR-sSNOM images reveal the transitional width of  $\sim 40$  nm (Figure 3.1.2e) at the domain boundaries, most likely representing the spatial resolution of IR-sSNOM, not the real domain-wall thicknesses.

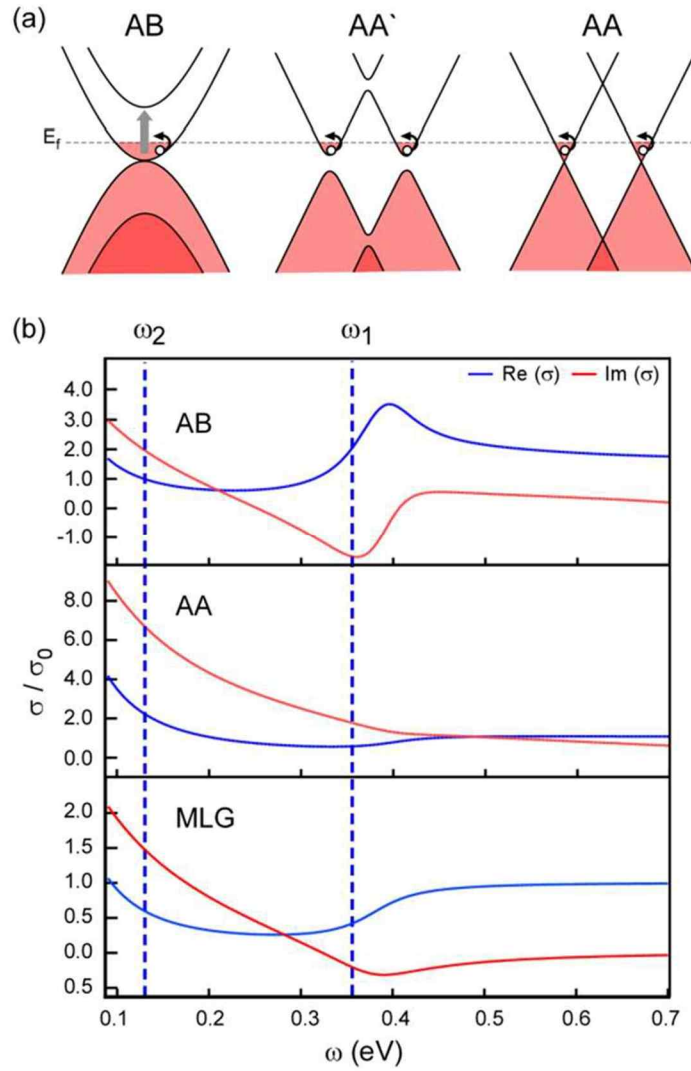


**Figure 3.1.5 Band structures and complex optical conductivity spectra of AB, AA' and AA-BLG.** (a) Schematic representation of band diagrams for AB, AA' and AA-BLG. Inter- and intra-band transitions are marked with grey and black arrows, respectively. (b) Real ( $\text{Re}(\sigma)$ ) and imaginary ( $\text{Im}(\sigma)$ ) parts of the theoretical optical conductivity spectra of AB-BLG, AA-BLG and MLG. See main text for the details of calculation. All of the conductivities ( $\sigma$ ) are expressed in unit of  $\sigma_0 = c\alpha/4$ , where  $c$  and  $\alpha$  are the speed of light and the fine-structure constant, respectively.

Band structures of AB, AA' and AA-BLG (Figure 3.1.5) qualitatively explain the observed IR-sSNOM contrasts at the two photon energies. For AB-BLG, strong interlayer coupling (with a coupling energy of  $\gamma_1 \sim 0.37 \text{ eV}^3$ ,<sup>4, 15</sup> leads to

parabolic energy bands<sup>3</sup>, whereas for AA-BLG, near-zero inter-layer coupling leads to linear energy bands. The band structure of AA'-BLG is similar to AA-BLG, except that it has avoided crossings<sup>8</sup>, with the energy gaps varying with  $\theta$ . The BLG on SiO<sub>2</sub>/Si substrate has a finite substrate-induced doping, placing the Fermi energy ( $E_f$ ) around 0.1 ~ 0.2 eV<sup>38</sup>. Owing to the AB-BLG shows a strong inter-band resonance around 0.4 eV<sup>3, 4, 15</sup>, whereas AA-BLG or AA'-BLG do not show such resonances.

On the other hand, at photon energy,  $\omega < 2E_f \sim 0.3$  eV, inter-band transitions are Pauli-blocked and intra-band transition dominates the conductivities of BLG. As shown in the band diagrams, the AB-BLG has only one conduction channel around  $E_f$ , whereas AA-BLG has two accessible conduction channels, leading to significantly larger conductivity of AA-BLG than that of AB-BLG. Band structures of AA'-BLG and AA-BLG around Fermi energy are similar, and therefore we expect that conductivity of AA'-BLG is also larger than that of AB-BLG. As mentioned above, IR-sSNOM intensities scale with the magnitudes of optical conductivities. These explain why we observe brighter and darker IR-sSNOM contrasts for AB-BLG and AA'-BLG at  $\omega_1 = 0.366$  eV, respectively, whereas such intensity contrasts are reversed at  $\omega_2 = 0.124$  eV.

To place the above arguments on a more quantitative ground, we have carried out point-dipole IR-sSNOM model calculations<sup>27, 39</sup> for BLG/SiO<sub>2</sub>/Si. The complex conductivity spectra of AB-BLG and MLG (Figure 3.1.5b), which are the key input parameters of the simulation, are obtained theoretically, and calibrated against reported experimental spectra<sup>3, 4, 15, 40</sup>. Realistic modeling of conductivities of AA'-BLG<sup>41, 42</sup> with arbitrary  $\theta$  are beyond the scope of this work. Instead, we calculated the conductivity of AA-BLG, and use this as the limiting conductivities

of AA'-BLG. We theoretically calculated the conductivity spectra based on the tight-binding Hamiltonian<sup>6</sup> with  $\gamma_0$  (intra-layer interaction) = 3.16 eV and  $\gamma_1$  (inter-layer interaction) = 0.37 eV) and the Kubo formula<sup>43</sup> (phenomenological disorder parameter  $\eta = 40$  meV, and Fermi energy of  $E_f = 0.19$  eV). At  $\omega < 2E_f$ , intra-band transitions lead to Drude peaks in the spectra, whereas inter-band transitions are forbidden due to Pauli-blocking. For AA'-BLG with arbitrary  $\theta$  (and also for AA-BLG), inter-layer coupling can be neglected and the system can be interpreted as two decoupled MLG. At  $\omega \gg \gamma_1$ , the real parts of the optical conductivities for AA, AB and AA' approach  $2\sigma_0$ .

In Figure 3.1.2f, we compare the experimental IR-sSNOM intensities of AB-BLG and AA'-BLG, and model IR-sSNOM intensities of AB-BLG and AA-BLG (used as the limiting case of AA'-BLG), at  $\omega_1 = 0.366$  eV and  $\omega_2 = 0.124$  eV. The IR-sSNOM model correctly reproduces key features of the experimental IR-sSNOM intensities of AB and AA'-BLG at two photon energies, fully validating our interpretation.

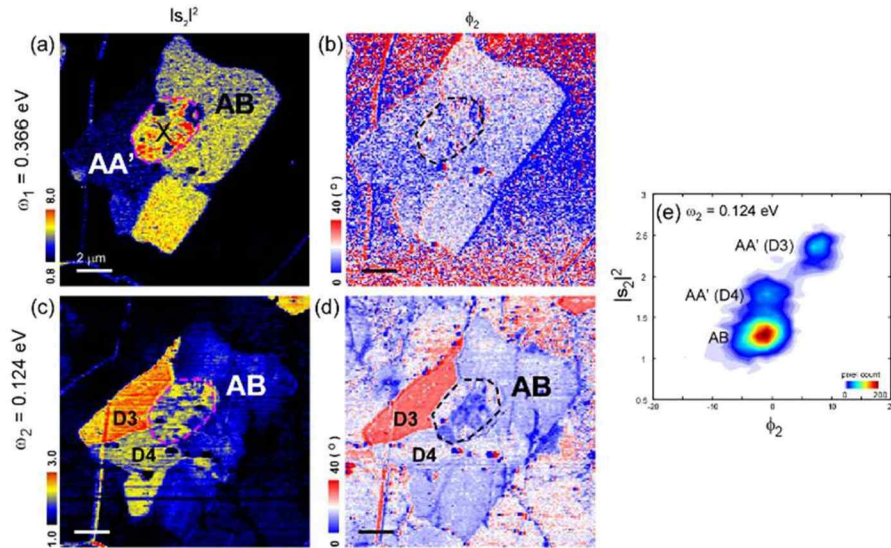


**Figure 3.1.5.** IR-sSNOM intensity ( $|s_2|^2$ ) ((a) & (c)) and phase ( $\phi_2$ ) ((b) & (d)) image of BLG at  $\omega_1 = 0.366$  eV and  $\omega_2 = 0.124$  eV, revealing two different AA'-BLG domains (D3 and D4). Region X is the domain with thicker multilayer graphene ( $n = 3$  and higher). (e) 2- dimensional intensity – phase image histogram of IR-sSNOM image of (c) & (d).

It must be noted, however, that the AA-BLG is a limiting case of AA'-BLG, and as such current IR-sSNOM modeling of AA'-BLG cannot fully explain all of the features of IR-sSNOM images. As shown in Supporting Information-figure S3.1.3, both the IR-sSNOM intensity and phase contrasts of AB-BLG in Figure 3.1.2 can be fully reproduced by the IR-sSNOM model. For AA'-BLG, however, IR-sSNOM phase contrasts at two different frequencies cannot be reproduced by the AA-BLG model. This not only shows missing structural information of AA'-BLG, but it also indicates that IR-sSNOM phase contrast is particularly sensitive to the stacking angles in AA'-BLG.

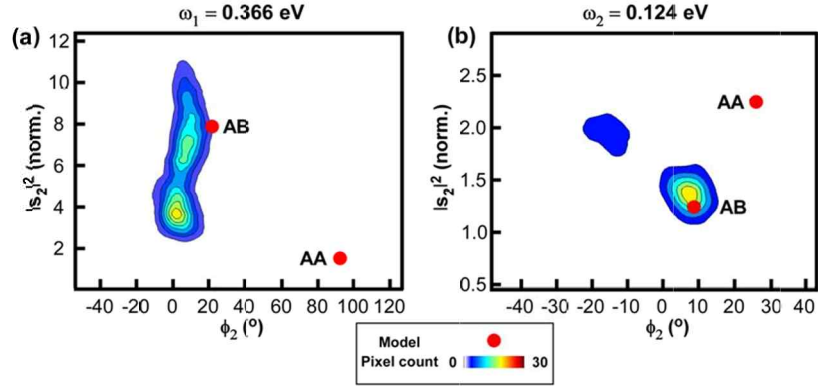


**Figure 3.1.6.** 2-dimensional intensity-phase ( $|s_2|^2$  vs  $\phi_2$ ) histograms of IR-sSNOM images (Figure S3.1.1) at  $\omega_1$  and  $\omega_2$  frequencies, along with IR-sSNOM model of AB-BLG and AA-BLG (red dots). The intensity and phase contrasts of AB-BLG domain can be satisfactorily reproduced by the model, whereas the phase contrasts of AA'-BLG cannot be reproduced by the model that is based on the optical conductivity of AA-BLG.

In particular, as shown in Figure 3.1.6, we find that the IR-sSNOM intensity and phase contrasts at 0.124 eV can differentiate two different AA'-BLG domains (D3 and D4 in Figure 3.1.5), with a phase difference of  $\Delta\phi_2 = 10^\circ$ , demonstrating that the IR-sSNOM phase as well as intensity contrasts may potentially yield stacking angles in AA'-BLG as well, provided that we have a priori knowledge on stacking-angle dependent optical conductivities of AA'-BLG.

### 3.1.4 Conclusions

To sum up, we have shown that IR-sSNOM can visualize various stacking domains of BLG with a  $\sim 40$  nm spatial resolution (see the inset of Figure 3.1.2e, showing a line-profile of IR-sSNOM intensity and a fit to a sigmoidal function. The fit provides a full transitional width of  $\sim 40$  nm), based on stacking-specific inter- and intra-band conductivities. The IR-sSNOM stacking map offers  $\sim 10$  times better spatial resolution than the one available from usual Raman spectroscopic methods. Because the IR-sSNOM can be applied to BLG on dielectric substrates, as well as on metallic substrates (possibly with increased IR-sSNOM sensitivity and image contrasts, due to the enhanced tip-sample coupling<sup>22</sup>), it offers a major practical advantage over scanning tunneling microscopy and electron microscopy. This is particularly relevant for in situ characterization of the BLG-devices, most of which are built on dielectric substrates. The method, in its current form, does not provide complete information to unambiguously determine the stacking angle between the two layers in AA'-BLG. We emphasize that this is by no means a fundamental limitation to the method: IR-sSNOM measurement with widely tunable IR sources (such as synchrotron source<sup>26</sup> or IR optical parametric oscillators) may provide a fully spectroscopic IR-sSNOM contrasts, enabling us not just to differentiate AB versus AA'-BLG domains but also to obtain the crystallographic angle between the two graphene layers.

### 3.1.5 References

1. W. Bao, L. Jing, J. Velasco, Jr., Y. Lee, G. Liu, D. Tran, B. Standley, M. Aykol, S. B. Cronin, D. Smirnov, M. Koshino, E. McCann, M. Bockrath and C. N. Lau, *Nature Phys.*, **7**, 948-952 (2011).
2. S. Latil and L. Henrard, *Phys. Rev. Lett.*, **97**, 036803 (2006).
3. C. H. Lui, Z. Li, K. F. Mak, E. Cappelluti and T. F. Heinz, *Nat. Phys.*, **7**, 944-947 (2011).
4. K. F. Mak, M. Y. Sfeir, J. A. Misewich and T. F. Heinz, *Proc. Natl. Acad. Sci. U. S. A.*, **107**, 14999-15004 (2010).
5. K. F. Mak, J. Shan and T. F. Heinz, *Phys. Rev. Lett.*, **104**, 176404 (2010).
6. H. Min and A. H. MacDonald, *Prog. Theor. Phys. Suppl.*, **176**, 227-252 (2008).
7. A. Kumar, W. Escoffier, J. M. Poumirol, C. Faugeras, D. P. Arovas, M. M. Fogler, F. Guinea, S. Roche, M. Goiran and B. Raquet, *Phys. Rev. Lett.*, **107**, 126806 (2011).
8. I. Redouani and A. Jellal, *Mater. Res. Express*, **3**, 065005 (2016).
9. A. W. Tsen, L. Brown, R. W. Havener and J. Park, *Acc. Chem. Res.*, **46**, 2286-2296 (2013).
10. L. Brown, R. Hovden, P. Huang, M. Wojcik, D. A. Muller and J. Park, *Nano Lett.*, **12**, 1609-1615 (2012).
11. A. W. Robertson, A. Bachmatiuk, Y. A. Wu, F. Schäffel, B. Rellinghaus, B. Büchner, M. H. Rummeli and J. H. Warner, *ACS Nano*, **5**, 6610-6618 (2011).
12. J. H. Warner, M. Mukai and A. I. Kirkland, *ACS Nano*, **6**, 5680-5686 (2012).
13. M. Yankowitz, J. I.-J. Wang, A. G. Birdwell, Y.-A. Chen, K. Watanabe, T. Taniguchi, P. Jacquod, P. San-Jose, P. Jarillo-Herrero and B. J. LeRoy, *Nat. Mater.*, **13**, 786-789 (2014).
14. C. Cong, T. Yu, K. Sato, J. Shang, R. Saito, G. F. Dresselhaus and M. S. Dresselhaus, *ACS Nano*, **5**, 8760-8768 (2011).
15. C. H. Lui, Z. Li, Z. Chen, P. V. Klimov, L. E. Brus and T. F. Heinz, *Nano Lett.*, **11**, 164-169 (2011).
16. K. Kim, S. Coh, L. Z. Tan, W. Regan, J. M. Yuk, E. Chatterjee, M. F.

- Crommie, M. L. Cohen, S. G. Louie and A. Zettl, *Phys. Rev. Lett.*, **108**, 246103 (2012).
17. J. N. Chen, M. Badioli, P. Alonso-Gonzalez, S. Thongrattanasiri, F. Huth, J. Osmond, M. Spasenovic, A. Centeno, A. Pesquera, P. Godignon, A. Z. Elorza, N. Camara, F. J. G. de Abajo, R. Hillenbrand and F. H. L. Koppens, *Nature*, **487**, 77-81 (2012).
  18. Z. Fei, A. S. Rodin, G. O. Andreev, W. Bao, A. S. McLeod, M. Wagner, L. M. Zhang, Z. Zhao, M. Thiemens, G. Dominguez, M. M. Fogler, A. H. C. Neto, C. N. Lau, F. Keilmann and D. N. Basov, *Nature*, **487**, 82-85 (2012).
  19. Z. Fei, G. O. Andreev, W. Z. Bao, L. F. M. Zhang, A. S. McLeod, C. Wang, M. K. Stewart, Z. Zhao, G. Dominguez, M. Thiemens, M. M. Fogler, M. J. Tauber, A. H. Castro- Neto, C. N. Lau, F. Keilmann and D. N. Basov, *Nano Lett.*, **11**, 4701-4705 (2011).
  20. F. Huth, A. Govyadinov, S. Amarie, W. Nuansing, F. Keilmann and R. Hillenbrand, *Nano Lett.*, **12**, 3973– 3978 (2012).
  21. D. S. Kim, J. Heo, S. H. Ahn, S. W. Han, W. S. Yun and Z. H. Kim, *Nano Lett.*, **9**, 3619-3625 (2009).
  22. J. Aizpurua, T. Taubner, F. J. de Abajo, M. Brehm and R. Hillenbrand, *Opt. Express*, **16**, 1529-1545 (2008).
  23. M. Wagner, Z. Fei, A. S. McLeod, A. S. Rodin, W. Bao, E. G. Iwinski, Z. Zhao, M. Goldflam, M. Liu, G. Dominguez, M. Thiemens, M. M. Fogler, A. H. C. Neto, C. N. Lau, S. Amarie, F. Keilmann and D. N. Basov, *Nano Lett.*, **14**, 894–900 (2014).
  24. J. N. Chen, M. L. Nesterov, A. Y. Nikitin, S. Thongrattanasiri, P. Alonso-Gonzalez, T. M. Slipchenko, F. Speck, M. Ostler, T. Seyller, I. Crassee, F. H. L. Koppens, L. Martín-Moreno, F. J. G. de Abajo, A. B. Kuzmenko and R. Hillenbrand, *Nano Lett.*, **13**, 6210-6215 (2013).
  25. S. Berweger, D. M. Nguyen, E. A. Muller, H. A. Bechtel, T. T. Perkins and M. B. Raschke, *J. Am. Chem. Soc.*, **135**, 18292-18295 (2013).
  26. H. A. Bechtel, E. A. Muller, R. L. Olmon, M. C. Martin and M. B. Raschke, *Proc. Natl. Acad. Sci. U.S.A.*, **111**, 7191–7196 (2014).
  27. D.-S. Kim, H. Kwon, A. Y. Nikitin, S. Ahn, L. Martín-Moreno, F. J. García-Vidal, S. Ryu, H. Min and Z. H. Kim, *ACS Nano*, **9**, 6765-6773 (2015).

28. G. X. Ni, H. Wang, J. S. Wu, Z. Fei, M. D. Goldflam, F. Keilmann, B. Ozyilmaz, A. H. Castro Neto, X. M. Xie, M. M. Fogler and D. N. Basov, *Nat. Mater.*, **14**, 1217-1222 (2015).
29. S. Gamage, Z. Li, V. S. Yakovlev, C. Lewis, H. Wang, S. B. Cronin and Y. Abate, *Adv. Mater. Interfaces*, **3**, 1600121 (2016).
30. T. G. Habteyes, *J. Phys. Chem. C*, **118**, 9119-9127 (2014).
31. W. H. Park, I. S. Jo, B. H. Hong and H. Cheong, *Nanoscale*, 9822-9827 (2016).
32. S. Sahoo, R. Palai and R. S. Katiyar, *J. Appl. Phys.*, **110**, 044320 (2011).
33. C.-H. Yeh, Y.-C. Lin, P. K. Nayak, C.-C. Lu, Z. Liu, K. Suenaga and P.-W. Chiu, *J. Raman Spectrosc.*, **45**, 912-917 (2014).
34. C. C. Lu, Y. C. Lin, Z. Liu, C. H. Yeh, K. Suenaga and P. W. Chiu, *ACS Nano*, **7**, 2587-2594 (2013).
35. X. D. Chen, W. Xin, W. S. Jiang, Z. B. Liu, Y. Chen and J. G. Tian, *Adv. Mater.*, **28**, 2563 (2016).
36. D. H. Yoon, H. R. Moon, Y.-W. Son, G. Samsonidze, B. H. Park, J. B. Kim, Y. P. Lee and H. S. Cheong, *Nano Lett.*, **8**, 4270-4274 (2008).
37. A. C. Ferrari, J. C. Meyer, V. Scardaci, C. Casiraghi, M. Lazzeri, F. Mauri, S. Piscanec, D. Jiang, K. S. Novoselov, S. Roth and A. K. Geim *Phys. Rev. Lett.*, **97**, 187401 (2006).
38. Y. J. Kang, J. G. Kang and K. J. Chang, *Phys. Rev. B*, **78**, 115404 (2008).
39. D. S. Kim and Z. H. Kim, *Opt. Express*, **20**, 8689- 8699 (2012).
40. Z. Li, C. H. Lui, E. Cappelluti, L. Benfatto, K. F. Mak, G. L. Carr, J. Shen and T. F. Heinz, *Phys. Rev. Lett.*, **7**, 156801 (2012).
41. C. J. Tabert and E. J. Nicol, *Phys. Rev. B*, **87**, 121402 (2013).
42. S. Tobias, S.-J. Pablo and B. Luis, *New J. Phys.*, **15**, 113050 (2013).
43. K. Ziegler, *Phys. Rev. B*, **55**, 10661 (1997).

## 4.1 Narrow infrared resonance of commensurate-incommensurate transition for tetramer-graphene on hexagonal boron nitride

- This paper will be submitted.

### 4.1.1 Introduction

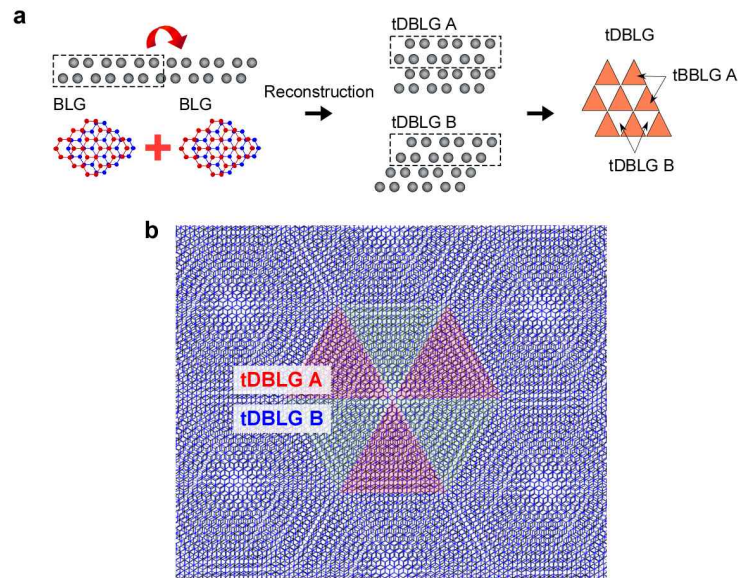


**Figure 4.1.1. Reconstruction of tDBG moiré pattern.** **a**, Schematics of twisted double bilayer graphene (tDBG) preparation. **b**, Schematics of twisted double bilayer graphene (tDBG)

Graphene is well known for its two-dimensional honeycomb structure crystal, whose peculiar electronic properties have raised considerable interests in the past few years. When two 2D materials layers are physically stacked in series with an arbitrary angle<sup>1</sup>, a distinctive pattern is created due to lattice mismatch and relative rotation between the layers. This interference pattern is called the moiré-pattern<sup>2</sup>. The atomic-scale crystalline alignment between the layers plays a critical role

determining properties of the layers. Also, these electronic properties in stacked graphene layers can be tuned by manipulating a twisted angle. Twistronics<sup>3,4</sup> are actively studied to control the electronics of these materials. And previous researches reported remarkable results when two layers are placed with specific magic angles<sup>2,4</sup>, the moiré patterns exhibit special properties such as superconducting phases<sup>5,6</sup>. In addition, a sharp peak associated with band-flattening near the charge-neutrality point is shown when the two van Hove singularities (VHS) in the density of states (DOS) of each monolayer are merged<sup>5</sup> in the angle<sup>2,7</sup>. Furthermore, these are not unique cases of the merging mono layered graphene. Recent studies reported<sup>6,7</sup> that moiré flat bands are made even with two Bernal stacking bilayer graphene overlapped with a specific small angle, which is twisted double bilayer graphene (tDBG).

The commonly used imaging tools for moiré pattern is electron microscopy (EM)<sup>8</sup> or scanning tunneling microscopy (STM)<sup>9,10</sup>. Because the size of the moiré pattern ranges from few nanometers to tens of nanometers, it is difficult to distinguish with common optical microscopy due to diffraction limit. Although, these imaging tools allow accurately to measure the size of the moiré pattern, there are several disadvantages. First, graphene sample can be damaged by electron beams during measurement<sup>11</sup>. In addition, it is difficult to satisfy the sample condition because the sample must be placed in an ultra-high vacuum (UHV) condition and substrate for STM is limited<sup>12</sup>. As these shortcomings stand out, the importance of infrared scattering scanning near-field microscopy (IR-sSNOM) has come into the spotlight<sup>8,13</sup>. AFM based IR-sSNOM is possible to measure a few nano-meter resolution without damaging the sample. The IR-sSNOM also has the advantage of having a huge range of choices for the sample substrates. For this reason, many

research papers<sup>8,14</sup> have confirmed the moiré-pattern by mapping the conductivity of graphene using IR-sSNOM. However, there is something more to consider about moiré-pattern imaging using IR-sSNOM. The question arises as to whether the information obtained from IR-sSNOM shows only graphene stacking information. If we can obtain not only optical conductivity of stacking structure, but also the peculiar property originated from moiré-pattern via using IR-sSNOM, we need to examine it separately.

In this study, we investigated the moiré structure of tDBG on h-BN using IR-sSNOM, revealing clearly separated domains of tDBG. However, features were significantly wavelength-dependent, which seemed to be highly affected by narrow plasmonic resonance of the graphene<sup>15</sup>. IR-sSNOM spectra shows moiré structure have a localized surface plasmon resonance (LSPR) at specific energy ( $\sim 960 \text{ cm}^{-1}$ ), which varies with stacking structure of graphene, the size of moiré pattern, arrangement of moiré pattern, the shape of the pattern, the edge around the pattern or something else. We also verified our experimental results with numerical finite difference time domain (FDTD) simulation.

### 4.1.2 Experiment

**Sample measurements (IR-sSNOM & FTIR)** - We use the side-illuminated IR-sSNOM, consisting of a tapping-mode atomic force microscope (AFM), Michelson interferometer, infrared lasers (a quantum cascade laser at  $\tilde{\nu} = 952.3 \sim 1428.5 \text{ cm}^{-1}$  and an infrared HeNe at  $\tilde{\nu} = 2949.9 \text{ cm}^{-1}$ ) infrared detectors (a mercury cadmium telluride (MCT) detector for  $\tilde{\nu} = 952.3 \sim 1428.5 \text{ cm}^{-1}$  and an InSb detector for  $\tilde{\nu} = 2949.9 \text{ cm}^{-1}$ ) cooled with liquid-nitrogen. The IR-sSNOM probe (Nanosensors, PPP-NCHPt,  $\Omega \sim 300 \text{ kHz}$ ) vertically vibrates with an amplitude of  $20 \sim 100 \text{ nm}$ . Linearly polarized (p-polarized with respect to the sample surface) light is focused on the tip-sample junction with an angle of  $30^\circ$  with respect to the sample surface via a Schwarzschild objective lens. The collected scattered light is amplified by a homodyne-amplified by a Michelson interferometer and the detected signal is lock-in filtered at the 2<sup>nd</sup> harmonic ( $2 \Omega \sim 600 \text{ kHz}$ ) of the tip oscillation to give the intensity ( $|s_2|^2$ ) and phase ( $\phi_2$ ) of the demodulated complex amplitude.

### 4.1.3 Results and discussion

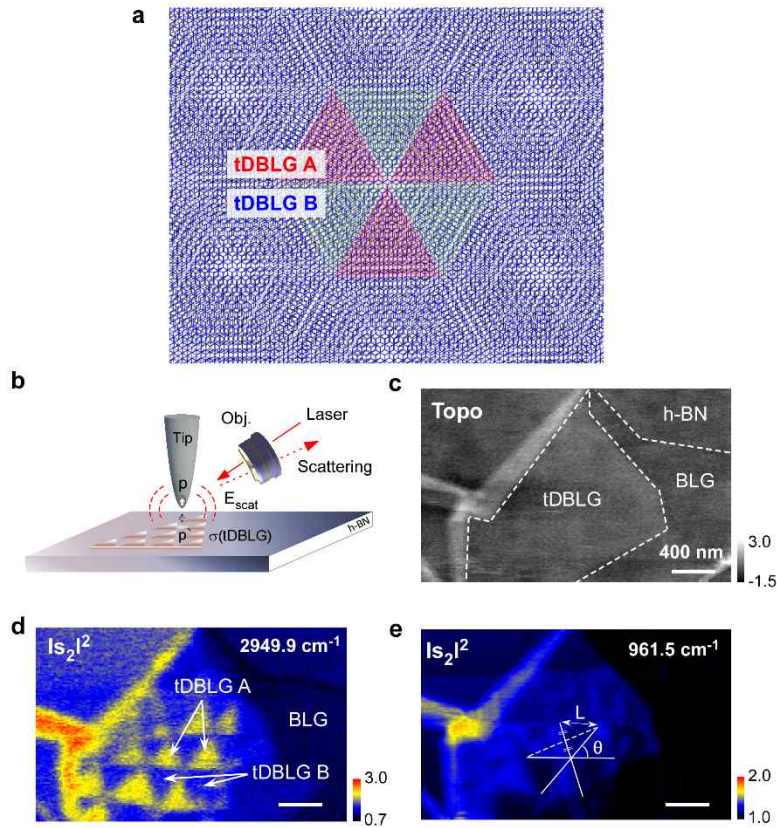


**Figure 4.1.2. Reconstruction of tDBG moiré pattern.** **a**, Schematics of twisted double bilayer graphene (tDBG). **b**, Schematic of IR-scattering-type scanning near-field optical microscopy (IR-sSNOM) measurement. the  $p$  and  $p'$  are the tip-dipole and its image on graphene sample surface, respectively. **c**, AFM images of the tDBG sample. **d**, & **e**, IR-sSNOM intensity ( $|s_2|^2$ ) images of the tDBG obtained with IR light at  $\tilde{\nu} = 2949.9 \text{ cm}^{-1}$  (**d**) and at  $\tilde{\nu} = 961.5 \text{ cm}^{-1}$  (**e**). the tDBG is divided into two domains, tDBG A (bright triangles) and tDBG B (dark triangles). The IR-sSNOM intensity of moiré patterned tDBG shown is normalized to that of hBN. Twist angle ( $\theta$ ) of the tDBG can be estimated by period length ( $L$ ) of near-field image. The estimated twist angle ( $\theta$ ) is  $0.045^\circ$ . All scale bars are 400 nm.

#### IR -sSNOM imaging of reconstructed twisted double bilayer graphene

The tDBG sample (Figure 4.1.2a; see methods for sample preparation procedure) is located on a h-BN flake. It is known that overlapped graphenes reconstruct their structures into new forms. In most cases, a newly constructed

graphene has a triangular pattern. This triangular pattern is called a moiré pattern. We measured this moiré patterned graphene using IR-sSNOM (see Figure 1b and Method section). LASER excites an oscillating dipole ( $p$ ) at the end of tip, and the tip-dipole interacts with its own image dipole ( $p'$ ) via dipole dipole interaction<sup>16,17</sup>. The amplitude of image-dipole is determined by the local optical properties including the local conductivity of moiré patterned graphene ( $\sigma$ ) and dielectric constants of the substrate ( $\epsilon$ ) which is h-BN. The scattering amplitude from the junction carries the local optical properties of the sample in case of the moiré patterned tDBLG. These patterns are not shown in the atomic force microscopy (AFM, Figure 4.1.2c). However, the IR-sSNOM intensity image at  $\tilde{\nu} = 2949.9 \text{ cm}^{-1}$  (Figure 4.1.2d) shows bright (tDBLG A) and dark (tDBLG B) domains. The IR-sSNOM intensity of moiré patterned tDBG is normalized to that of h-BN. The tDBLGs are divided into two different domains as their local stacking structure differences make different intra-band optical conductivities. In the case of tDBLG A, experiment results show there are strong interlayer couplings. On the other hand, there are near-zero inter-layer couplings in the case of tDBLG B. These are mainly caused as tDBLG A and B have different band structures. IR-sSNOM intensity image measured at  $\tilde{\nu} = 961.5 \text{ cm}^{-1}$  (Figure 4.1.2e) are also divided into two domains for similar reasons (in this case difference of intra-band optical conductivities). The size of the moiré pattern is about 300 nm and the twisted angle between two BLGs is estimated about 0.045 degrees<sup>18</sup>. Also, looking closely at Figure 1d or e, the size of the surrounding moiré patterns is different. We assume that the size of the patterns can vary for various reasons. When the two BLGs are overlapped, for example, strains might act differently on the graphene layers<sup>19,20</sup>. Also, this phenomenon could be caused by lattice mismatch between h-BN and graphene<sup>21</sup>.

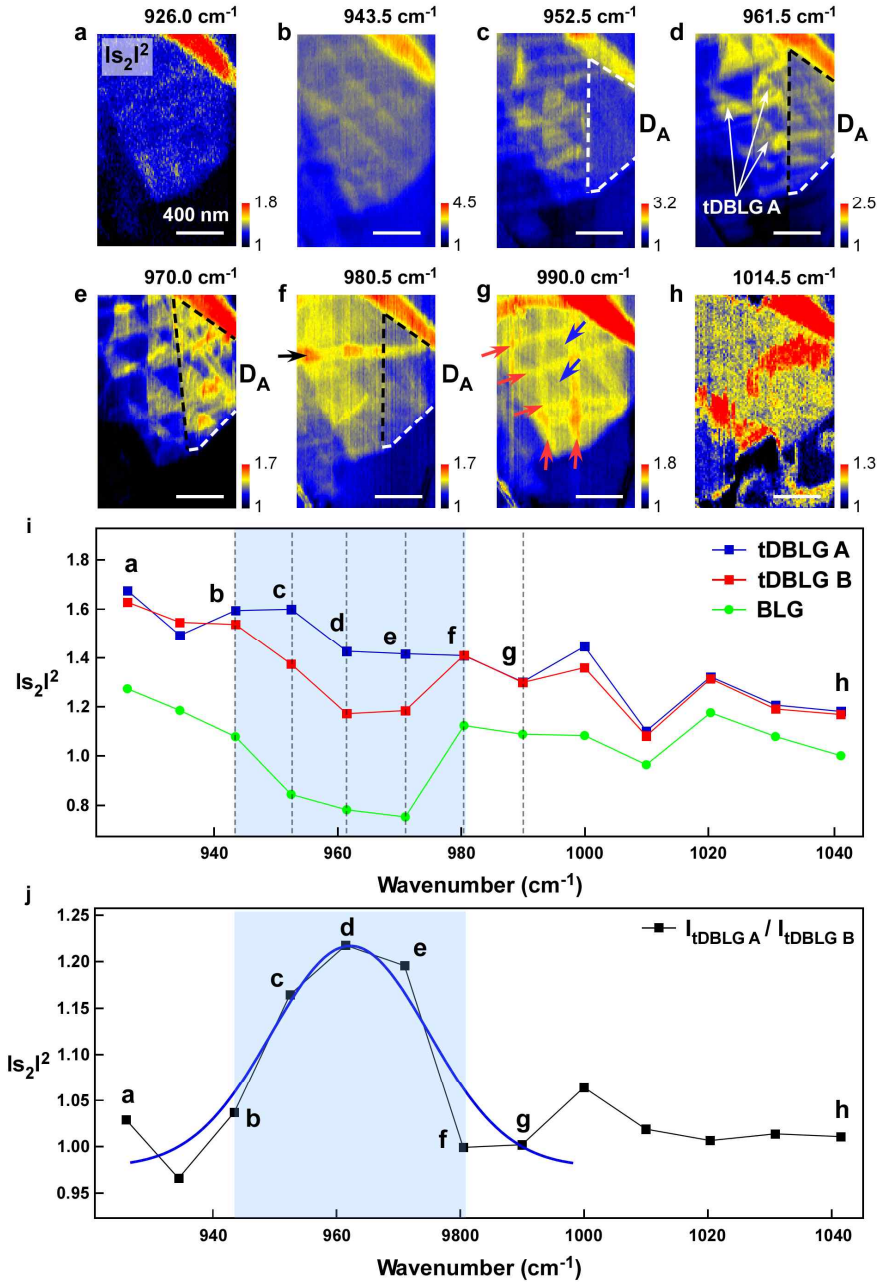


**Figure 4.1.3. Wavenumber dependence of near-field optical intensity contrast changes of tDBG.** a-f, IR-sSNOM intensity ( $|s_2|^2$ ) image of the moiré patterned tDBG obtained with IR light at  $\tilde{\nu} = 926.0$  (a), 943.5 (b), 952.5 (c), 961.5 (d), 970.0 (e), 980.5 (f), 990.0 (g) and 1014.5 (h)  $\text{cm}^{-1}$ . c-f,  $D_A$  means the domain surrounded by dotted lines. g, The red arrows indicates relatively high (positive) contrast line, and the blue arrows indicates relatively low (negative) contrast line. All scale bars in IR-sSNOM images are 400 nm. g, Nano IR-sSNOM intensity spectra of tDBLG A (blue), tDBLG B (red), and BLG (green). h, Nano IR-sSNOM intensity spectrum (blue) of divide intensity of tDBLG A by intensity of tDBLG B. All of the IR-sSNOM intensity images of moiré patterned tDBG is normalized to that of h-BN.

## Spectroscopic signatures of the moiré patterned tDBG

We conducted IR-sSNOM on the moiré patterned tDBG at more IR wavelength between  $\tilde{\nu} = 926.0 \sim 1041.5 \text{ cm}^{-1}$ . Unlike the case in the Figure 4.1.2f, the bright (tDBLG A) and dark (tDBLG B) domains are not clearly divided at  $\tilde{\nu} = 926.0$  and  $934.5 \text{ cm}^{-1}$ . There is a faint streak with very slightly high intensity contrast. This might have taken place due to the interaction of h-BN and tDBLG. Or this phenomenon could occur due to the structures of the moiré pattern. When the wavenumber is changed to a larger wavenumber, the contrast of IR-sSNOM intensities are increased at the specific moiré patterned graphene (tDBLG A and B) as shown in Figures 4.1.3b, c, d and e (at  $\tilde{\nu} = 943.5 \sim 970.0 \text{ cm}^{-1}$ ). Also, at  $\tilde{\nu} = 961.5 \text{ cm}^{-1}$  (Figure 4.1.3d), the greatest IR-sSNOM intensity contrast difference was observed. Also interestingly, the specific domain  $D_A$  is not well distinguished at  $\tilde{\nu} = 952.5$  and  $961.5 \text{ cm}^{-1}$  (Figure 4.1.3c and d), but at  $\tilde{\nu} = 970.0 \text{ cm}^{-1}$  (Figure 4.1.3d), another moiré pattern is distinctly distinguished. Through these results, we find out that the moiré pattern tDBLG has a wavelength. When the image is taken at  $980.5 \text{ cm}^{-1}$ , the intensity contrast difference between moiré pattern tDBLG A and B is decreased. Also, as shown in Figure 4.1.3f, high contrast lines (black arrow) begin to appear. At  $990.0 \text{ cm}^{-1}$ , two other types of lines are observed (Figure 4.1.3g). One has relatively high contrast (red arrows) and the other has low contrast (blue arrows). Those lines are assumed to be a saddle point (SP) of the stacked graphene<sup>22</sup>. Although it is difficult to clearly explain this phenomenon, we attribute that these SPs have an enormously narrow IR resonance. The reason why these two types of SPs can exist is that the graphene structure can be affected by strains (shear<sup>23,24</sup> or tensile<sup>25</sup>). Furthermore, the recently reported theoretical paper<sup>22</sup> supports this phenomenon. On the other hand, ironically, even though the SP's intensity has

changed, but there is no difference in IR-sSNOM intensity contrast between tDBG A and B. When the image is taken at  $1014.5\text{ cm}^{-1}$ , these lines become invisible (in Figure 4.1.3h). Also, the IR-sSNOM intensity contrast is almost the same, so the moiré pattern is invisible.

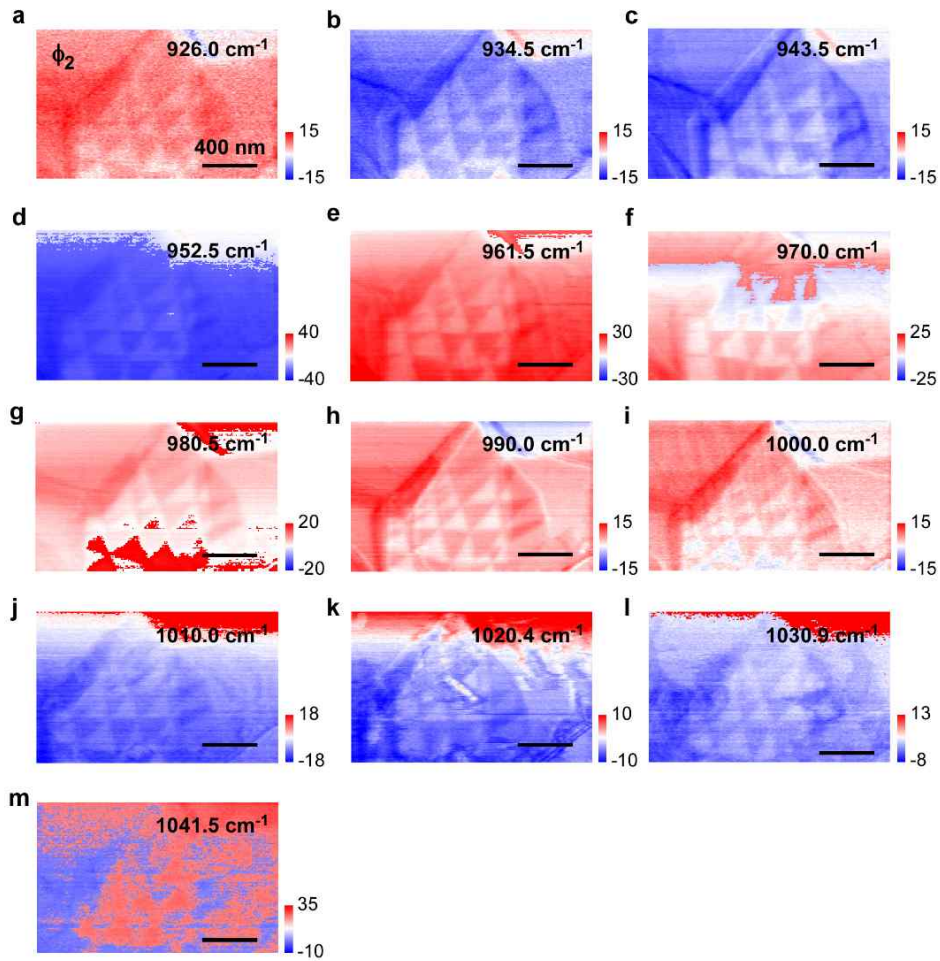


**Figure 4.1.4. Wavenumber dependence of near-field optical phase contrast changes of tDBG.** a-m, IR-sSNOM phase ( $\phi_2$ ) images of the tDBG obtained with IR light at  $\tilde{\nu} = 926.0$  (a), 934.5 (b), 943.5 (c), 952.5 (d), 961.5 (e), 970.0 (f), 980.5 (g), 990.0 (h), 1000.0 (i), 1010.0 (j) 1020.4 (k), 1030.9 (l) and 1041.5 (m)  $\text{cm}^{-1}$ . All scale bars in IR-sSNOM images are 400 nm. All of the IR-sSNOM phase images of moiré patterned tDBG is normalized to that of h-BN.

However, when looking at the IR-sSNOM phase images, the moiré pattern is clearly visible without wavelength dependence (see the IR-sSNOM phase images in Figure 4.1.4).

First of all, looking at all the IR-sSNOM intensity spectra (in Figure 4.1.3i), IR-sSNOM intensity spectra of tDBLG is quite similar to those of the Drude model. To comparing BLG with two tDBLG (A and B) of IR-sSNOM intensity spectra, it can be clearly seen that the optical conductivity of tDBLG B is similar to that of BLG, but that of tDBLG A is completely different from that of tDBLG B at specific regions (blue region in Figure 4.1.3i). To know how different optical property of these two tDBLGs is, we divide the intensity of tDBLG A by the intensity of tDBLG B (Figure 4.1.3j). Anomalously, tDBLG A has a very narrow infrared resonance, namely localized surface plasmon resonance (LSPR) in a specific region ( $\tilde{\nu} = 943.5 \sim 980.5 \text{ cm}^{-1}$ ). However, according to the previous study<sup>17,26</sup>, no LSPR has been reported in the corresponding region in graphene with a perfect Bernal and rhombohedral stacking structure.

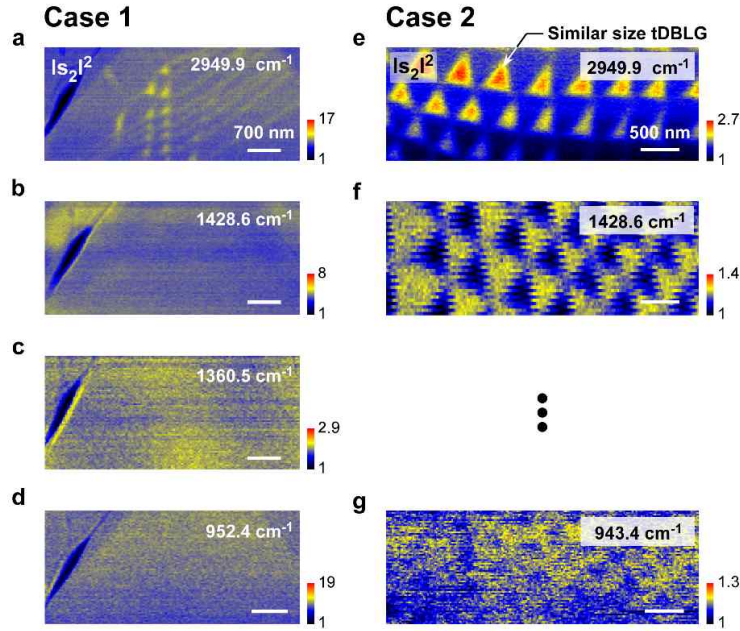


**Figure 4.1.5. Examples of IR-sSNOM intensity ( $|s_2|^2$ ) images of moiré patterned tDBG obtained with IR light. a-d**, IR-sSNOM intensity ( $|s_2|^2$ ) images of the another tDBG sample (case 1) obtained different wavenumber at  $\tilde{\nu} = 2949.9$  (a), 1428.6 (b), 1360.5 (c) and 952.4 (d)  $\text{cm}^{-1}$ . The scale bars in IR-sSNOM images a-d are 700 nm. **e-h**, IR-sSNOM intensity ( $|s_2|^2$ ) images of the other tDBG sample (case 2) obtained different wavenumber at  $\tilde{\nu} = 2949.9$  (e), 1428.6 (f) and 943.4 (g)  $\text{cm}^{-1}$ . The scale bars in IR-sSNOM images e-g are 500 nm.

It will be necessary to conduct additional experiments to see if this phenomenon such as LSPR is limited to this sample (see Figure 4.1.5 for more examples). Looking at case 1 of Figure 4.1.5, it was obviously confirmed the moiré pattern through IR-sSNOM imaging at  $\tilde{\nu} = 2949.9 \text{ cm}^{-1}$  (inter-band transition), but moiré pattern is invisible (see Figures 4.1.5b, c and d) in the particular wavenumber range (at  $\tilde{\nu} = 952.3 \sim 1428.5 \text{ cm}^{-1}$ ), even if moiré patterned tDBG have the similar size. Next, looking at Case 2 of Figure 4.1.5, the moiré pattern was well distinguished even at  $\tilde{\nu} = 1428.5$  and  $2949.9 \text{ cm}^{-1}$ , even if moiré patterned tDBG have the similar size. From these experimental results, it can be concluded that the all moiré pattern tDBG does not necessarily have remarkable optical properties in intra-band transition region, and it seems to be too sensitive to sample conditions.

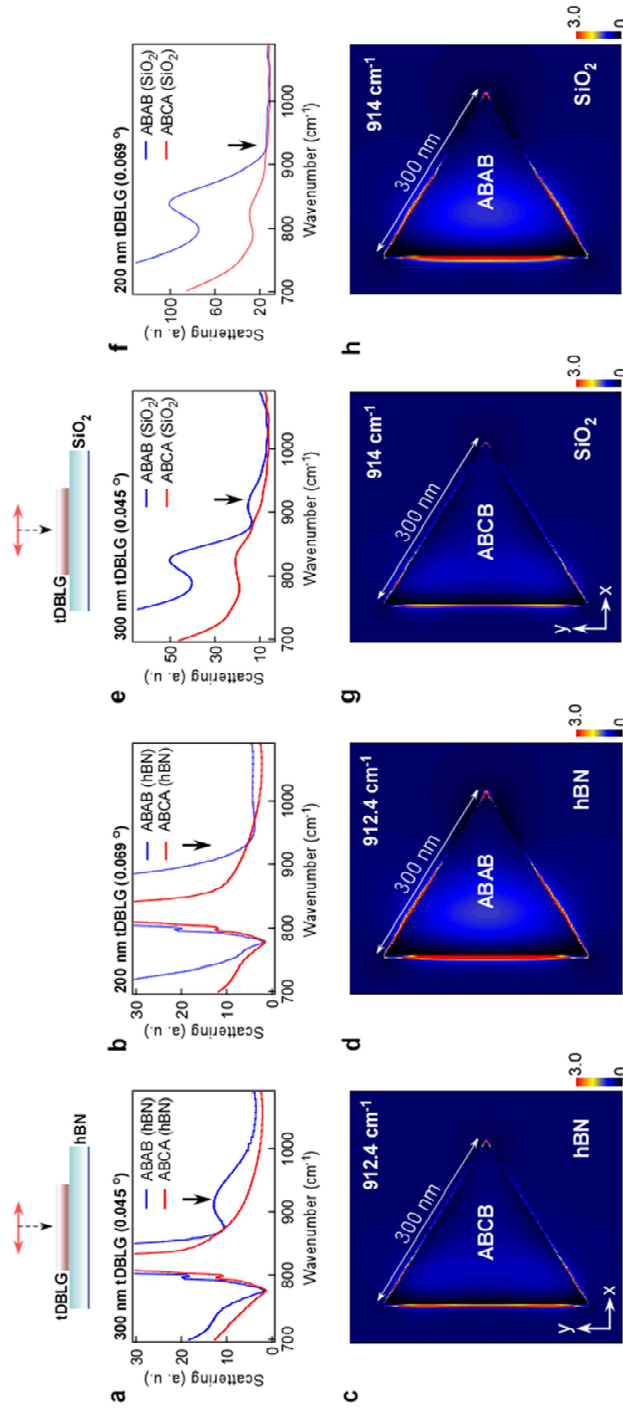


**Figure 4.1.6. Electromagnetic simulation of triangle structure.** **a-b**, Calculated scattering spectra of the ABAB / ABCB graphene triangle on h-BN / SiO<sub>2</sub> substrate with length = 300 (**a**) and 200 (**b**) nm. Peak appears at  $\tilde{\nu} = 912.4 \text{ cm}^{-1}$  (black arrow) in **a**. **c** and **d**, Intensity field map of ABAB / ABCB graphene triangle on h-BN / SiO<sub>2</sub> substrate at  $\tilde{\nu} = 912.4 \text{ cm}^{-1}$ , **e**, **f**, **g** and **h**, analogous results for graphene triangle on SiO<sub>2</sub> substrate without h-BN layer. Peak appears at  $\tilde{\nu} = 914.0 \text{ cm}^{-1}$  (black arrow) in **e**.

### **Numerical simulation depending on stacking structures, size and substrates**

Next, we carried out numerical electromagnetic simulation (finite-difference time-domain (FDTD) method, Lumerical Inc.), to find out where these abnormal resonance features stem from. Such resonance could be affected by stacking structures of graphene, the size of moiré structure, and also substrate. In particular, we calculated the local electric field and scattering spectra of modeled structure, various sizes of tetralayer graphene triangles stacked above the different substrates.

To investigate the effect of the stacking structure, we considered two fundamental stacking structure of tetralayer graphene, which are Bernal (ABAB) and rhombohedral (ABCB), where these conductivities were calculated by the method available in our previous report<sup>17</sup>. Figure 4.1.6a shows that ABAB and ABCB graphene triangle with 300 nm length sides have clearly different intensity at  $\tilde{\nu} = 912.4 \text{ cm}^{-1}$ .

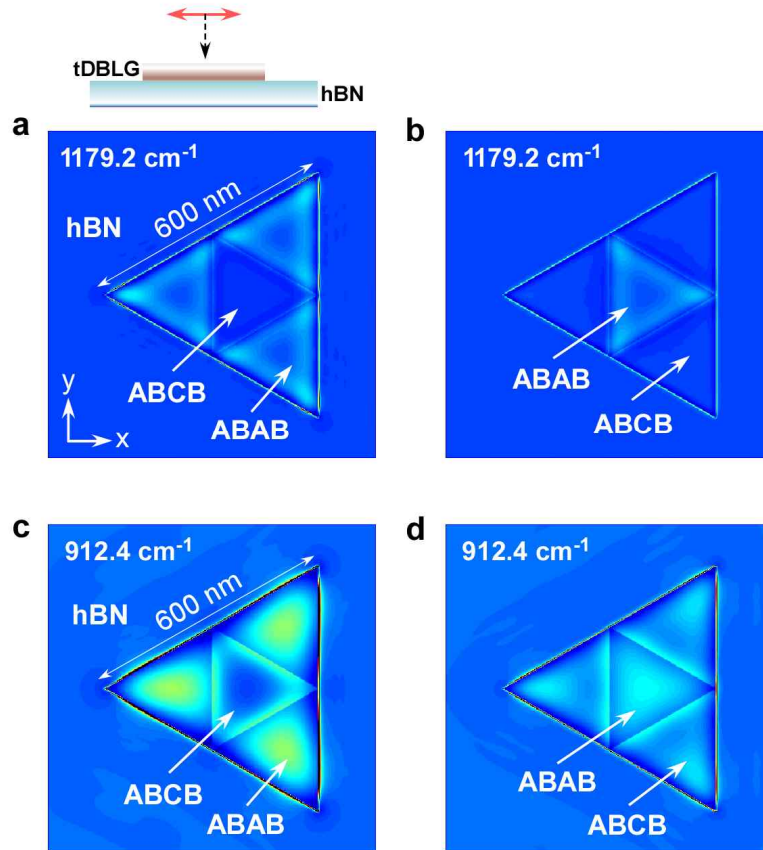


**Figure 4.1.7. Electromagnetic simulation of tDBLG structures.** a-d, Intensity field map of ABCB (a, c) / ABAB (b, d) centered tDBLG graphene structures on h-BN substrate at  $\tilde{\nu} = 1179.2 \text{ cm}^{-1}$ .(a-b) and  $\tilde{\nu} = 912.4 \text{ cm}^{-1}$ .(c-d).

In common with ABAB and ABCB, the intensity field maps (see Figure 4.1.7) show the electric field was confined on the edges. However, in case of ABAB, we can find that the field was also localized across the interior of the graphene triangle, and that is where the LSPR comes from. These spectral features disappeared when the length of the triangle was reduced to 200 nm (Figure 4.1.6b), clearly showing the size-dependence of LSPR. Furthermore, the calculation using simple Drude model<sup>27</sup> without consideration of inter-band transition and stacking structure shows more significant size-dependence. It can also be seen that such LSPR spectral features were almost preserved when substrate condition was changed. (Figures

4.1.6a and e) With or without 30 nm h-BN layer below the graphene, the localized electric field was similar (Figures 4.1.6d and h) and peak appears near at  $\tilde{\nu} = 914$   $\text{cm}^{-1}$  (Figures 4.1.6a and e) in both cases.

#### **4.1.4 Conclusions**

From all spectroscopic measurement and calculation above, we can interpret these results that it should be considered that each moiré patterned tDBLG sample has different and unique characteristics, even if they have the same size. Although, it cannot be interpreted accurately these differences, we carefully speculate that there will be differences in the arrangement of moiré patterns, the shape of the pattern, the edge around the pattern, or something else we didn't recognize. If we make good use of tDBLG, which has such numerous capabilities, it is expected to emerge as an advanced sensor material. In addition, we think such research will be of great help in the development of the twistronics field.

## 4.1.5 References

- 1 Basov, D. N., Fogler, M. M. & García de Abajo, F. J. Polaritons in van der Waals materials. *Science* **354**, aag1992, doi:10.1126/science.aag1992 (2016).
- 2 Gustafsson, M. G. L. Surpassing the lateral resolution limit by a factor of two using structured illumination microscopy. *Journal of Microscopy* **198**, 82-87, doi:10.1046/j.1365-2818.2000.00710.x (2000).
- 3 Carr, S. *et al.* Twistronics: Manipulating the electronic properties of two-dimensional layered structures through their twist angle. *Physical Review B* **95**, 075420, doi:10.1103/PhysRevB.95.075420 (2017).
- 4 Cao, Y. *et al.* Unconventional superconductivity in magic-angle graphene superlattices. *Nature* **556**, 43-50, doi:10.1038/nature26160 (2018).
- 5 Zhu, Z., Carr, S., Massatt, D., Luskin, M. & Kaxiras, E. Twisted Trilayer Graphene: A Precisely Tunable Platform for Correlated Electrons. *Physical Review Letters* **125**, 116404, doi:10.1103/PhysRevLett.125.116404 (2020).
- 6 Haddadi, F., Wu, Q., Kruchkov, A. J. & Yazyev, O. V. Moiré Flat Bands in Twisted Double Bilayer Graphene. *Nano Letters* **20**, 2410-2415, doi:10.1021/acs.nanolett.9b05117 (2020).
- 7 Shen, C. *et al.* Correlated states in twisted double bilayer graphene. *Nature Physics* **16**, 520-525, doi:10.1038/s41567-020-0825-9 (2020).
- 8 Luo, Y. *et al.* In situ nanoscale imaging of moiré superlattices in twisted van der Waals heterostructures. *Nature Communications* **11**, 4209, doi:10.1038/s41467-020-18109-0 (2020).
- 9 Voloshina, E. N. *et al.* Electronic structure and imaging contrast of graphene moiré on metals. *Scientific Reports* **3**, 1072, doi:10.1038/srep01072 (2013).
- 10 Lu, C.-I. *et al.* Moiré-related in-gap states in a twisted MoS<sub>2</sub>/graphite heterojunction. *npj 2D Materials and Applications* **1**, 24, doi:10.1038/s41699-017-0030-6 (2017).
- 11 Murakami, K., Kadowaki, T. & Fujita, J.-i. Damage and strain in single-layer graphene induced by very-low-energy electron-beam irradiation. *Applied Physics Letters* **102**, 043111, doi:10.1063/1.4790388 (2013).
- 12 Kobayashi, K. Moiré pattern in scanning tunneling microscopy: Mechanism in observation of subsurface nanostructures. *Physical Review B* **53**, 11091-11099, doi:10.1103/PhysRevB.53.11091 (1996).
- 13 Chen, X. *et al.* Moiré engineering of electronic phenomena in correlated oxides. *Nature Physics* **16**, 631-635, doi:10.1038/s41567-020-0865-1 (2020).

- 14 Wang, J., Bo, W., Ding, Y., Wang, X. & Mu, X. Optical, optoelectronic, and photoelectric properties in moiré superlattices of twist bilayer graphene. *Materials Today Physics* **14**, 100238, doi:<https://doi.org/10.1016/j.mtphys.2020.100238> (2020).
- 15 Fei, Z. *et al.* Edge and Surface Plasmons in Graphene Nanoribbons. *Nano Letters* **15**, 8271-8276, doi:10.1021/acs.nanolett.5b03834 (2015).
- 16 Jeong, G. *et al.* Mapping of Bernal and non-Bernal stacking domains in bilayer graphene using infrared nanoscopy. *Nanoscale* **9**, 4191-4195, doi:10.1039/C7NR00713B (2017).
- 17 Kim, D.-S. *et al.* Stacking Structures of Few-Layer Graphene Revealed by Phase-Sensitive Infrared Nanoscopy. *ACS Nano* **9**, 6765-6773, doi:10.1021/acsnano.5b02813 (2015).
- 18 Sunku, S. S. *et al.* Photonic crystals for nano-light in moiré graphene superlattices. *Science* **362**, 1153-1156, doi:10.1126/science.aau5144 (2018).
- 19 Wang, K. *et al.* Strain Engineering Modulates Graphene Interlayer Friction by Moiré Pattern Evolution. *ACS Applied Materials & Interfaces* **11**, 36169-36176, doi:10.1021/acscami.9b09259 (2019).
- 20 Artaud, A. *et al.* Universal classification of twisted, strained and sheared graphene moiré superlattices. *Scientific Reports* **6**, 25670, doi:10.1038/srep25670 (2016).
- 21 Preobrajenski, A. B., Nesterov, M. A., Ng, M. L., Vinogradov, A. S. & Mårtensson, N. Monolayer h-BN on lattice-mismatched metal surfaces: On the formation of the nanomesh. *Chemical Physics Letters* **446**, 119-123, doi:<https://doi.org/10.1016/j.cplett.2007.08.028> (2007).
- 22 Lebedeva, I. V. & Popov, A. M. Energetics and Structure of Domain Wall Networks in Minimally Twisted Bilayer Graphene under Strain. *The Journal of Physical Chemistry C* **124**, 2120-2130, doi:10.1021/acs.jpcc.9b08306 (2020).
- 23 Wang, G. *et al.* Measuring Interlayer Shear Stress in Bilayer Graphene. *Physical Review Letters* **119**, 036101, doi:10.1103/PhysRevLett.119.036101 (2017).
- 24 Gan, L. *et al.* Shear-induced orientation of functional graphene oxide sheets in isotactic polypropylene. *Journal of Materials Science* **51**, 5185-5195, doi:10.1007/s10853-016-9820-z (2016).
- 25 Min, K. & Aluru, N. R. Mechanical properties of graphene under shear deformation. *Applied Physics Letters* **98**, 013113, doi:10.1063/1.3534787 (2011).
- 26 Yu, R., Cox, J. D., Saavedra, J. R. M. & García de Abajo, F. J. Analytical Modeling of Graphene Plasmons. *ACS Photonics* **4**, 3106-3114,

doi:10.1021/acsp Photonics.7b00740 (2017).

- 27 Horng, J. *et al.* Drude conductivity of Dirac fermions in graphene. *Physical Review B* **83**, 165113, doi:10.1103/PhysRevB.83.165113 (2011).

## **Chapter 5:**

### **Studies of selective chemical reaction on graphene surface**

## 5.1 Stacking-specific reversible oxidation of bilayer graphene

- This paper will be published.

### 5.1.1 Introduction

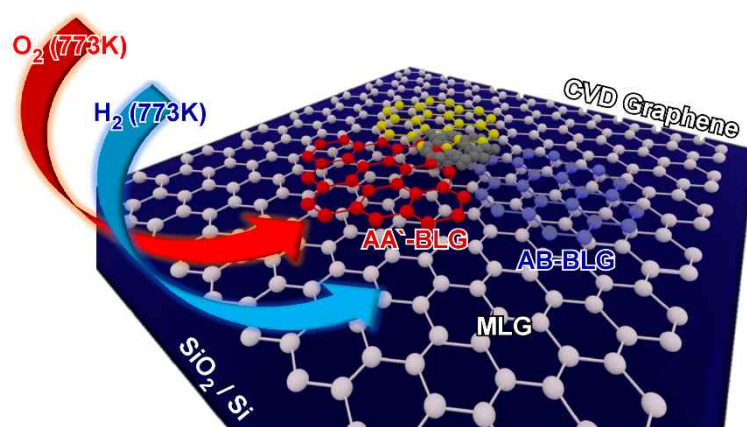


**Figure 5.1.1** Schematic illustration of redox reaction of bilayer graphene (a) Possible stacking structures of bilayer graphene

Since its first discovery, numerous studies on graphene have been made to utilize its unique physical and chemical properties. As a part of the endeavor to exploit the outstanding features of graphene, modification of electronic properties of graphene through chemical, physical and contact-mediated doping method was proposed<sup>1,2</sup>. Accompanied by such advancements, bilayer graphene (BLG) was spotlighted for its facile tunability of bandgap that can be controlled by stacking angles, external electric field, or chemical doping<sup>3,4</sup>. It was also reported that BLG can change from a superconductor to an insulator by simply changing its stacking angle<sup>5,6</sup>. However, with exfoliated BLG, exploring such stacking-specific properties of BLG is difficult due to its complicated fabrication processes<sup>7,8</sup>, and thus is hard to

be fully implemented in practical devices. On the other hand, the graphene layers synthesized by chemical vapor deposition (CVD) methods are reported to form BLGs *in situ*, which is relevant for practical applications, including chemical sensors<sup>9</sup>, barrier films<sup>10,11</sup>, fuel cells<sup>12</sup>, batteries<sup>13</sup>, *etc.* The exfoliated BLGs dominantly show the AB-stacked structures with carbons on the upper layer is positioned in the middle of the hexagonal lattice on the lower layer, while the CVD-grown BLGs show various stacking orders, which provides a better system to study various stacking-dependent phenomena. While some studies have been carried out to characterize the structures of oxidized monolayer graphene (MLG)<sup>14,15</sup>, there has been no study on the stacking-specific chemical reactivities of BLGs.

In this study, we, for the first time, show that O<sub>2</sub> and H<sub>2</sub> flow at elevated temperature can induce fully reversible redox reactions of CVD-grown BLG without introducing additional defects, which is different from the redox reactions of epitaxially grown<sup>16</sup> or exfoliated<sup>17</sup> samples. More importantly, we observe that the oxidized Bernal (AB) and non-Bernal (AA') stacked BLG show drastically different Raman spectral features (peak-shifts and line-shapes), strongly suggesting that the two structures produce two different oxide products. The *ab initio* molecular dynamics (AIMD) simulation of the oxidation of BLG further corroborates the stacking-specific chemical reactivities of BLG.

## 5.1.2 Experiment

**Reversible redox reaction** - The sample (Fig. 5.1.2; see methods for sample preparation procedure) is comprised of a  $\text{SiO}_2/\text{Si}$  substrate uniformly covered with mono-layer graphene (MLG) and an additional graphene layer island (diameters of  $\sim 10\ \mu\text{m}$ ) formed on top of the MLG. The islands provide BLG with a various stacking domains. The sample was placed in a vacuum furnace and heated to 873 K with the  $\text{O}_2$  (g) flow of 100 ml / min or  $\text{H}_2$  (g) flow of 150 ml / min to induce oxidation and reduction of BLG (see Fig 5.1.2).

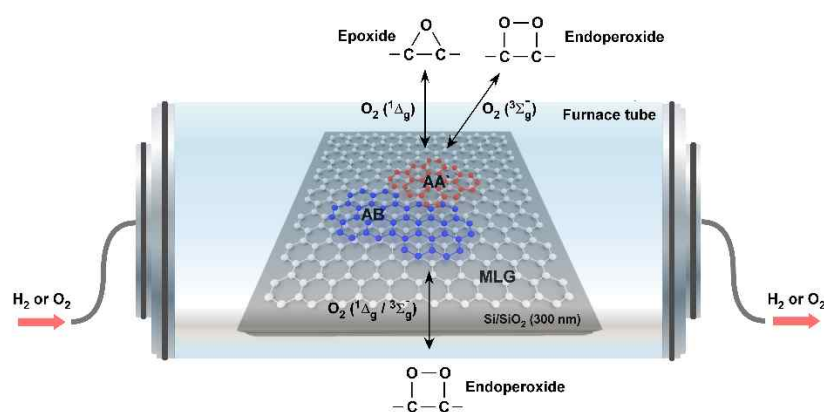


**Figure 5.1.2. Schematic illustration of oxidation / reduction processes of BLG.** The BLG on  $\text{SiO}_2/\text{Si}$  wafer is placed in a quartz tube at the temperature of 873 K, and  $\text{O}_2$  (g) and  $\text{H}_2$  (g) are flowed through the vacuum furnace at the flow rates of 100 ml / min and 150 ml / min respectively.

**Sample preparation (CVD bilayer graphene)** - Graphene films were synthesized on 25  $\mu\text{m}$  thick copper foil through the CVD method using methane (50 s.c.c.m.) and hydrogen (5 s.c.c.m.) gas with vacuum pumping ( $\sim 1.5$  mtorr) at 1000  $^\circ\text{C}$  for  $\sim 2$  hours. Methane was used only during the growth stages of graphene and was not used during the cooling process. Poly (methyl methacrylate) (PMMA) was spin-coated on top of graphene, and the copper foil was etched in an ammonium persulfate

solution (20 mM with distilled water). The achieved monolayer graphene films were transferred onto SiO<sub>2</sub> (thickness of 285 nm) / Si substrates. The monolayer covers nearly all areas of the SiO<sub>2</sub>/ Si substrate, and bilayer domains appear as islands with an average radius of  $\sim 10 \mu\text{m}$ .

**Sample measurements (FTIR, Raman & IR-sSNOM)** - FTIR measurements were carried out on the graphene sample with Perkin Elmer Spotlight 400. Micro-Raman spectroscopy measurements (an excitation wavelength of 514.5 nm) are carried out on the sample to determine the redox states of BLG. We employ side-illuminated IR-sSNOM (home-built) equipped with an infrared laser (an infrared HeNe laser at  $\lambda = 3.39 \mu\text{m}$ ), and liquid-nitrogen cooled InSb detectors. The IR-sSNOM probe (Nanosensors, PPP-NCHPt,  $\Omega \sim 300 \text{ kHz}$ ) vertically vibrates with an amplitude of 20 – 100 nm. A Linearly polarized IR-light is focused on the tip-sample junction with an angle of 30° via a Schwarzschild objective lens. The collected scattered light is amplified by a homodyne-amplified by a Michelson interferometer and a lock-in amplifier to obtain the intensity ( $|s_2|^2$ ) and phase ( $\phi_2$ ) IR-sSNOM signals. The IR-sSNOM data shown in main text refers to the intensity signals.

**Computational methods** - All *ab initio* molecular dynamics (AIMD) simulations were carried out with Vienna *ab initio* simulation package (VASP, version 5.3.5)<sup>18</sup>. Simulation results were visualized with Visualization for Electronic and STructural Analysis (VESTA) and Visual Molecular Dynamics (VMD) programs<sup>19,20</sup>. The electron-ion interaction was described by projector augmented wave (PAW) method<sup>21,22</sup> with 520.0 eV kinetic energy cutoff for plane waves. Perdew-Burke-

Ernzerhof (PBE) exchange-correlation functional<sup>23</sup> is used for density functional theory (DFT) calculations and zero damping DFT-D3 method of Grimme<sup>24</sup> is employed to consider van der Waals interactions. Both spin-polarized and spin-unpolarized calculations were performed to apply triplet and singlet spin state of O<sub>2</sub> respectively. In all AIMD simulations, Brillouin zone was sampled at only  $\Gamma$  point, time-step was set to 1 fs, and the temperature was controlled by Nosé thermostat of 873 K in the canonical ensemble.

To construct the model system of AB-BLG and AA'-BLG, rectangular shaped two dimensional primary unit-cell with C-C bond length of 1.42 Å was generated at first ( $a = 2.46$  Å;  $b = 4.26$  Å). Then, the square shaped layer **A** ( $a = 12.54$  Å) consisted of 60 carbon atoms was created by extending rectangular primary unit-cell (5-fold to  $a$ -axis and 3-fold to  $b$ -axis) and modifying axis lengths (lengthening  $a$ -axis two percent and shortening  $b$ -axis two percent). The second layer for Bernal stacking (**B**) was made by translating layer **A**, and the second layer for non-Bernal stacking (**A'**) was made by rotating 90 degrees and translating layer **A** (**A** and **A'** have crystallographic angle of 30 degrees or 90 degrees since graphene has 6-fold symmetry). Finally, three dimensional AB-BLG or AA'-BLG was created by locating the layer **B** or layer **A'** 3.35 Å below the layer **A**, respectively. Afterward, four oxygen molecules with the O-O bond length of 1.21 Å were located parallel to the graphene 1.3 Å above the carbon of layer (**B** and **A'**) to make an initial geometry for simulations. Hence, in all respective simulations, upper graphene layer (**B** and **A'**) and oxygen molecules have exactly same atomic coordinates initially. Also, bottom graphene layers (**A**) were fixed not to move while upper graphene layer (**B** and **A'**) and oxygen molecules were allowed to move throughout the simulations. Vacuum layer larger than 15 Å was inserted above the oxygen molecules to prevent the interaction between unit-

cells, and oxygen molecules that flew away over 5 Å were deleted during the simulation to avoid the collision with the upper unit-cell.

### 5.1.3 Results and Discussion

#### Spectroscopic Signatures of the Reversible Oxidation

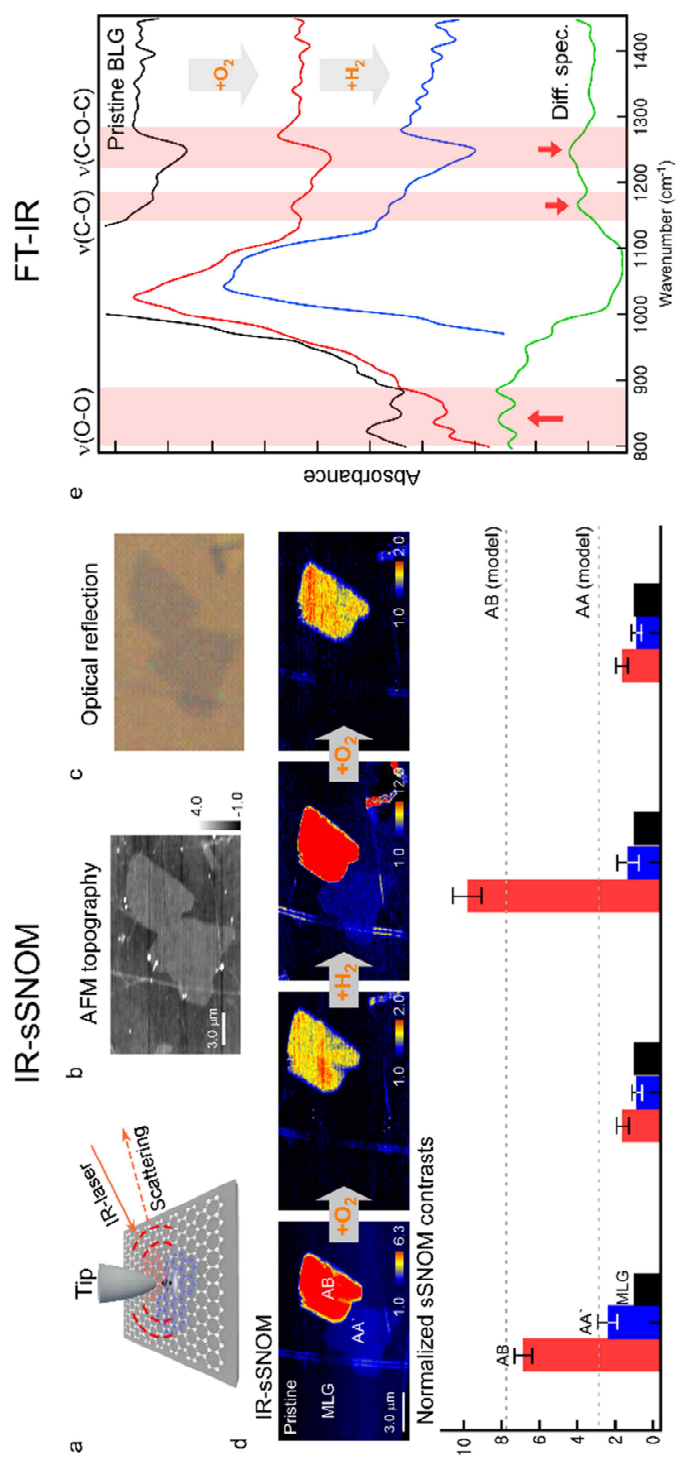


**Figure 5.1.3. Changes in the IR-sSNOM contrasts and the IR spectra of BLG upon O<sub>2</sub> / H<sub>2</sub> exposure.** **a**, Schematic diagram of IR-sSNOM. **b**, AFM image of BLG grown on top of monolayer graphene (MLG). **c**, Optical reflectance (OR) microscopy image of **b**. **d**, IR-sSNOM intensity images of the BLG / MLG sample obtained with IR laser at  $\lambda = 3.39 \mu\text{m}$ , and the contrast change upon exposure to O<sub>2</sub> and H<sub>2</sub>. The color scale is normalized to the IR-sSNOM intensity of MLG sampled from each image. The bar graphs in the bottom panel represent the average IR-sSNOM intensities (normalized to MLG contrast) for AB (red), AA' (blue), and MLG (black) graphene. The error bars are the fwhm of the image pixel histogram (see Supporting Information S5.1.1) corresponding to domain. The dashed lines in the bar graph represent the model contrasts for AB and AA'-stacked BLG, derived from dipolar tip-sample coupling model and the theoretical conductivities (see Supporting Information figure S5.1.1 and S5.1.2). **e**, Enlarged FT-IR spectra of pristine (black), oxidized (red) and reduced (blue) graphene. The differential spectrum (green) shows peaks at  $800 \sim 900 \text{cm}^{-1}$ ,  $1160 \text{cm}^{-1}$ , and  $1260 \text{cm}^{-1}$ , which could be assigned as the stretching of endoperoxide (-C-O-O-C-), stretching of C-O stretching, and stretching of epoxide (C-O-C).

The structural changes in BLG upon O<sub>2</sub> and H<sub>2</sub> exposure were investigated with the micro Fourier-transform infrared (FT-IR) absorption spectroscopy, infrared scattering scanning near-field microscopy (IR-sSNOM, or simply IR-nanoscopy) and Raman spectroscopy. The IR-sSNOM measurement was performed to observe the changes in the local IR-conductivity of graphene. The IR-sSNOM records light scattering from atomic force microscopy (AFM) tip and the sample junction (see Figure 5.1.3a). The IR-sSNOM image contrast is determined by the local dielectric properties of the samples and the near-field tip-sample coupling. In the particular case of graphene on SiO<sub>2</sub>/ Si substrate, the IR-sSNOM contrast reflects the local IR-conductivity ( $\sigma$ ) of monolayer and few-layer graphene<sup>25</sup>. The IR-conductivity of graphene is influenced by many factors, including the number of graphene layers, stacking structures<sup>25</sup>, electronic transition resonances, and doping levels. In this experiment, the IR laser is tuned at  $\lambda = 3.39 \mu\text{m}$ , which is on and off-resonant with inter-band transitions of AB-BLG and AA'-BLG, respectively<sup>25,26</sup>. This makes contrast ordering of AB-BLG > AA'-BLG > MLG<sup>26</sup>.

In the particular sample shown in Figures 5.1.3b-c, atomic force microscopy (AFM) and optical reflection microscopy (OR) images show two islands of BLG with the same topographic height and optical reflection, whereas the corresponding IR-sSNOM intensity images (Figure 5.1.3d, upper panels; The images represent the  $|s_2|^2$ -map, the square modulus of the 2<sup>nd</sup> harmonic component of IR-sSNOM signal) show distinctly different intensity contrasts for the two. The images and the associated contrast plots (Figure 5.1.3d, lower panel) are normalized to the signals of MLG domains sampled from the corresponding images. Based on the contrast analysis and the modeling of IR-sSNOM contrast<sup>26</sup> (dashed lines in the lower panel of Figure 5.1.3d; see also chapter 1.4 Point-dipole Modeling for IR s-SNOM), we assign that the one with stronger IR-sSNOM contrast is AB-BLG and the other one is AA'-BLG. The AB-BLG shows large intensity contrast compared with those of MLG or AA', because the inter-band transition of pristine AB-BLG (0.37 eV) is resonant with the frequency of the IR-laser used (0.366 eV). Also, note that the IR-sSNOM contrast model reliably predicts the contrasts of AB-BLG and MLG, whereas it provides only a rough estimate for the contrast of AA'-BLG. For this reason, the domain-assignment is further cross-checked by a separate Raman spectroscopy. Figure 5.1.3d also shows a series of IR-sSNOM images (upper panel) and the associated intensity contrasts (lower panel) of AB-BLG and AA'-BLG, which drastically change upon exposure to O<sub>2</sub> and H<sub>2</sub>. When the pristine sample is exposed to O<sub>2</sub>, we observe decrease in the IR-sSNOM contrasts of AB-BLG and AA'-BLG. Furthermore, the AA' / MLG contrast ratio is reduced below unity. Upon exposure to H<sub>2</sub>, the image contrast is fully recovered to initial values. These show that O<sub>2</sub> and H<sub>2</sub> exposure reversibly modulate the local optical conductivities of AB-BLG and AA'-BLGs, while maintaining the shapes of AB and AA' domains. The

modulation in optical conductivities most likely arise from the reversible oxidation and reduction, altering band-structures and doping levels of BLG. The contrast modulation is the most pronounced for AB-BLG, because the inter-band transition of pristine AB-BLG (0.37 eV) is resonant with the frequency of the IR-laser used (0.366 eV).

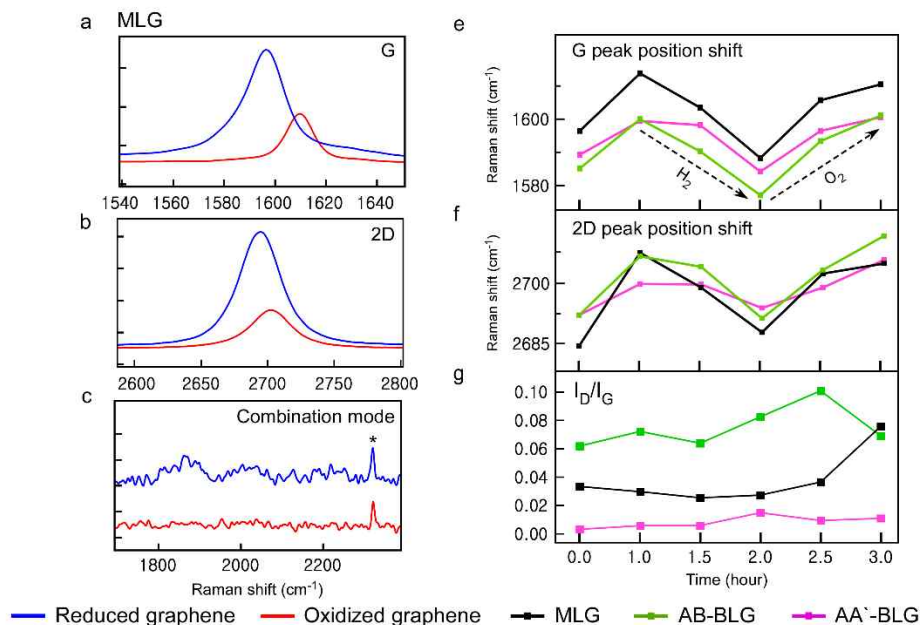


**Figure 5.1.4. Raman spectral changes of MLG following the O<sub>2</sub> and H<sub>2</sub> exposure.** a-c, G, 2D, and combination-mode peaks of Raman spectra of MLG before (blue) and after (red) the exposure to O<sub>2</sub>. d-f, Comparison of the Evolutions of G-peak center position (d), 2D peak position (e), and ratio of D and G peak intensities ((f), I<sub>D</sub> / I<sub>G</sub>) of AB-BLG (green), AA'-BLG (violet) and MLG(black) under the H<sub>2</sub> and O<sub>2</sub> exposure.

The possible modulation of the optical conductivity of MLG is not evident from the IR-sSNOM images because the normalized IR-sSNOM contrasts can probe only the relative changes. However, through the Raman spectroscopy measurement, we indirectly confirm that similar reversible changes also occur for MLG as well. (see Figure 5.1.4)

To directly probe the oxides on the BLG, we have carried out a micro-infrared (IR) absorption measurement on the sample, using the micro-Fourier

transform IR (FT-IR) spectrometer. Due to the limitation of the spatial resolution, the sampled area ( $6\ \mu\text{m} \times 6\ \mu\text{m}$ ) includes regions of MLG as well as the BLG. The FT-IR spectrometer resolution was set at  $2\ \text{cm}^{-1}$ , and the scan number at 120 s. The measurement was performed over the same area wider than  $6.25\ \mu\text{m}$  by  $6.25\ \mu\text{m}$ , but MLG was also measured with BLG due to the diffraction limit. The FT-IR and Raman spectra were obtained for five times, and the average was taken for the result. In addition, every spectrum was normalized with respect to those of blank  $\text{SiO}_2$  wafer without graphene. Figure 5.1.3e shows how the FT-IR spectrum of the pristine BLG sample (black) changes upon  $\text{O}_2$ -exposure (red) and the subsequent exposure to  $\text{H}_2$ -gas (blue). We find that two new peaks at  $1160\ \text{cm}^{-1}$  and  $1250\ \text{cm}^{-1}$ , which can be assigned as the stretching modes of  $\text{C-O}^{21}$ , and epoxide ( $\text{C-O-C}$ )<sup>22, 23</sup> on graphene, appear and disappear upon  $\text{O}_2$  and  $\text{H}_2$  exposure. In the bottom of the Figure 5.1.3a, we have also shown the differential spectrum, the spectrum of the  $\text{O}_2$ -exposed sample minus that of the pristine sample, better showing the two vibrational peaks. The difference spectrum also shows a broad (positive) feature at  $800\text{-}1000\ \text{cm}^{-1}$ . The assignment of the feature is rather inconclusive: it may indicate highly heterogeneously broadened O-O stretching of endoperoxide ( $-\text{C-O-O-C}-$ )<sup>27</sup>, or the change in intra-band conductivity of graphene upon oxidation. Additionally, the change accompanies a reversible change in the line-shapes of  $\text{SiO}_2$  phonon peak ( $1000\text{-}1200\ \text{cm}^{-1}$ ), which may arise from the change in the surface phonon states of  $\text{SiO}_2$  caused by the oxidized graphene.

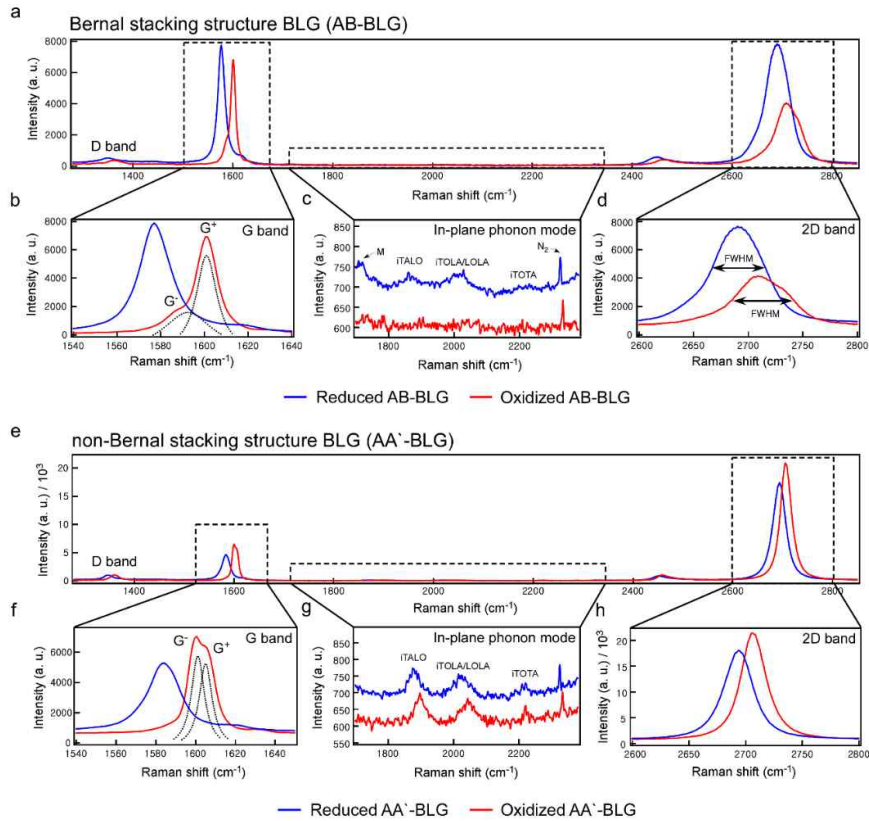


**Figure 5.1.5. Wide-range Raman spectrum of AB- and AA'-BLG before and after oxidation.** **a**, Wide range Raman spectra of Bernal- stacked BLG before and after oxidation. **b**, Changes in the G band shape through reduction and oxidation. **c**, Changes in In-plane phonon mode. **d**, Changes in the 2D band shape through reduction and oxidation. **e**, Wide range Raman spectra of non-Bernal-stacked BLG before and after oxidation. **f**, Changes in G band shape through reduction and oxidation. **g**, Changes in the In-plane phonon mode. **h**, Changes in the 2D band shape through reduction and oxidation.

As in the case of FT-IR and IR-sSNOM results, the Raman scattering spectra of AB-BLG and AA'-BLG reversibly change upon O<sub>2</sub> and H<sub>2</sub> exposure (Figure 5.1.5; Raman spectra of BLG, covering wider range of spectral window), which may arise from the mechanical strain<sup>28</sup> and / or the chemical-doping<sup>16</sup> caused by the oxides on BLG. For the particular data shown, the stacking angle of AA'-BLG is estimated to be<sup>29</sup>  $\theta \sim 26^\circ$ .

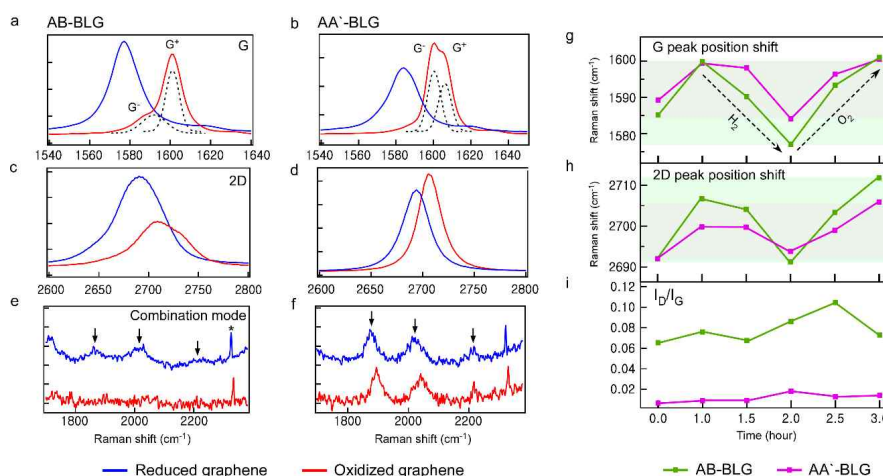


**Figure 5.1.6. Raman spectral changes of AB and AA'-BLG following the O<sub>2</sub> and H<sub>2</sub> exposure.** a-f, G, 2D, and combination-mode peaks of Raman spectra of AB-BLG (a, c, e) and AA'-BLG (b, d, f) before (blue) and after (red) the exposure to O<sub>2</sub>. After the exposure to O<sub>2</sub>, G-peak is split into two components (G<sup>+</sup> and G<sup>-</sup>), which are fitted to two Lorentzian functions (dashed curves). The peak at 2331 cm<sup>-1</sup> (marked in \* in e) appearing in e and f is the Raman peak of the ambient N<sub>2</sub> gas present. g-i Evolutions of G-peak center position (g), 2D peak position (h), and ratio of D and G peak intensities ((i), I<sub>D</sub> / I<sub>G</sub>) of AB-BLG (green) and AA'-BLG (violet) under the H<sub>2</sub> and O<sub>2</sub> exposure. Shaded regions in (g) and (h) refer to the ranges of center frequency changes of G and 2D peaks of AB-BLG (green) and AA'-BLG (purple).

The most pronounced changes are the peak-center shifts of G and 2D peaks (Figures 5.1.6a-d, g, h), indicating the doping level changes induced by the redox reaction. The line-shapes of G peaks of pristine and reduced AB-BLG (blue trace in Figure 5.1.6a) and AA'-BLG (blue trace in Figure 5.1.6b) are nearly identical to each other, and they appear as a single peak (with a fwhm of 20 cm<sup>-1</sup>), corresponding to the doubly degenerate E<sub>2g</sub> phonon vibration of BLG<sup>8,30,31</sup>. Upon oxidation (red traces in Figures 5.1.6a and b), the single G-peak is split into two components (denoted as G<sup>+</sup> and G<sup>-</sup>). The G-peak splitting can arise from uniaxial mechanical strain<sup>32</sup> induced by oxides, lifting the degeneracy of E<sub>2g</sub> -mode frequency, or from the asymmetric doping induced by oxides, leading to the mixing of E<sub>2g</sub> (Raman-active) and E<sub>u</sub> (Raman-inactive) phonon modes<sup>33</sup>. The D versus G peak intensity ratio (I<sub>D</sub> / I<sub>G</sub>),

which is a widely accepted measure of the defect-density on graphene, remain nearly unchanged (see Figure 5.1.6i) during these reversible processes. This clearly shows that the redox cycles do not generate additional defects on BLG.

We also note that above-mentioned spectral changes are different for AB and AA'-BLG, strongly suggesting that the AB and AA'-BLG may have different redox reactivities and / or generate different kinds of oxide products. Specifically, when exposed to the same dosage of H<sub>2</sub> and O<sub>2</sub>, the magnitudes of peak-center shifts in G and 2D peaks (Figures 5.1.6g and h; see the shaded regions), the magnitude of G-peak splitting ( $\Delta\nu_G = \nu_{G^+} - \nu_{G^-}$ ), and the intensity ratios of the  $\nu_{G^+}$  and  $\nu_{G^-}$  components ( $I_{G^+} / I_{G^-}$ ) are different for AB and AA'-BLG. Additionally, we find that reduced AB and AA'-BLG both show combination-mode peaks at 1860 cm<sup>-1</sup>, 1983 cm<sup>-1</sup>, and 2220 cm<sup>-1</sup><sup>34,35</sup>. Upon oxidation, these peaks of AB-BLG completely disappear, whereas those of AA'-BLG remain nearly unchanged (see Figures 5.1.6e and f). As previously shown<sup>34</sup>, the peak positions and intensities of the combination peaks of graphite and few-layer graphene critically depend on the number of layers, doping, and stacking<sup>36</sup>. Overall, the observed differences suggest different reactivities and / or different oxide structures of AB and AA'-BLG.

Overall, FT-IR spectra, IR-sSNOM images, and Raman spectra show that exposure to O<sub>2</sub> and H<sub>2</sub> under elevated temperature lead to reversible oxidation and reduction processes without apparent increase defect densities (Figures 5.1.6g-i). More importantly, the result suggests that the oxide structure and / or reactivities are different for differently stacked BLGF. We find that such reversible change occur only for the mild reaction condition described above: Prolonged exposure to O<sub>2</sub> (> 3 hrs) at an elevated temperature generates irreversible formation of etch pits<sup>17</sup> in AB and AA'-BLG, which is accompanied by the drastic increase in D peak in the Raman

spectra. To better characterize the oxidized sample, we have attempted to carry out the high-resolution electron microscopy measurement (CS-corrected STEM), but without success: the grids for the TEM could not withstand harsh oxidation condition employed, and the PMMA (poly(methyl methacrylate)) and ammonium persulfate residues further impeded the measurement.

## *Ab initio* molecular dynamics (AIMD) simulation

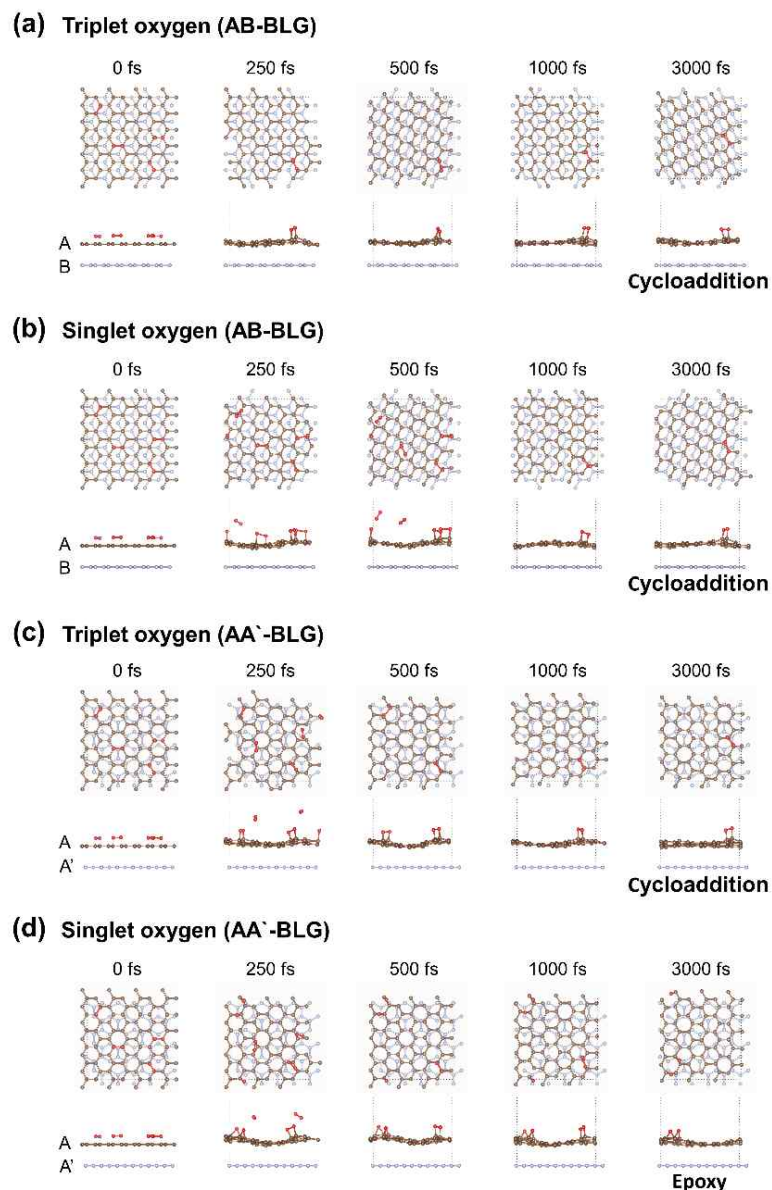


**Figure 5.1.7.** Temporal top view (top) and side view (bottom) snapshots from the AIMD simulation of Bernal stacked bilayer graphene (AB) with (a) four triplet oxygen molecules or (b) four singlet oxygen molecules and non-Bernal stacked bilayer graphene (AA') with (c) four triplet oxygen molecules or (d) four singlet molecules. Atomic coordinates of the upper graphene layer (A) and oxygen molecules are exactly same initially in all simulations. Oxygen, carbon of the upper graphene layer (A), and carbon of the bottom graphene layer (B or A') are colored with red, brown, and sky-blue, respectively.

To explore possible reactivity and oxide-structure differences between AB-BLG and AA'-BLG, we have carried out an *ab initio* molecular dynamics (AIMD) simulation (see Figure 5.1.7, based on density functional theory (DFT) calculation with periodic boundary condition (see Methods for detail). Four ground-state triplet oxygen ( $^3\text{O}_2$ ,  $^3\Sigma_g^-$ ; Figures 5.1.8b-c) and four excited-state singlet  $\text{O}_2$  ( $^1\text{O}_2$ ,  $^1\Delta_g$ ; Figures 5.1.8b and d) are initially positioned (physi-sorbed) on AB and AA'-BLG, and the time-evolution of the atoms are calculated at 873 K (See computational methods for details). The  $^1\text{O}_2$  is included in the simulation because the Si-O network at the top surface of  $\text{SiO}_2/\text{Si}$  substrate facilitates the  $^3\text{O}_2 \rightarrow ^1\text{O}_2$  transition at temperature  $> 600$  K<sup>37-39</sup>, hence it can participate in the reaction. For AA'-BLG, stacking angle of  $\theta = 90^\circ$  was chosen. Identical atomic coordinates of O- and the C-atoms of the top-layer of BLG were set as the initial configurations of  $^1,3\text{O}_2 \dots \text{AB-BLG}$  and  $^1,3\text{O}_2 \dots \text{AA'-BLG}$  complexes (Figures 5.1.8b-d). Hence, the differences among the results solely stemmed from the stacking-order difference and spin state of  $\text{O}_2$ . Figures 5.1.7b-d display snapshots of initial ( $t = 0$  s) and final ( $t = 3$  ps) atomic configurations of  $\text{O}_2 \dots \text{BLG}$  complex.

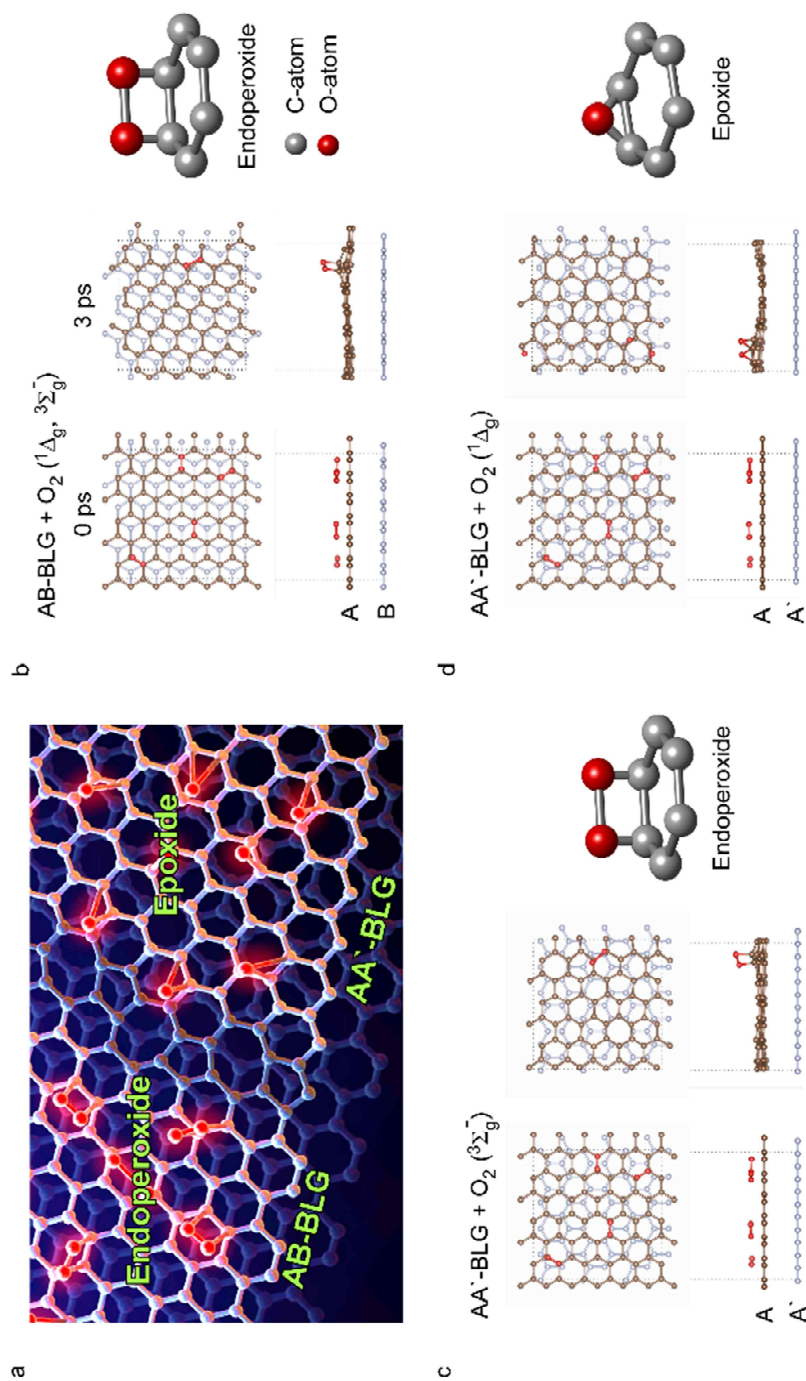


**Figure 5.1.8.** AIMD simulation revealing the different chemical reactivities of AB and AA'-BLG. **a.** A representative image of oxidized AB and AA'-BLG. **b.** AB-BLG reacting with singlet and triplet oxygen to form 4-membered endoperoxides **c.** AA'-BLG reacting with triplet oxygen to form endoperoxides. **d.** AA'-BLG reacting with singlet oxygen to form epoxides.

We find that  $^1\text{O}_2\text{...AB-BLG}$ ,  $^3\text{O}_2\text{...AB-BLG}$ , and  $^3\text{O}_2\text{...AA'-BLG}_2$  complexes exclusively lead to the formation of endoperoxides (see the image capture at  $t = 3$  ps of Figures 5.1.8b and c). The  $^1\text{O}_2\text{...AA'-BLG}$  complex, on the other hand, leads to the epoxides (3-membered ring structure, Figure 5.1.8d). For the latter complex, both the epoxides and endoperoxides are formed in the early stage ( $t = 0\sim 250$  fs) of the reaction, but most of the endoperoxides are decomposed in the later stage ( $t > 2$  ps);

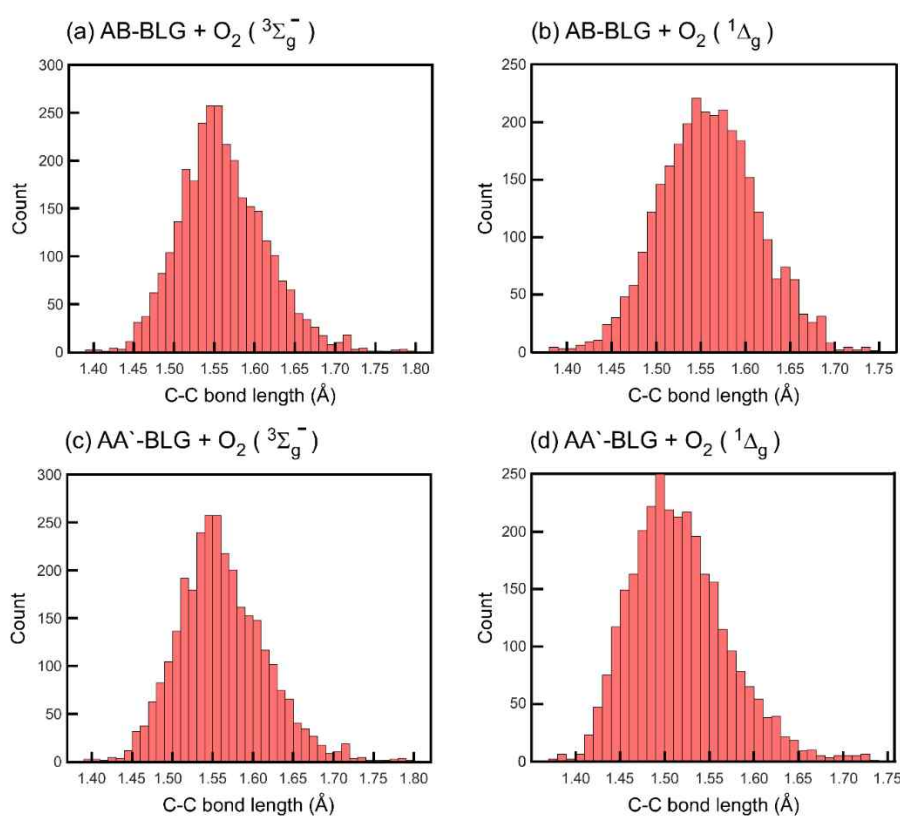


**Figure 5.1.9.** Analysis (AIMD simulation results) of C-C bond lengths of the different chemical bonding between AB and AA'-BLG resulting oxidation. The average C-C bond lengths of endoperoxide is 1.55 Å (a-c) and epoxides is 1.49 Å (d).

The analysis of the calculated C-C bond lengths (see Figure 5.1.9) in

endoperoxide (1.55 Å), in epoxides (1.49 Å) and in normal BLG (1.42 Å) further suggest that endoperoxides in BLG may have substantially larger mechanical strain than in the cases of epoxides in BLG. These results, when combined with the fact that heated SiO<sub>2</sub> surface causes <sup>3</sup>O<sub>2</sub> → <sup>1</sup>O<sub>2</sub> conversion, support our claim that AB and AA' BLG may have significantly different reactivity toward the O<sub>2</sub> and can lead to different oxide forms. The AIMD cannot directly simulate the changes in Raman spectra<sup>40</sup> or the IR-sSNOM contrasts, however.

### 5.1.4 Conclusion

Formation of stacking domains and their crystallographic characterization have been extensively studied thus far<sup>25,30,35</sup>. However, the stacking-dependent chemical reactivity of BLGs has not yet been explored. We have shown, based on the FTIR, IR-sSNOM and Raman spectroscopy measurements, that CVD-grown BLG allows reversible redox reaction with O<sub>2</sub> without inducing additional defects. The Raman spectral shapes of the oxidized BLG also indicate that different oxide structures are formed on the AB-BLG and the AA'-BLG. The simulation suggests that the singlet and triplet O<sub>2</sub> molecules behave differently on AA'- and AB-stacked BLGs, resulting in epoxides and endoperoxides, respectively. The CVD-grown bilayer graphene is useful for many applications. For example, it was reported that the bilayer graphene electrodes outperform monolayer graphene in hydrogen evolution reactions<sup>41</sup>, possibly because the electronic bands of the BLGs is better aligned with frontier molecular orbitals of chemisorbed hydrogen molecules than in the case of monolayer graphene. In this regard, we believe that the current study provides a new strategy to design high-performance graphene-based catalysts useful for various electrochemical, biological, and environmental applications.

## 5.1.5 References

- 1 Kim, S. J. *et al.* Characterization of chemical doping of graphene by in-situ Raman spectroscopy. *Appl. Phys. Lett.* **108**, 203111, doi:10.1063/1.4950969 (2016).
- 2 Bokdam, M., Khomyakov, P. A., Brocks, G., Zhong, Z. & Kelly, P. J. Electrostatic Doping of Graphene through Ultrathin Hexagonal Boron Nitride Films. *Nano Lett.* **11**, 4631-4635, doi:10.1021/nl202131q (2011).
- 3 Ohta, T., Bostwick, A., Seyller, T., Horn, K. & Rotenberg, E. Controlling the Electronic Structure of Bilayer Graphene. *Science* **313**, 951, doi:10.1126/science.1130681 (2006).
- 4 Castro, E. V. *et al.* Biased Bilayer Graphene: Semiconductor with a Gap Tunable by the Electric Field Effect. *Phys. Rev. Lett.* **99**, 216802, doi:10.1103/PhysRevLett.99.216802 (2007).
- 5 Yankowitz, M. *et al.* Tuning superconductivity in twisted bilayer graphene. *Science* **363**, 1059, doi:10.1126/science.aav1910 (2019).
- 6 Vaziri, S. *et al.* Bilayer insulator tunnel barriers for graphene-based vertical hot-electron transistors. *Nanoscale* **7**, 13096-13104, doi:10.1039/C5NR03002A (2015).
- 7 Cong, C., Yu, Ting. Evolution of Raman G and G' (2 D) modes in folded graphene layers. *Phys. Rev. B* **89**, 235430, doi:10.1103/PhysRevB.89.235430 (2014).
- 8 Wu, J.-B. *et al.* Interface Coupling in Twisted Multilayer Graphene by Resonant Raman Spectroscopy of Layer Breathing Modes. *ACS Nano* **9**, 7440-7449, doi:10.1021/acsnano.5b02502 (2015).
- 9 Justino, C. I. L., Gomes, A. R., Freitas, A. C., Duarte, A. C. & Rocha-Santos, T. A. P. Graphene based sensors and biosensors. *TrAC Trends in Analytical Chemistry* **91**, 53-66, doi:<https://doi.org/10.1016/j.trac.2017.04.003> (2017).
- 10 Cui, Y., Kundalwal, S. I. & Kumar, S. Gas barrier performance of graphene/polymer nanocomposites. *Carbon* **98**, 313-333, doi:<https://doi.org/10.1016/j.carbon.2015.11.018> (2016).
- 11 Allahbakhsh, A. in *Food Packaging* (ed Alexandru Mihai Grumezescu)

- 699-737 (Academic Press, 2017).
- 12 Tsang, A. C. H., Kwok, H. Y. H. & Leung, D. Y. C. The use of graphene based materials for fuel cell, photovoltaics, and supercapacitor electrode materials. *Solid State Sci.* **67**, A1-A14, doi:<https://doi.org/10.1016/j.solidstatesciences.2017.03.015> (2017).
  - 13 Cai, X., Lai, L., Shen, Z. & Lin, J. Graphene and graphene-based composites as Li-ion battery electrode materials and their application in full cells. *J. Mater. Chem. A* **5**, 15423-15446, doi:10.1039/C7TA04354F (2017).
  - 14 Li, R. *et al.* Surface Oxidation of Graphene Oxide Determines Membrane Damage, Lipid Peroxidation, and Cytotoxicity in Macrophages in a Pulmonary Toxicity Model. *ACS Nano* **12**, 1390-1402, doi:10.1021/acsnano.7b07737 (2018).
  - 15 Hossain, M. Z. *et al.* Aqueous-Phase Oxidation of Epitaxial Graphene on the Silicon Face of SiC(0001). *J. Phys. Chem. C* **118**, 1014-1020, doi:10.1021/jp4092738 (2014).
  - 16 Hossain, M. Z. *et al.* Chemically homogeneous and thermally reversible oxidation of epitaxial graphene. *Nat. Chem.* **4**, 305-309, doi:10.1038/nchem.1269 (2012).
  - 17 Liu, L. *et al.* Graphene Oxidation: Thickness-Dependent Etching and Strong Chemical Doping. *Nano Lett.* **8**, 1965-1970, doi:10.1021/nl0808684 (2008).
  - 18 Kim, D.-S. *et al.* Stacking Structures of Few-Layer Graphene Revealed by Phase-Sensitive Infrared Nanoscopy. *ACS Nano* **9**, 6765-6773, doi:10.1021/acsnano.5b02813 (2015).
  - 19 Jeong, G. *et al.* Mapping of Bernal and non-Bernal stacking domains in bilayer graphene using infrared nanoscopy. *Nanoscale* **9**, 4191, doi:DOI: 10.1039/c7nr00713b (2017).
  - 20 Vacque, V., Sombret, B., Huvenne, J. P., Legrand, P. & Suc, S. Characterisation of the O-O peroxide bond by vibrational spectroscopy. *Spectrochim. Acta A* **53**, 55-66, doi:[https://doi.org/10.1016/S1386-1425\(97\)83009-0](https://doi.org/10.1016/S1386-1425(97)83009-0) (1997).
  - 21 Wang, G. *et al.* Measuring Interlayer Shear Stress in Bilayer Graphene. *Physical Review Letters* **119**, 036101, doi:10.1103/PhysRevLett.119.036101 (2017).

- 22 Lu, C.-C. *et al.* Twisting Bilayer Graphene Superlattices. *ACS Nano* **7**, 2587-2594, doi:10.1021/nn3059828 (2013).
- 23 Wu, J.-B., Wang, H., Li, X.-L., Peng, H. & Tan, P.-H. Raman spectroscopic characterization of stacking configuration and interlayer coupling of twisted multilayer graphene grown by chemical vapor deposition. *Carbon* **110**, 225-231, doi:<https://doi.org/10.1016/j.carbon.2016.09.006> (2016).
- 24 Wu, J.-B. *et al.* Resonant Raman spectroscopy of twisted multilayer graphene. *Nat. Commun.* **5**, 5309, doi:10.1038/ncomms6309 <https://www.nature.com/articles/ncomms6309#supplementary-information> (2014).
- 25 Mohiuddin, T. M. G. *et al.* Uniaxial strain in graphene by Raman spectroscopy: G peak splitting, Grüneisen parameters, and sample orientation. *Phys. Rev. B* **79**, 205433, doi:10.1103/PhysRevB.79.205433 (2009).
- 26 Bruna, M. & Borini, S. Observation of Raman G-band splitting in top-doped few-layer graphene. *Phys. Rev. B* **81**, 125421, doi:10.1103/PhysRevB.81.125421 (2010).
- 27 Cong, C., Yu, T., Saito, R., Dresselhaus, G. F. & Dresselhaus, M. S. Second-Order Overtone and Combination Raman Modes of Graphene Layers in the Range of 1690–2150  $\text{cm}^{-1}$ . *ACS Nano* **5**, 1600-1605, doi:10.1021/nn200010m (2011).
- 28 Rao, R. *et al.* Effects of Layer Stacking on the Combination Raman Modes in Graphene. *ACS Nano* **5**, 1594-1599, doi:10.1021/nn1031017 (2011).
- 29 Zhang, W. *et al.* Molecular adsorption induces the transformation of *rhombohedral*- to Bernal-stacking order in trilayer graphene. *Nat. Commun.* **4**, 2074, doi:10.1038/ncomms3074 (2013).
- 30 Kajihara, K. *et al.* Diffusion and Reactions of Interstitial Oxygen Species in Amorphous SiO<sub>2</sub>. *J. Non. Cryst. Solids* **354**, 224-232, doi:10.1016/j.jnoncrysol.2007.07.038 (2008).
- 31 Dannefaer, S. Defects and Oxygen in Silicon Studied by Positrons. *physica status solidi (a)* **102**, 481-491, doi:10.1002/pssa.2211020203 (1987).
- 32 Dannefaer, S. & Kerr, D. Oxygen in silicon: A positron annihilation investigation. *J. Appl. Phys.* **60**, 1313-1321, doi:10.1063/1.337303 (1986).

- 33 Wang, L., Zhao, J., Sun, Y.-Y. & Zhang, S. B. Characteristics of Raman spectra for graphene oxide from ab initio simulations. *J. Chem. Phys.* **135**, 184503, doi:10.1063/1.3658859 (2011).
- 34 Sim, U. *et al.* Double-Layer Graphene Outperforming Monolayer as Catalyst on Silicon Photocathode for Hydrogen Production. *ACS Appl. Mater. Interfaces* **9**, 3570-3580, doi:10.1021/acsami.6b11750 (2017).
- 35 Hafner, J. Ab-initio simulations of materials using VASP: Density-functional theory and beyond. *J. Comput. Chem.* **29**, 2044-2078, doi:10.1002/jcc.21057 (2008).
- 36 Momma, K. & Izumi, F. VESTA 3 for three-dimensional visualization of crystal, volumetric and morphology data. *J. Appl. Crystallogr.* **44**, 1272-1276, doi:doi:10.1107/S0021889811038970 (2011).
- 37 Humphrey, W., Dalke, A. & Schulten, K. VMD: Visual molecular dynamics. *J. Mol. Graph.* **14**, 33-38, doi:[https://doi.org/10.1016/0263-7855\(96\)00018-5](https://doi.org/10.1016/0263-7855(96)00018-5) (1996).
- 38 Blöchl, P. E. Projector augmented-wave method. *Phys. Rev. B* **50**, 17953-17979, doi:10.1103/PhysRevB.50.17953 (1994).
- 39 Kresse, G. & Joubert, D. From ultrasoft pseudopotentials to the projector augmented-wave method. *Phys. Rev. B* **59**, 1758-1775, doi:10.1103/PhysRevB.59.1758 (1999).
- 40 Perdew, J. P., Burke, K. & Ernzerhof, M. Generalized Gradient Approximation Made Simple. *Phys. Rev. Lett.* **77**, 3865-3868, doi:10.1103/PhysRevLett.77.3865 (1996).
- 41 Grimme, S., Antony, J., Ehrlich, S. & Krieg, H. A consistent and accurate ab initio parametrization of density functional dispersion correction (DFT-D) for the 94 elements H-Pu. *J. Chem. Phys.* **132**, 154104, doi:10.1063/1.3382344 (2010).

## **6.1 Infrared Nano-spectroscopy Study on Oxidized Graphene Surface**

- This paper is currently being produced.

### **6.1.1 Introduction**

Many studies have been conducted for various physical and chemical properties of graphene. In particular, the change of electronic properties through the chemical and physical doping method is emerging as the most important research topic. The most commonly used graphene in accordance with this subject are mono- and bi-layer graphene. Interestingly in the case of BLG, it has been reported that superconducting phases can appear when two graphenes are engaged at a specific angle. In this respect, a non-Bernal stacking structure overlapped at a specific angle can be seen as having something unique properties. This distinctive characteristic stems from the different band structure. Also, there are fairly meaningful reports that charge transfer (CT) effect of graphene originates from unusual band structure. Among these CT effects, various interesting research results have been reported in the spectroscopy field. For example, giant IR absorption at the edge of the GO as a result of CT was reported. Also, it was reported that fluorescence can be affected by charge transfer effect at graphene. However, these researches are left much to be desired. First, there are fatal limitations to the aforementioned spectroscopic studies. Generally used optical equipment such as conventional FTIR cannot obtain spectroscopic information of individual domains of graphene on account of spatial resolution limitations. Second, most of the graphene related studies focus on monolayer graphene, not on bi or multilayer graphene. We think that interesting

research results can be drawn by studying the non-Bernal stacking structure of BLG.

We studied stacking dependent charge transfer effect at bilayer graphene using IR-sSNOM with CVD-grown BLG beyond diffraction limitation. As the most fundamental study, the CT effect of oxidized Bernal and non-Bernal BLG (AB-BLG and AA'-BLG) was examined. Interestingly, after oxidation, optical conductivity of AA'-BLG is increased more than 2 times. Additionally, intensity of certain vibration mode of a particular functional group ( $1325\text{ cm}^{-1}$ ) is enhanced nearly sextuple. We attribute these unusual spectroscopic phenomena to graphene CT effect. We believe that the abundant free electrons present in graphene have such an effect.

### 6.1.2 Experiment

**Sample measurements (FTIR, Raman & topography)** - Micro-Raman spectroscopy measurements (an excitation wavelength of 514.5 nm) are carried out on the BLG sample to determine the stacking structure of BLG and to confirm oxidation. We utilize side-illuminated IR-sSNOM (home-built) equipped with an infrared laser (an infrared HeNe laser at  $\lambda = 3.39 \mu\text{m}$  and a quantum cascade laser at  $\lambda = 7.46 \sim 8 \mu\text{m}$ ), and liquid-nitrogen cooled InSb detectors and a mercury cadmium telluride (MCT) detector. The IR-sSNOM probe (Nanosensors, PPP-NCHPt,  $\Omega \sim 300 \text{ kHz}$ ) vertically vibrates with an amplitude of  $20 \sim 100 \text{ nm}$ . A linearly polarized IR-light (parallel to the tip) is focused on the tip-sample junction with an angle of  $30^\circ$  via a Schwarzschild objective lens. The collected scattered light from the junction light is homodyne-amplified at Michelson interferometer and filtered unwanted background signal by lock-in amplifier to obtain the 2<sup>nd</sup> harmonic ( $2\Omega \sim 600 \text{ kHz}$ ) intensity ( $|s_2|^2$ ) and phase ( $\phi_2$ ) IR-sSNOM signals. The IR-sSNOM data shown in main text normalize to the SiO<sub>2</sub> intensity and phase signals. FTIR measurements were carried out on the graphene sample with Perkin Elmer Spotlight 400.

**Sample preparation (CVD bilayer graphene)** - Graphene films were synthesized on  $25 \mu\text{m}$  thick copper foil through the CVD method using methane (50 s.c.c.m.) and hydrogen (5 s.c.c.m.) gas with vacuum pumping ( $\sim 1.5 \text{ mtorr}$ ) at  $1000 \text{ }^\circ\text{C}$  for  $\sim 2$  hours. Methane was used only during the growth stages of graphene and was not used during the cooling process. Poly (methyl methacrylate) (PMMA) was spin-coated on top of graphene, and the copper foil was etched in an ammonium persulfate

solution (20 mM with distilled water). The achieved monolayer graphene films were transferred onto SiO<sub>2</sub> (thickness of 285 nm) / Si substrates. The monolayer covers nearly all areas of the SiO<sub>2</sub>/ Si substrate, and bilayer domains appear as islands with an average radius of  $\sim 10 \mu\text{m}$ .

**Oxidation processes of CVD bilayer graphene** - Graphene films were oxidized under atmospheric pressure, with 100 ml / min of oxygen and 300 ml/min of argon gas flow, in a 1-inch quartz tube vacuum furnace. When the temperature of the furnace reached 773 K, the furnace was slid to cover the sample to heat the sample for 30 min. After the reaction, the sample was rapidly cooled by sliding the furnace away.

### 6.1.3 Results and Discussion

#### Changes in the IR-sSNOM contrasts of BLG upon O<sub>2</sub> exposure

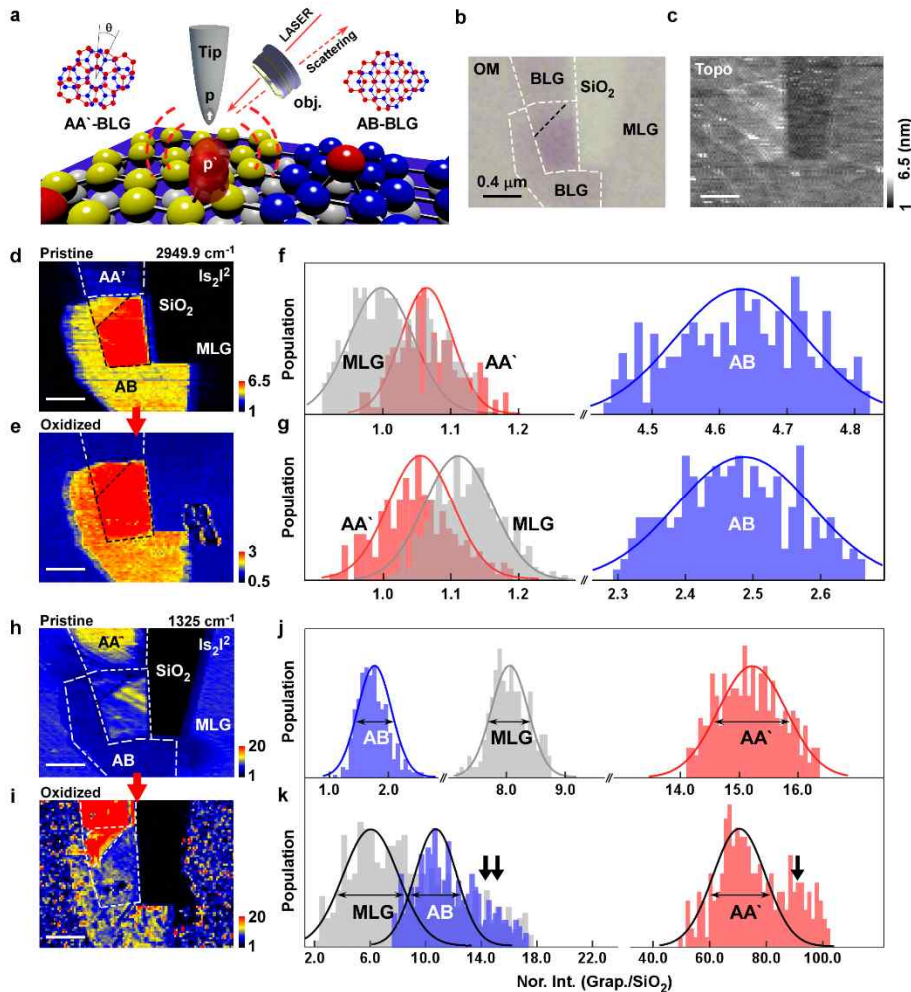


**Figure 6.1.1. Changes in the IR-sSNOM contrasts of BLG and MLG upon O<sub>2</sub> exposure.**  
**a**, Schematic image of infrared-scattering-type scanning near-field optical microscopy (IR-sSNOM) measurement. The  $p$  and  $p'$  represent the tip-dipole and tip image-dipole on bilayer graphene (BLG) sample surface, respectively. The scattering amplitude of IR-sSNOM is affected by optical conductivity of graphene ( $\sigma$ ). **b**, Optical reflectance microscopy (OM) image of BLG samples grown on top of monolayer graphene and made by overlapping monolayer. **c**, AFM image of **b**. **d & e**, IR-sSNOM intensity images of the pristine BLG sample obtained with IR laser at  $\tilde{\nu} = 2949.9 \text{ cm}^{-1}$  pristine (**d**) and after reaction (**e**). **f & g**, Histograms of the IR-sSNOM intensity (at  $\tilde{\nu} = 2949.9 \text{ cm}^{-1}$ ) of AA' (red), AB (blue) and MLG (gray) before pristine (upper panel) and after oxidized (lower panel). **h & i**, IR-sSNOM intensity images of the pristine BLG sample obtained with IR laser at  $\tilde{\nu} = 1325 \text{ cm}^{-1}$  before pristine (**h**) and after oxidized (**i**). **j & k**, Histograms of the IR-sSNOM intensity of AA' (red), AB (blue) and MLG (gray) before pristine (upper panel) and after oxidized (lower panel)

at  $\tilde{\nu} = 1325 \text{ cm}^{-1}$ . The color scale of IR-sSNOM intensity image is normalized to the IR-sSNOM intensity of  $\text{SiO}_2$  from each image. Also, curves shown in images (f, g, j and k) are the Gaussian fits. All scale bars in AFM topography and IR-sSNOM images correspond to  $0.4 \mu\text{m}$ .

As shown in Figure 6.1.1a, we excite an oscillating dipole (p) at the tip-end with light. This tip-dipole interacts with its own image (p') via dipole-dipole coupling<sup>1</sup>. The amplitude of image-dipole is affected by the local optical properties (such as the local conductivity of graphene,  $\sigma$ , and dielectric constants of substrate wafer (in this case  $\text{SiO}_2$  and Si). The scattering amplitude at the tip-sample junction (the IR-sSNOM amplitude) correlates with local optical conductivities of the sample. For this reason, the IR-sSNOM images not only display the local stacking structures of BLG but also distinguish between AB-BLG and AA'-BLG. As is well known, far-field white-light reflection microscopy (OM) and atomic force microscopy (AFM) only reveal the number of layers of graphene (Figures 6.1.1b and c). However, looking at Figure 1d, AB-BLG and AA'-BLG can be distinguished through the IR-sSNOM imaging at  $\tilde{\nu} = 2949.9 \text{ cm}^{-1}$  ( $\omega = 0.366 \text{ eV}$ ). Owing to the parabolic dispersion of band structures<sup>2</sup>, the inter-band transition of pristine AB-BLG (0.37 eV) is resonant with the frequency of the IR-laser whereas AA-BLG or AA'-BLG do not show such resonances. The pristine AB-BLG shows large contrast in IR intensity compared with those of pristine MLG or pristine AA'-BLG. Contrast was large in order of AB-BLG > AA'-BLG > MLG >  $\text{SiO}_2$ . However, after reaction, the optical conductivities of graphene are changed. In this case, contrast was large in order of AB-BLG > MLG > AA'-BLG >  $\text{SiO}_2$  (Figure 6.1.1e). sequences of MLG and AA'-BLG have been changed. Also, intensity of AB-BLG was decreased by oxidation. In the histogram Figures 6.1.1f and g, except the such an intensity change, the variation of the deviation is hardly changed.

However, looking at the IR-sSNOM imaging in the intra-band transition region at  $\tilde{\nu} = 1325 \text{ cm}^{-1}$  (Figure 6.1.1h), the contrast order of pristine graphene is different from that of the inter-band transition region. Contrast was large in order of AA'-BLG > MLG > AB-BLG > SiO<sub>2</sub>. The difference of intensity in intensity is also stemmed from the difference in band structures. Looking at the band diagrams of AB and AA'-BLG<sup>2</sup>, AA'-BLG has two accessible conduction channels. On the contrary, the pristine AB-BLG has one conduction channel around  $E_f$ <sup>2</sup>. This difference in the number of channels shows a huge difference in conductivity. However, when graphene is oxidized, the tendency of intensity is greatly changed. The intensity of oxidized AB-BLG was much stronger than that of oxidized MLG, resulting in a change in the order of contrast (AA'-BLG > AB-BLG > MLG > SiO<sub>2</sub>). In addition, the intensity of oxidized MLG dropped sharply, and the intensity of oxidized AB-BLG and oxidized AA'-BLG drastically increased.

Apart from change in the order of intensity, there is something we need to focus on. Looking at the inter-band transition region IR-sSNOM image (Figure 6.1.1i), high intensity spots are distributed throughout the all graphene but no spots were seen on SiO<sub>2</sub>. Comparing the topography image of before and after oxidation, there was no significant change. Looking at the histogram (Figures 6.1.1 j and k), distribution of intensity is broadened for all three types of graphene. The Gaussian fit curve was seen to be widened after oxidation. Furthermore, this histogram can be divided into two elements: one is a histogram with a general distribution and the other is a tail with a relatively high intensity (black arrows in Figures 6.1.1j and k). And then, it will be necessary to check whether this phenomenon of dividing into two elements occurs in all intra band transition areas except for inter-band transitions. In other words, it must be distinguished whether the high intensity component is

caused by other influences.

### Wavenumber dependent of intensity changes upon O<sub>2</sub> exposure

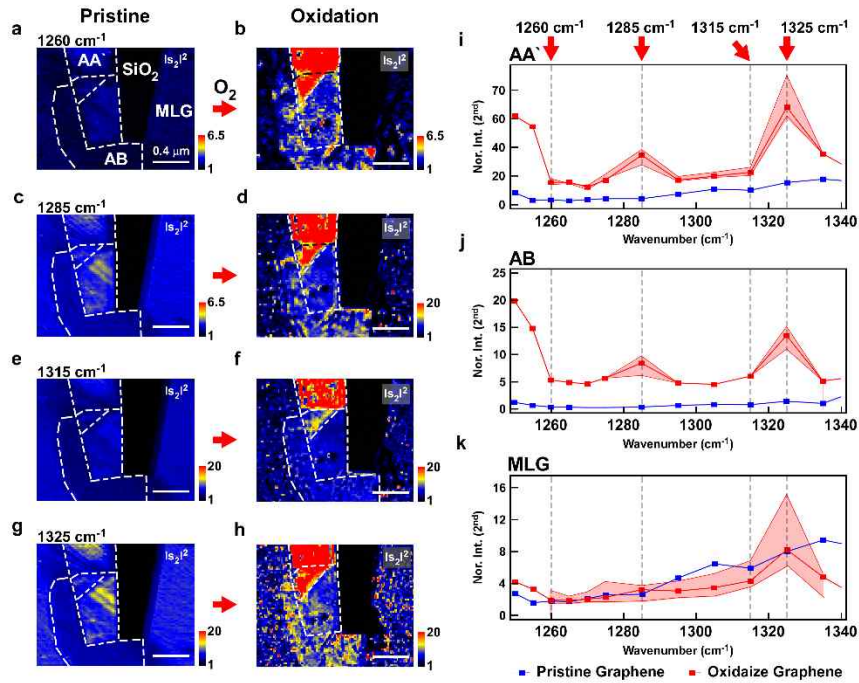


**Figure 6.1.2. The IR-sSNOM contrasts Changes of BLG and MLG upon O<sub>2</sub> exposure.** **a-h**, IR-sSNOM intensity images of the pristine BLG sample obtained with IR laser (at  $\tilde{\nu} = 1260, 1285, 1315$  and  $1325 \text{ cm}^{-1}$ ) pristine (**a, c, e** and **g**) and after oxidized (**b, d, f** and **h**) graphene. All scale bars in IR-sSNOM images correspond to  $4 \mu\text{m}$ . **i, j** and **k**, Nano IR-sSNOM spectra ( $\tilde{\nu} = 1250 \sim 1340 \text{ cm}^{-1}$ ) of AA'-BLG (**i**), AB-BLG (**j**) and MLG (**k**) pristine (blue) and oxidized (red). The red area means the area of the average of the two components in the histogram, and the square points (red and blue) mean the average value of IR-sSNOM intensity.

We conduct IR-sSNOM imaging in the intra-band transition region (at  $\tilde{\nu} = 1250 \sim 1340 \text{ cm}^{-1}$ ) to confirm that this is happening at different wavenumber. When looking at the pristine graphene IR-sSNOM image (Figures 6.1.2a, c, e and g) in the intra-band transition region (at  $\lambda = 1260, 1285, 1315$  and  $1325 \text{ cm}^{-1}$ ), there was no particular change. However, when the oxidation reaction occurs, unusually high intensity spots are visible (Figures 6.1.2b, d, f and h). In addition, the intensity of spots varies with wavelength and stacking structure. In the case of MLG, spots were

visible at all wavenumber, but in the case of AB-BLG, spots were visible only at a specific wavelength. On the other hand, AA-BLG showed spots with very strong intensity at a specific wavenumber. The intensity of the spots of oxidized AA-BLG is larger than those of oxidized AB-BLG and MLG.

We obtained the Nano IR-sSNOM spectra of AA'-BLG , AB-BLG and MLG (Figures 2i, j and k) from  $\tilde{\nu} = 1250$  to  $\tilde{\nu} = 1340$   $\text{cm}^{-1}$ . The Nano IR-sSNOM Spectra were obtained by taking the maximum and minimum average values from the two histograms in each IR-sSNOM images. The square points in each histogram (red and blue) are average value of IR-sSNOM intensity. First of all, looking at the Nano IR spectrum of AA'-BLG, the conductivity increased more than twice after oxidation. In addition, the average intensity increased more than 6 times at a specific wavenumber ( $\tilde{\nu} = 1325$   $\text{cm}^{-1}$ ). After the reaction, the optical conductivity of the AB-BLG nano IR-sSNOM spectrum also increased. However, IR enhancement was weak at a specific wavenumber ( $\tilde{\nu} = 1325$   $\text{cm}^{-1}$ ). In the case of MLG, unlike BLG, there was no change in optical conductivity. However, it showed relatively strong enhancement at  $\tilde{\nu} = 1325$   $\text{cm}^{-1}$ .

We have found what we see in common feature at these three nano IR-sSNOM spectra. Two new peaks occur at a specific wavenumber (at  $\tilde{\nu} = 1285$  and  $1325$   $\text{cm}^{-1}$ ). In particular, the peak intensity was different depending on the type of graphene, and AA-BLG showed the strongly enhanced intensity. In addition, it could be seen that only AB and AA'-BLG had a peak at  $1250$   $\text{cm}^{-1}$ .

#### **6.1.4 Conclusion**

In this experiment, we show a strong IR enhancement phenomenon of graphene. In particular, a strong IR enhancement phenomenon occurred in non-Bernal stacking structure graphene. We think that the reason why such a peculiar phenomenon occurs is due to the graphene possessed by the abundant free electrons. Furthermore, the influence of the unique band structure of only the non-Bernal stacking structure is large. We believe that our results (graphene CT effect) can be applied to designing a new strategy for high-performance graphene-based catalysts, which can be used in electrochemical, biological, and environment.

### 6.1.5 References

- 1 Kim, S. J. *et al.* Characterization of chemical doping of graphene by in-situ Raman spectroscopy. *Appl. Phys. Lett.* **108**, 203111, doi:10.1063/1.4950969 (2016).
- 2 Jeong, G. *et al.* Mapping of Bernal and non-Bernal stacking domains in bilayer graphene using infrared nanoscopy. *Nanoscale* **9**, 4191, doi:DOI: 10.1039/c7nr00713b (2017)

## 7.1 Reversible Multilayer CO<sub>2</sub> Loading in Bilayer Graphene

- This paper will be submitted

### 7.1.1 Introduction

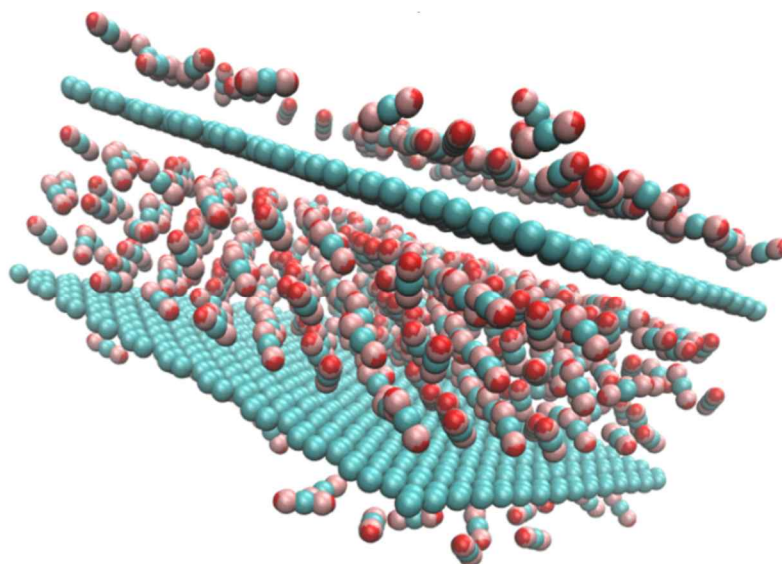


**Figure 7.1.1 Schematic illustration of intercalated CO<sub>2</sub> molecules between two graphenes.** MD simulation results of intercalated CO<sub>2</sub> molecules between two graphenes

Besides many unique properties relevant to micro-electronics<sup>1,2</sup>, chemical sensors<sup>3</sup>, optics<sup>4</sup>, and catalysis<sup>5,6</sup>, graphene shows unique property of capturing molecules and ions (such as H<sub>2</sub><sup>7</sup>, CO<sub>2</sub><sup>8,9</sup>, ammonia<sup>10</sup>, nitrogen dioxide<sup>11</sup>, sulfur dioxide<sup>12</sup>, water<sup>13,14</sup>, sodium<sup>15</sup>, sulfur<sup>16</sup> and Lithium<sup>17</sup>) between the layers and between the graphene -substrate<sup>18</sup>. The van der Waals pressure applied in the graphene pocket is reported to be ~1 GPa<sup>19</sup>. This capturing capability can be also utilized as nano-reactors for chemical reactions<sup>20,21</sup>. Particularly, multilayers of graphene oxides<sup>9,22</sup> can capture ~ 4 mmol per grams of graphene, which may be

useful for the sequestration of environmental CO<sub>2</sub>. The capture includes the capturing of gas-phase CO<sub>2</sub> in the pocket defined by the graphene and graphite surfaces, the adsorption onto the graphene surface, and the intercalation of CO<sub>2</sub> into the gap of graphene layers. In analogy to CO<sub>2</sub> capturing by rocks<sup>23-25</sup> and other materials<sup>26</sup>, it has been interpreted that the capturing or intercalation of CO<sub>2</sub> occurs via the adsorption at the defect sites or functional groups<sup>3</sup>, creating mono- or sub-molecular layer of CO<sub>2</sub> on graphene<sup>9,27</sup>. Because the results are largely based on the isotherm measurements on graphite powder of graphite and graphite oxide<sup>9,28</sup>, the structure of the captured CO<sub>2</sub> and the driving force are largely unverified, although there exists a theory suggesting that CO<sub>2</sub> adsorbs on graphene via the charge-transfer as well as via the van der Waals interaction<sup>29</sup>.

Here we report an experimental evidence that CO<sub>2</sub> is loaded in between the layers of graphene as a form of multilayer condensate, not as a monolayer adsorbate. When exposed to CO<sub>2</sub>(g) at  $T \sim 770$  K, topographic thickness of bilayer and trilayer graphene is found to be increased to  $\sim 3$  nm, which is 5 times thicker than what is expected from the adsorption of CO<sub>2</sub> on either surface of graphene. Furthermore, most of the captured CO<sub>2</sub> could be reversibly unloaded by heating under inert gas. The molecular dynamics (MD) simulation further indicates that the captured CO<sub>2</sub> has crystal-like clusters of CO<sub>2</sub> formed under the internal pressure of graphene.

### 7.1.2 Experiment

**The sample and CO<sub>2</sub> loading** - The sample is formed on SiO<sub>2</sub> (285 nm) / Si wafer and is consisted of a uniform monolayer graphene (MLG) and additional graphene layer island (diameters of ~10 μm) forming BLG islands with various stacking degree. The sample was located in a furnace at 773 K and exposed to the constant flow of CO<sub>2</sub> (g) flow at 100 ml / min or H<sub>2</sub> (g) at 150 ml / min. For the SERS measurement, Au-nanoparticles (NPs, diameters of 80 nm) were dispersed on BLG / MLG sample on a Cu-film. Such Au-NP-BLG-Cu metallic junctions serve as electromagnetic hotspots for the SERS measurement.

**Sample measurements (FTIR, Raman & topography)** - FTIR measurements were carried out on the TLG and MLG sample with Perkin Elmer Spotlight 400. Micro-Raman spectroscopy measurements (an excitation wavelength of 514.5 nm) are carried out on the sample to determine graphene layer stacking. The SERS spectra were obtained by placing the laser focus onto AuNP-BLG-Cu junctions. The AFM (home-built), operating under the tapping-mode condition, was carried out with silicon probes (Nanosensors, PPP-NCHR,  $\Omega \sim 300$  kHz)

### 7.1.3 Results and Discussion

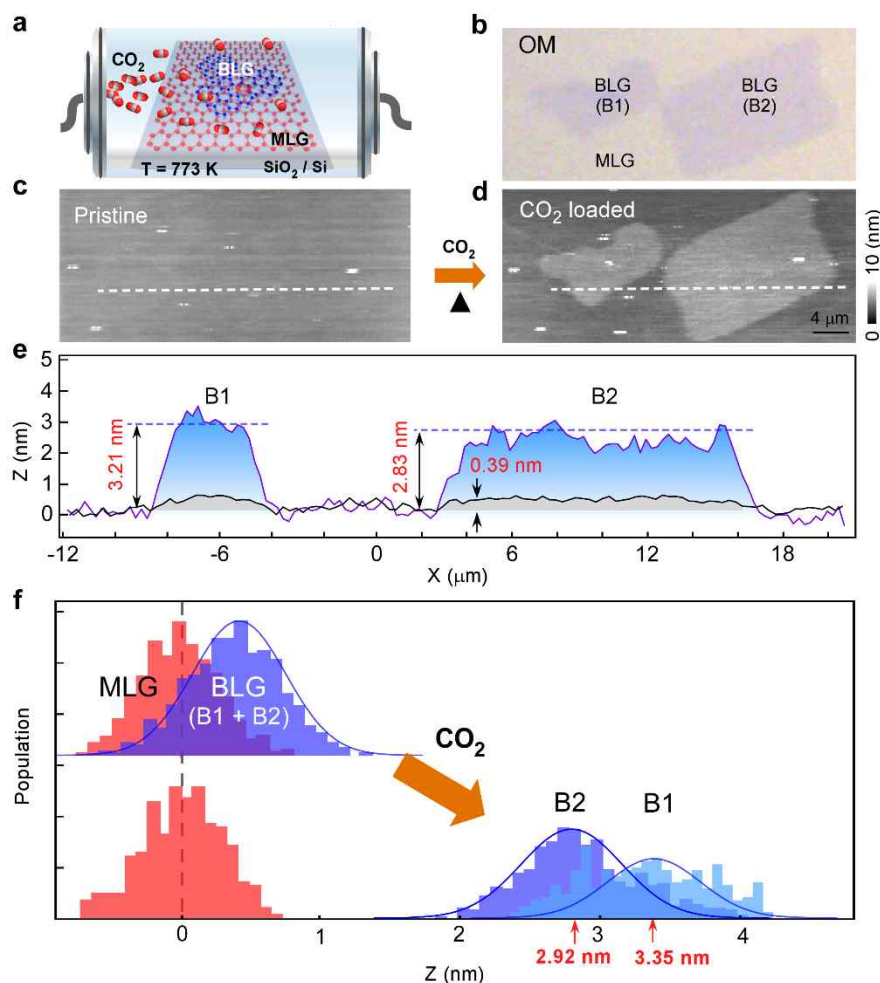


**Figure 7.1.2. Topographic height changes in CVD-BLG upon CO<sub>2</sub>-exposure.** **a**, Schematic of the CO<sub>2</sub>-loading into graphene. **b**, Optical reflectance microscopy (OM) image showing two BLG islands (B1 & B2) grown on top of monolayer graphene (MLG). **c** & **d**, AFM images of the sample before (**c**) and after (**d**) the CO<sub>2</sub>-exposure. The height color scale of the two images are the same. The scale bar in (**d**) represents 4 μm. **e**, Topographic line-profiles (black = pristine; blue = CO<sub>2</sub>-exposed) of B1 and B2 sampled from **c** & **d** (dashed lines). **f**, Histograms of the topographic height of BLG (blue) and MLG (red) before (upper panel) and after (lower panel) the CO<sub>2</sub>-exposure. The zero of height (grey dashed line) refers to the mean topographic height of MLG. Also shown in curves are the Gaussian fits. Average heights (in reference to MLG) of B1 and B2 are also shown.

The sample employed is BLG on SiO<sub>2</sub> (thickness of 285 nm) / Si substrate grown by chemical vapor deposition (CVD) on Cu-foil followed by the substrate-transfer. The sample has BLG islands grown on top of a uniform monolayer of

graphene (MLG). For the loading of CO<sub>2</sub> (see Figure 7.1.2a), the sample is placed in the furnace maintained at the temperature of  $T = 770$  K, and CO<sub>2</sub> gas was flowed at a rate of 100 ml / min. After the CO<sub>2</sub>-loading, the sample was rapidly cooled down to room temperature in the presence of CO<sub>2</sub> in the furnace.

The atomic force microscopy (AFM, operating under tapping-mode) images are obtained for the same set of BLG islands before (Figure 7.1.2c) and after (Figure 7.1.2d) the CO<sub>2</sub>-exposure. The topography ( $z$ ) scale of AFM was calibrated against calibration grating and mechanically exfoliated few-layer graphene. The AFM image measured before the CO<sub>2</sub>-exposure (pristine, Figures 7.1.2c and e) shows average topographic height of BLG (B1 and B2) of  $\sim 0.39$  nm in reference to the underlying MLG, which is a typical topographic thickness of a single layer graphene<sup>30,31</sup>. Upon CO<sub>2</sub>-exposure (Figures 7.1.2d and e), the BLG islands show clear height increase, indicating the loading of CO<sub>2</sub> preferentially to BLG.

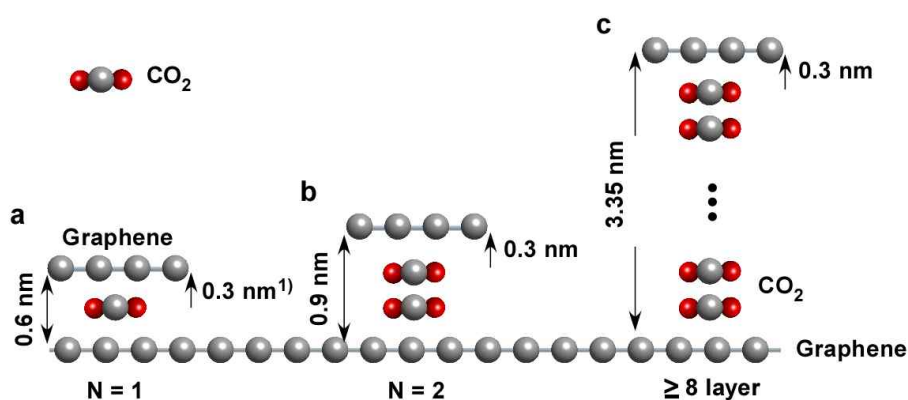


**Figure 7.1.3.** a, b & c, Illustration of estimated minimum height of intercalated bilayer graphene (BLG). a & b, Estimation of minimum BLG height in case of (a) CO<sub>2</sub> monolayer intercalating and (b) CO<sub>2</sub> bilayer intercalating. c, Estimation of number of CO<sub>2</sub> layers in B2 BLG (Figure 6.1.2f).

Quite remarkably, the thickness of CO<sub>2</sub>-loaded BLG is much larger than

what is expected from two graphene layers and a monolayer of CO<sub>2</sub>. Rather, the thickness corresponds to  $\geq 8$  layers of CO<sub>2</sub> sandwiched between the two graphene layers (see Supporting Information-figure 7.1.3). Figure 7.1.2f show the histograms of topographic height sampled from the AFM images before and after the CO<sub>2</sub>-loading, better showing the thickness changes beyond the roughness of the substrate (width of the peaks of the histograms). The CO<sub>2</sub>-loaded B1 and B2 islands, which initially had nearly the same height of 0.4 nm, exhibit  $\sim 0.4$  nm height difference, which may indicate the stacking-structure specific CO<sub>2</sub>-loading (see below for more data). The roughness in CO<sub>2</sub>-loaded BLG island (i. e., the width in the histogram) is nearly the same (to within a few percent) as those of the MLG and pristine BLG, showing that CO<sub>2</sub>-loading conformally increases the thickness of BLG.

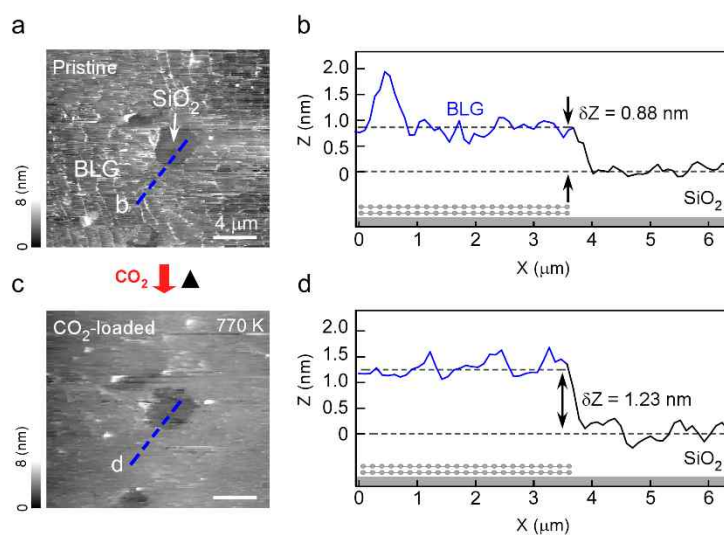


**Figure 7.1.4.** **a**, Contact-mode AFM image of CVD-grown multilayer graphene. **b**, Line-profiles sampled from **a** (dashed lines in **b**). **c**, Clearly visualized BLG at the same position with **a** after CO<sub>2</sub>-loading due to volume expansion. **d**, Line-profiles sampled from **c** (dashed lines in **d**). By CO<sub>2</sub>-exposure, the thickness of BLG (measured from the top surface of SiO<sub>2</sub> as standard) is increased. All scale bars in AFM images are 4 μm.

We have carried out the similar measurement with contact-mode AFM,

which leads to the essentially the same result (see Figure 7.1.4). This rules out the possibility that the topographic changes may arise from chemical-specific tip-sample interaction<sup>32,33</sup>, not from genuine topographic height change.

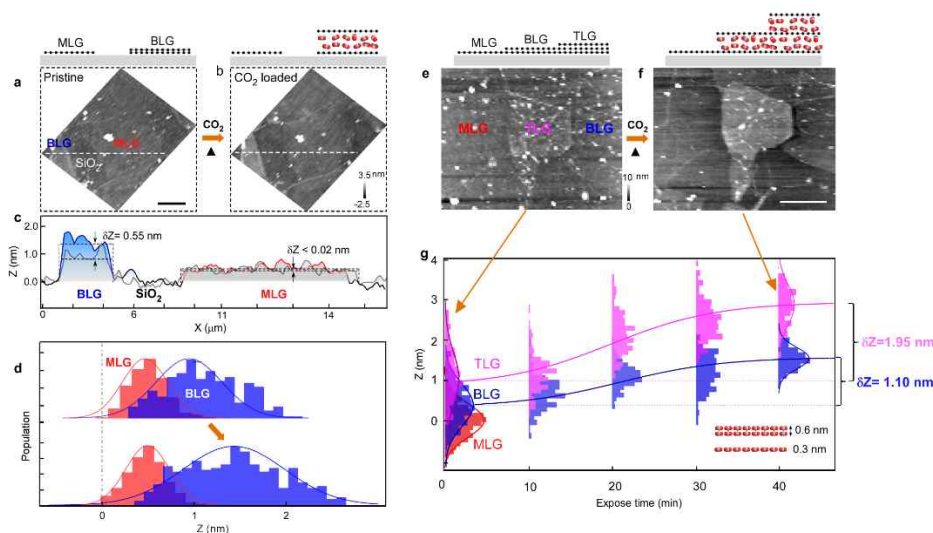


**Figure 7.1.5. Thickness changes in MLG, BLG and TLG upon CO<sub>2</sub>-exposure.** **a & b**, AFM images containing MLG, BLG, and SiO<sub>2</sub> regions, obtained before (**a**) and after (**b**) the CO<sub>2</sub>-exposure. **c**, line-profiles sampled from **a & b** (dashed lines in **a & b**). The  $\delta Z$  refers to the change in height of MLG and BLG upon CO<sub>2</sub>-exposure, as measured from the surface of SiO<sub>2</sub> substrate. **d**, Associated topographic histograms of MLG (red) and BLG (blue). In **c** and **d**,  $Z = 0$  nm refers to the height to the surface of SiO<sub>2</sub>. **e & f**, AFM images containing MLG, BLG, TLG regions, obtained before (**e**) and after (**f**) the CO<sub>2</sub>-exposure (for 40 min). **g**, Time-evolution of the height histograms of BLG (blue) and TLG (magenta) shown in **e & f**. The histogram of MLG (red), which serves as  $Z = 0$  nm reference, is also shown.  $\delta Z$  for BLG and TLG indicate the thickness increase during the 40 mins of CO<sub>2</sub>-exposure. All scale bars in AFM topography images correspond to 4  $\mu$ m.

We find that such thickness change does not occur for MLG on SiO<sub>2</sub> / Si. Figures 7.1.5a and b show the AFM images of a part of sample containing the regions of MLG, BLG, and SiO<sub>2</sub> / Si, obtained before and after the CO<sub>2</sub>-loading. Here, the bare SiO<sub>2</sub> region serves as the topographic reference ( $Z = 0$  nm). As can be seen in the line-profiles (Figure 7.1.5c) and the histograms (Figure 7.1.5d), the thickness of BLG (as measured from top surface of SiO<sub>2</sub>) is increased by  $\delta Z > 0.5$  nm, thickness

of the MLG is essentially unchanged ( $\delta Z < 0.011$  nm). Figure 7.1.3e and f show the AFM images of a part of sample containing the regions of BLG and trilayer graphene (TLG), obtained before and after the CO<sub>2</sub>-loading (40 min). Figure 7.1.5g show the time-evolution of the thickness of BLG and TLG during the 40 minutes of CO<sub>2</sub>-exposure.

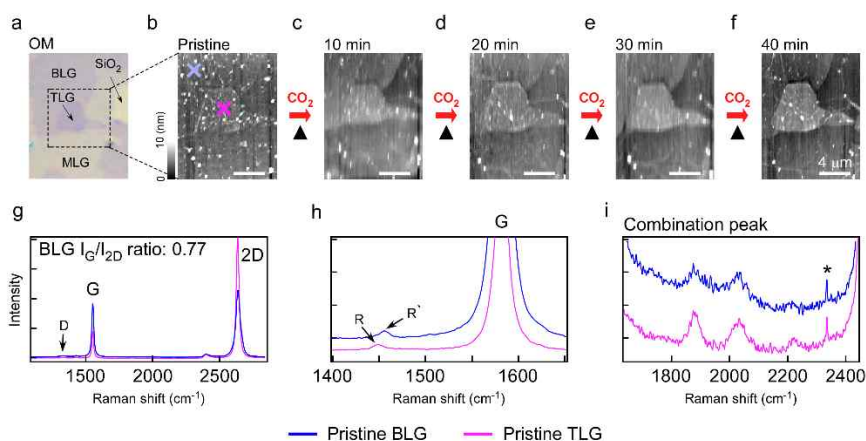


**Figure 7.1.6.** **a**, Optical reflectance microscopy (OM) image of CVD-grown multilayer graphene. **b**, AFM image of BLG and TLG grown on the top of MLG. Raman spectra of BLG (blue) and TLG (magenta) were measured at position X. **b-f**, Time-evolution of the AFM images. The scale bars in 3. b-f represent 4  $\mu\text{m}$  length scale. **g**, Wide range Raman spectra of pristine BLG and TLG. **h**, G, R and R' (rotation)-peaks of magnified Raman spectra of BLG and TLG. From the R and R' peaks, it is considered that the synthesized CVD-grown graphene is not Bernal stacking structure form.<sup>2,3</sup> Through  $I_G/I_{2D}$  ratio observed from BLG and TLG, we estimate that both BLG and TLG are non-Bernal or rhombohedral stacking structure.<sup>4-6</sup> **i**, Combination-mode peaks of Raman spectra of BLG and TLG. The peak at 2331  $\text{cm}^{-1}$  (marked as \* in **i**) is assigned to symmetric mode of the ambient N<sub>2</sub> gas. All scale bars in AFM images are 4  $\mu\text{m}$ .

time-evolution of the AFM images and Raman spectra of BLG and TLG are shown in Figure 7.1.6. We find that the thickness change ( $\delta Z$ ) for TLG is approximately twice that of BLG. This, together with the BLG / MLG comparison shown in Figures 7.1.5a-d, proves that the loaded CO<sub>2</sub> intercalates *between* the graphene layers, not between the graphene and substrate, or adsorbs on top surface of graphene.

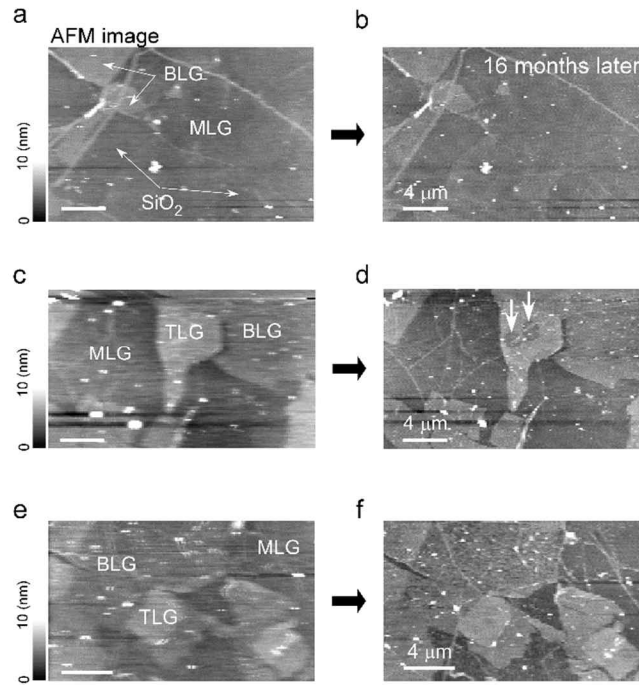


**Figure 7.1.7.** **a, c, and e,** AFM images of various volume-expanded BLG and TLG samples after CO<sub>2</sub>-loading. **b, d, and f,** AFM images of stably retained CO<sub>2</sub> in the graphene even after 16 months kept at room temperature and atmospheric pressure, despite some damaged island TLGs observed in **d**. All scale bars are 4 μm.

Once loaded, the thickness of the CO<sub>2</sub>-loaded BLG and TLG is maintained for > 16 months at room temperature (see Figure 7.1.7). Upon heating at  $T = 770$  K under atmospheric or H<sub>2</sub> environment, most of the captured CO<sub>2</sub> are unloaded from the graphene.



**Figure 7.1.8. Unloading of CO<sub>2</sub>, temperature dependence of CO<sub>2</sub>-loading, and spectroscopy of CO<sub>2</sub>-loaded BLG.** **a & b**, AFM images of CO<sub>2</sub>-loaded BLG before and after the heating (T = 770 K) under atmosphere. **c & d**, Associated changes in line-profiles (**c**) and height histogram (**d**), showing the reduction in thickness upon heating. **e**, Thickness change (AFM images and height histograms) in two BLG islands (B3 and B4) upon alternating CO<sub>2</sub> and H<sub>2</sub> exposure, showing near-reversible CO<sub>2</sub>-loading and unloading. **f & g**, Changes in Raman G and D peaks measured from the B3 and MLG shown in the inset AFM image (marked as x) of **e**, upon alternating CO<sub>2</sub> and H<sub>2</sub> exposure. **h**, The surface-enhanced Raman scattering (SERS) spectra measured from AuNP-BLG-Cu junction structure (see inset figure) before and after the CO<sub>2</sub>-loading. Red arrows point to newly emerging peaks, which are assigned to the stretching vibrational modes of the intercalated CO<sub>2</sub>. Black and grey arrows point to the reported<sup>75, 76</sup> spectral positions and relative intensities (lengths of the arrows) of the vibrational peaks of solid CO<sub>2</sub> deposited on Cu at T = 40K. **i**, Temperature-dependence of CO<sub>2</sub>-loading of BLG (blue) and TLG (magenta). Error bars correspond to standard deviation of height of TLG and BLG islands. **j**, Change in the infrared spectra (IR) reflection spectra of TLG upon alternating CO<sub>2</sub> and H<sub>2</sub> exposure. The scale bars in **a**, **b**, and **e** represents 4 μm length scale.

Figures 7.1.8a-d shows one such example. In fact, we could carry out multiple cycles of loading and unloading of CO<sub>2</sub> without the apparent damage to the sample (see Figure 7.1.8e). Similar unloading can be introduced by the prolonged laser illumination of the sample. We find that the thermal annealing for a limited time (< 10 min) does not completely recovers the original thickness of the graphene: as can be seen in Figures 7.1.2c and d, the annealed BLG show a height of 0.6 nm, which is thicker than that of pristine BLG by 0.2~0.3 nm. This thickness difference, which is close to a single-atom thickness, suggests the existence of strongly bound monolayer CO<sub>2</sub> as well as the weakly bound CO<sub>2</sub>.

We find that the amount (or the rates) of CO<sub>2</sub> - loading / unloading on graphene islands with the same number of layers show notable island-to-island variation. As shown in Figure 7.1.8e, two BLG islands (B3 and B4 in inset topography) with the same initial thicknesses, after undergoing a loading / unloading cycle (each with 10 min CO<sub>2</sub> and H<sub>2</sub> exposure), exhibit notable thickness differences ( $\delta Z > 0.6$  nm)

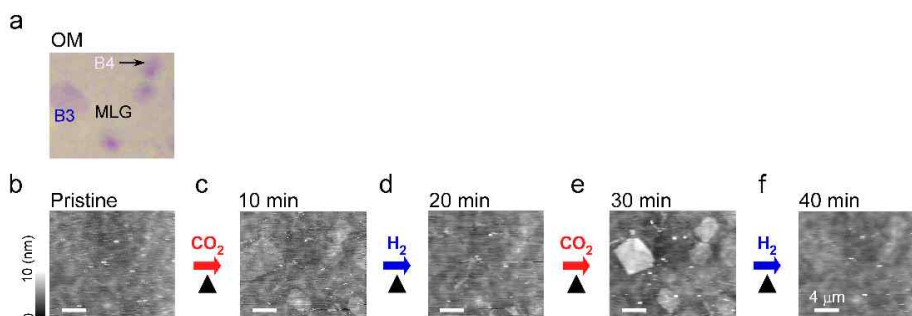


**Figure 7.1.9.** **a**, Optical reflectance microscopy (OM) image of CVD-grown multilayer graphene. **b**, AFM image of CVD-grown multilayer graphene. BLG (B3 and B4) and MLG are undistinguishable due to small topographic contrasts. **c**, AFM image of clearly visualized BLG after first CO<sub>2</sub>-loading due to volume expansion. **d**, AFM image of disappeared BLG under first H<sub>2</sub> exposure after **c**. **e**, AFM image of re-visualized BLG with higher expansion of B3 than B4 under second CO<sub>2</sub>-loading after **d**. **f**, AFM image of re-disappeared BLG under second H<sub>2</sub> exposure after **e**. All scale bars in AFM images are 4 μm.

In Figure 7.1.9, associated optical reflectance (OM) AFM images and more detailed images are presented to the sequential reaction time. The exact physical origin of such variation is unclear at the moment. Given that the major variation among the CVD-BLG islands in the same sample is the stacking angle between the two layers<sup>36,37</sup>, we hypothesize that the CO<sub>2</sub>-loading / unloading characteristics may be influenced by the stacking orders in few-layer graphene.

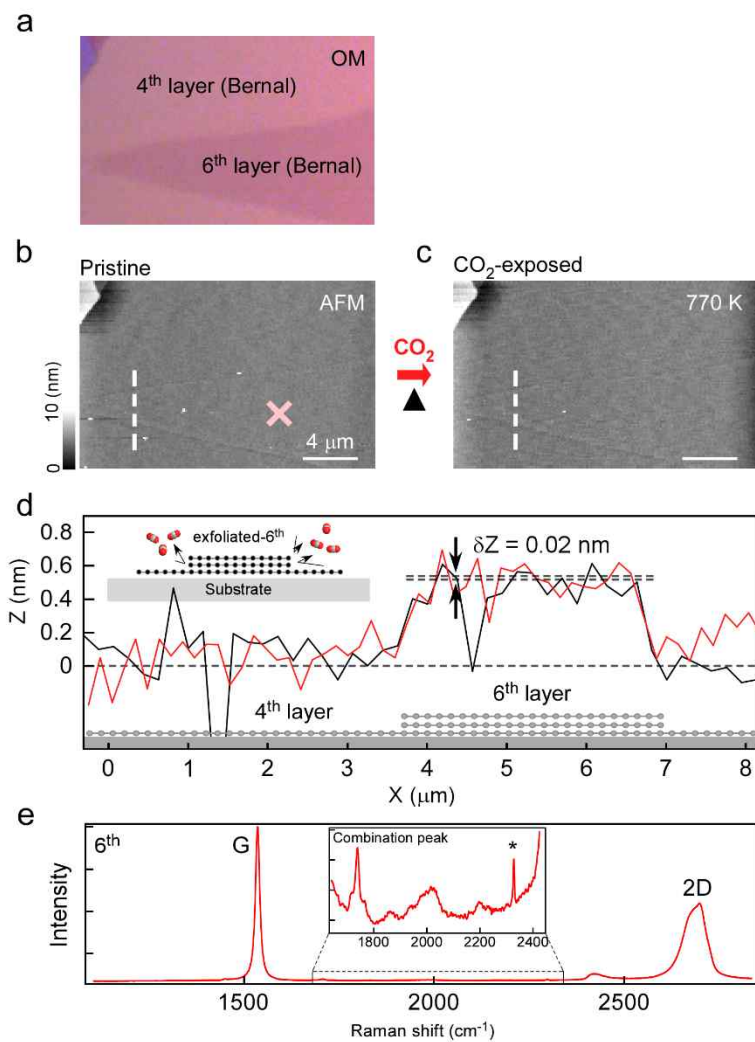


**Figure 7.1.10.** **a**, OM image of mechanically exfoliated 6<sup>th</sup> layer graphene on 4<sup>th</sup> layer graphene. **b**, AFM image of **a**. Raman spectrum of 6<sup>th</sup> layer graphene was measured at position X (magenta). **c**, AFM image of **a**, after CO<sub>2</sub>-loading showing no contrast change with **b**. All scale bars in AFM images are 4 μm. **d**, Line-profiles sampled from **b** & **c** (dashed lines in **b** & **c**). Thickness of the 6<sup>th</sup> layer graphene is indisputably unchanged. **e**, Wide range Raman spectrum of pristine 6<sup>th</sup> layer graphene. Inset shows combination-mode peaks of Raman spectrum of 6<sup>th</sup> layer graphene. The graphene sample is mechanically exfoliated from Kish graphite.

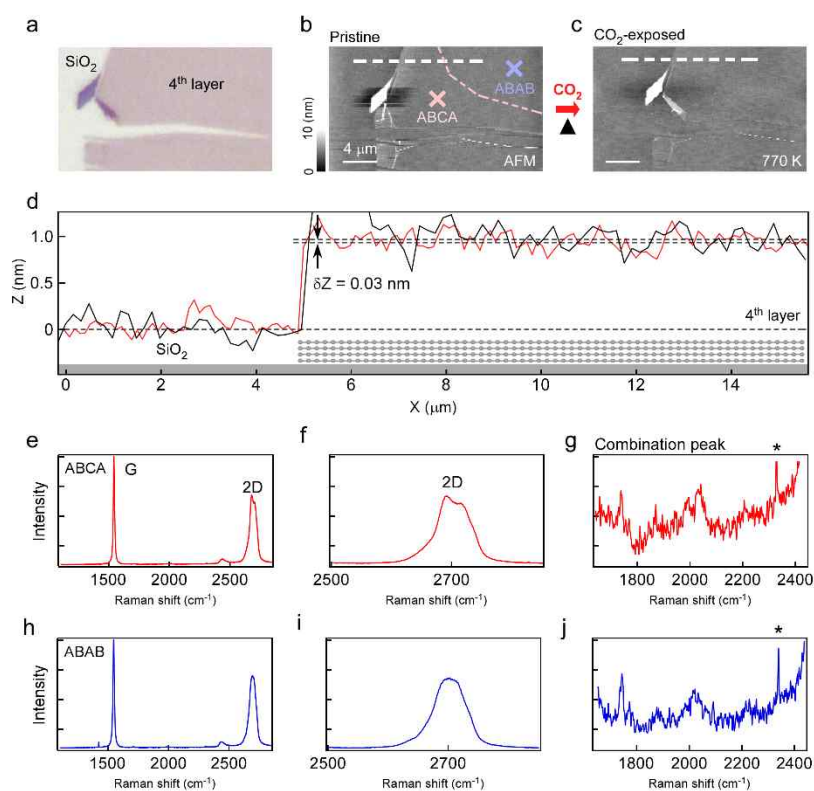


**Figure 7.1.11.** **a**, OM image of mechanically exfoliated 4<sup>th</sup> layer graphene. **b**, AFM image of **a**. Raman spectra of 4<sup>th</sup> layer graphene was measured at position X (magenta and blue). **c**, AFM image of **a**, after CO<sub>2</sub>-loading showing no contrast change with **b**. There was no topographic contrast change on 4<sup>th</sup> layer graphene, regardless of the stacking structure (Bernal or rhombohedral). All scale bars in AFM images are 4 μm. **d**, line-profiles sampled from **b** & **c** (dashed lines in **b** & **c**). Also, Thickness of the 4<sup>th</sup> layer graphene is essentially unchanged. **e** & **h**, Wide range Raman spectrum of pristine rhombohedral (ABCA) and Bernal (ABAB) stacking structure 4<sup>th</sup> layer graphene. **f** & **i**, 2D-peak of Raman spectrum of rhombohedral (ABCA) and Bernal (ABAB) stacking structure 4<sup>th</sup> layer graphene. **g** & **j**, Combination-mode peaks of Raman spectrum of rhombohedral (ABCA) and Bernal (ABAB) stacking structure 4<sup>th</sup> layer graphene. **j**, Although the 4<sup>th</sup> layer graphene have the same height, the Raman spectra of the two structures are different.

We have carried out the same experiment with mechanically exfoliated multilayer graphene that is mostly Bernal (ABAB) or rhombohedral (ABCA)-stacked (see Figure 7.1.10 and 11). We did not observe any sign of CO<sub>2</sub>-loading, corroborating our hypothesis.

Raman spectroscopy on CO<sub>2</sub>-loaded sample (B3 and MLG) reveal several features worth noting. First, the CO<sub>2</sub>-loading and unloading does not change the ratio

of intensities of D versus G-peaks ( $I_D / I_G$ ) or the intensity of D-peak ( $I_D$ ) (see Figures 6.1.8g), showing that the loading and unloading processes do not create additional defects.

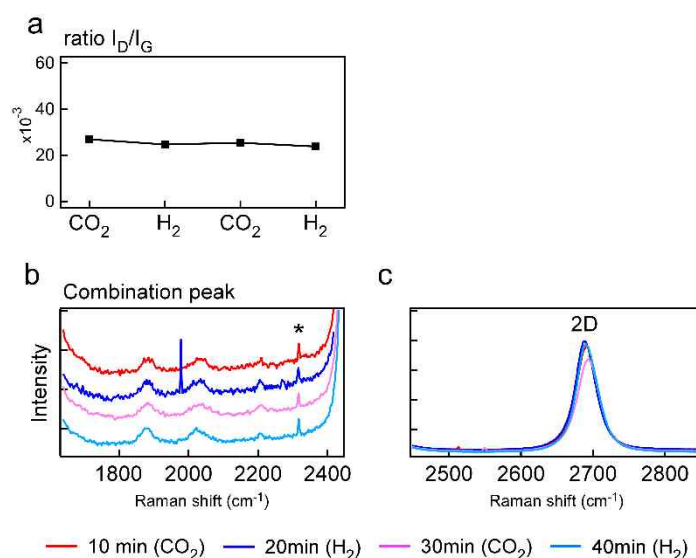


**Figure 7.1.12.** **a**, The intensity ratio of D versus G-peak ( $I_D / I_G$ ) obtained from the Raman spectra of CVD-BLG under  $\text{CO}_2$  and  $\text{H}_2$  exposure. The subtle change of  $I_D/I_G$  is considered as no generation of additional defect on CVD-BLG regardless of repetitive  $\text{CO}_2$  and  $\text{H}_2$  exposure. **b** & **c**, Raman spectra of CVD-BLG under  $\text{CO}_2$  and  $\text{H}_2$  exposure. Comparing to the continuously changed line-shape of the G-peak, no spectral change is observed at the combination-mode and 2D-peak. The peak at  $2331 \text{ cm}^{-1}$  (marked as \* in **b**) is assigned to symmetric mode of the ambient  $\text{N}_2$  gas.

Secondly, we have carried out  $\text{CO}_2$ -loading experiment on defective BLG islands showing pronounced  $I_D$  and  $I_D / I_G$  of Raman spectra (see Figure 7.1.12). We find that the amount of  $\text{CO}_2$ -loading is uncorrelated to the  $I_D$  or  $I_D / I_G$ , suggesting that the  $\text{CO}_2$  adsorption on defect (oxides, alcoholic functional groups, or structural defect) is not the main driving force of the  $\text{CO}_2$ -loading.

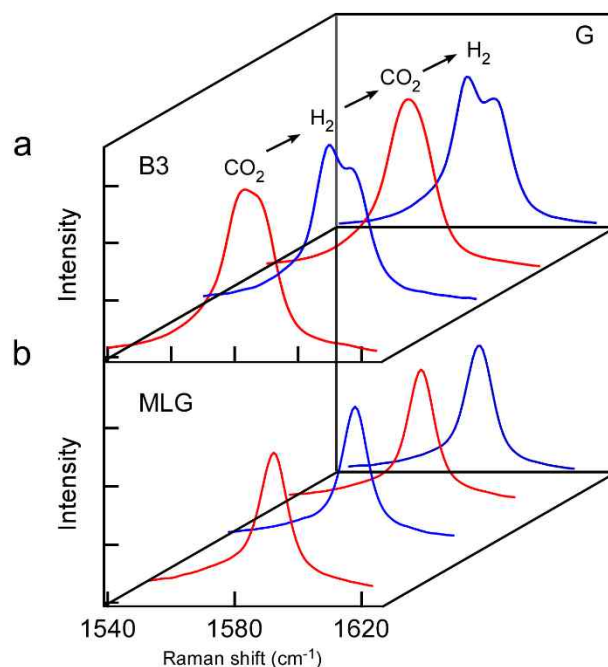


**Figure 7.1.13. a & b,** The G-peaks of Raman spectra obtained from Figure 7.1.8e (BLG and MLG).

Thirdly, the G-peak line-shape of the CO<sub>2</sub>-loaded BLG is unimodal (Figure 7.1.8f), which is distinctly different from the familiar bimodal line-shape of pristine and unloaded BLG. The center frequency of the G-peak is nearly unchanged ( $< 5 \text{ cm}^{-1}$ ). The change may arise from the chemical doping by CO<sub>2</sub>, or from the transformation of the electronic band structure of BLG into that of MLG upon increase in interlayer distance. Chemical doping always accompanies large peak-center shift ( $\geq 10 \text{ cm}^{-1}$ ) as well as the line-shape change in G-peak<sup>38</sup>, which contradicts what we observe. We thus hypothesize that it is the inter-layer distance change that is causing the line-shape change (Raman spectral changes of G-peak of MLG obtained from the position at the inset of Figure 7.1.8e (marked as X) in Figure 7.1.13).

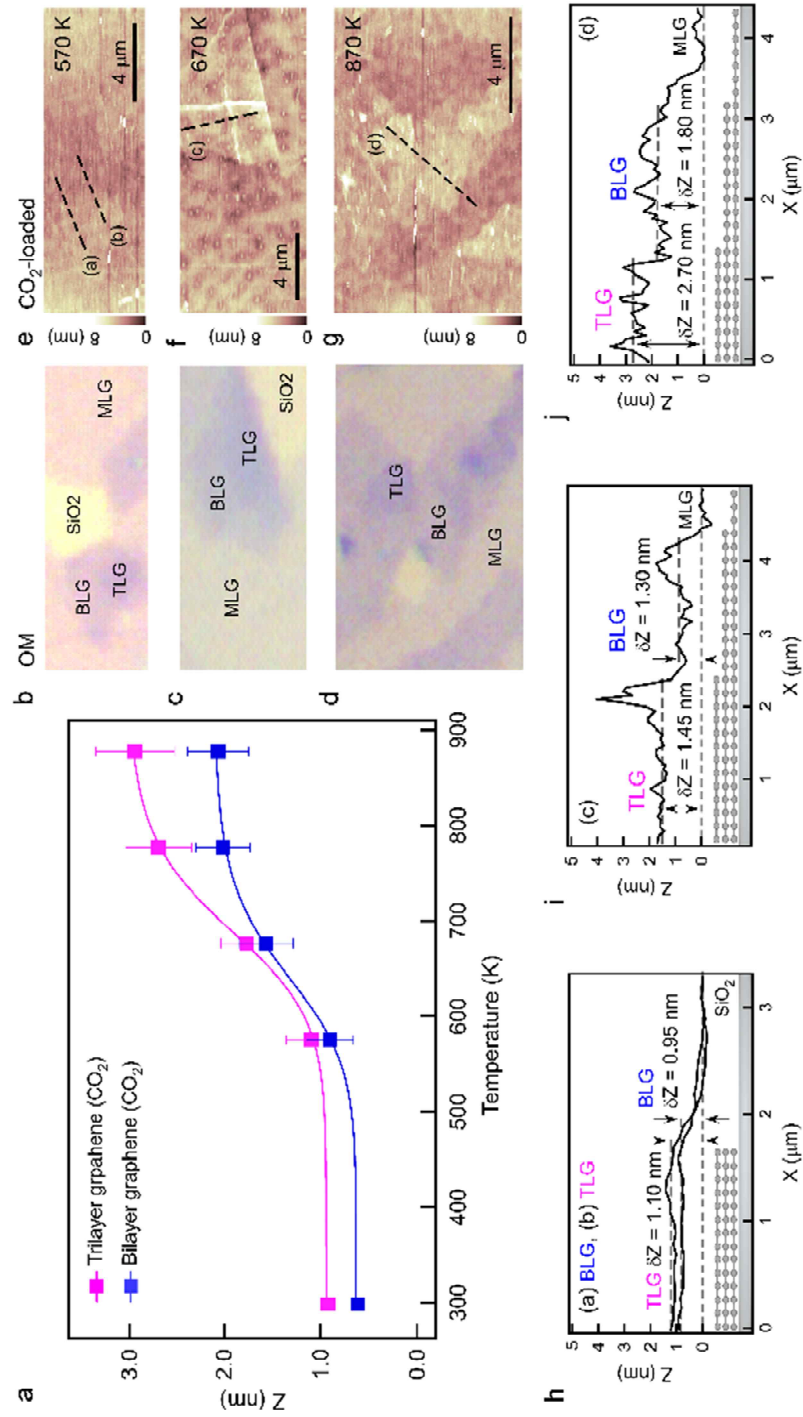


**Figure 7.1.14** **a**, The degree of height expansion ( $Z$ ) of BLG (blue) and TLG (magenta) at 4 different temperature. **b-d**, OM images and **e-g**, corresponding AFM images of CVD-grown multilayer graphene at **b, e** (570 K), **c, f** (670 K), and **d, g** (870 K). **h-j**, Line-profiles sampled from **e-g**, (dashed lines in (a)-(d)). All scale bars in AFM images are 4  $\mu\text{m}$ .

We believe that the CO<sub>2</sub>-loading / unloading is determined by the thermal activation of graphene layers, not by the adsorption of CO<sub>2</sub> onto the graphene surface: We have carried out the CO<sub>2</sub>-loading experiment under various temperature (see Figure 7.1.8i and temperature-dependent AFM images in Figure 7.1.14), and found that the amount of loading (i. e., the thickness of the BLG) *increases* with temperature, with a well-defined threshold temperature of 700 K for BLG and TLG. Note that the probability (or sticking coefficient) for the chemi- or physi-sorption of gas (the sticking coefficient) onto surface generally *decreases* with increasing temperature<sup>39,40</sup>, which is opposite to what is observed. Figure 7.1.16 show a model of CO<sub>2</sub>-capture by thermally activated graphene, in which thermal fluctuation in interlayer distance at the edges of the BLG allows the CO<sub>2</sub> to enter between the layers. Increase in sample temperature lowers the activation barrier, facilitating the CO<sub>2</sub>-insertion. The amount of inter-layer fluctuation and thus the activation energy for the insertion will correlate to how strongly the two layers are bound together<sup>31</sup>. For example, the layers of AA-BLG may fluctuate more than AB-BLG. This may explain the island-to-island variation in CO<sub>2</sub>-loading.

We were unable to directly quantify the amount of the captured CO<sub>2</sub> because the number of the captured CO<sub>2</sub> molecules is not nearly enough to be recorded by standard analytical tools. Nevertheless, we were able to obtain a preliminary surface-enhanced Raman scattering (SERS) spectra of the sample, showing features that could be assigned to the C-O stretching modes of the captured CO<sub>2</sub><sup>34,35,41</sup>. When exposed to CO<sub>2</sub>(g), the SERS spectrum of BLG sandwiched between a Cu-substrate and a Au-nanoparticle (Figure 7.1.4h inset) show new peaks at 1135 cm<sup>-1</sup> and 1370 cm<sup>-1</sup> (red arrows in Figure 7.1.8i), which are similar (both in

position and relative intensity) to the Fermi resonance doublet of C-O stretching peaks of solid CO<sub>2</sub> on Cu recorded at  $T = 40$  K<sup>32, 33</sup> (black and grey arrow).

Infrared (IR) reflection spectra of the sample before and after the CO<sub>2</sub>-loading do not clearly reveal the vibrational feature of the captured CO<sub>2</sub> (see Figure 7.1.8j for the TLG spectra). Instead, the spectra show reversible change in low-frequency side ( $< 900$  cm<sup>-1</sup>).

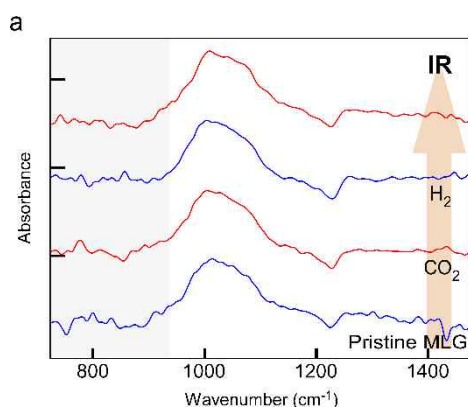


**Figure 7.1.15. a**, Infrared (IR) spectra of MLG upon alternating CO<sub>2</sub> and H<sub>2</sub> exposure.

No such spectral change is observed for MLG similarly exposed to CO<sub>2</sub> (see Figure 7.1.15). The low-frequency tail of the IR spectra of mono- and multi-layer graphene reflects the intra-band optical conductivity<sup>42,43</sup>, which can be modulated by adsorbed or intercalated molecules on graphene through the changes in doping level and electronic band structure. In this regard, the data not only corroborates our claim that the CO<sub>2</sub>-loading requires at least two layers of graphene, but it also shows a new possibility that the CO<sub>2</sub>-loading can tune the electronic and optical properties of graphene.

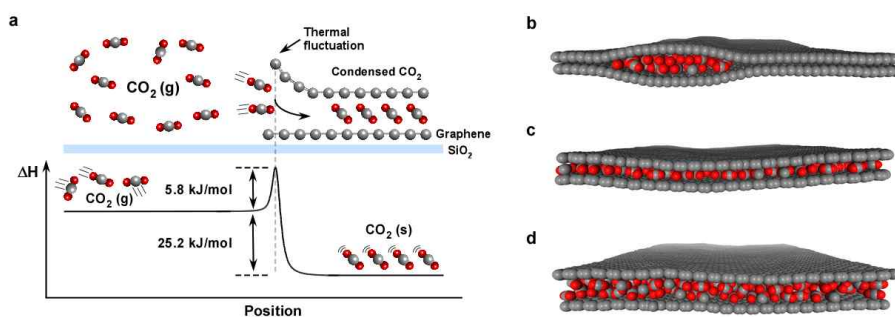


**Figure 7.1.16. Possible mechanism of CO<sub>2</sub> loading in BLG and MD simulation of CO<sub>2</sub> condensed form between graphenes depending on the number of CO<sub>2</sub> molecules.** **a**, Possible mechanism of CO<sub>2</sub> loading in BLG. **b-c**, MD simulation of CO<sub>2</sub> condensed form between graphenes depending on the number of CO<sub>2</sub> molecules. The CO<sub>2</sub> molecules used in the experiment are 300 (a), 500 (b) and 1000 (c). The size of graphene used in the simulation is 10.156 nm by 10.156 nm.

The amount of thickness change, and its temperature dependence cannot be explained by the CO<sub>2</sub> adsorption on graphene surface. Rather, all of our data consistently indicates the formation of multilayer (up to ~10 layer, assuming flat-on stacking geometry) CO<sub>2</sub>, which is mediated by the thermal activation of graphene. Given 1 GPa's of internal pressure between graphene layers, and known phase diagram of CO<sub>2</sub>, it is not unreasonable to assume that the captured CO<sub>2</sub> may be in the form of solid condensates. We have carried out a molecular dynamics (MD) simulation on CO<sub>2</sub> molecules embedded between the two layers of graphene. The primary aim of the simulation is to find out the structure of the captured CO<sub>2</sub> at room temperature. The simulation starts out with 100, 200, ..., 2000 number of CO<sub>2</sub> molecules with inter-molecular distance larger than 0.5, 1.0, ..., 2.0 nm, placed in between the graphene layers (see the right panel of Figure 7.1.16). As shown by the snapshot of the simulation, the captured CO<sub>2</sub> spontaneously form crystal-like clusters of CO<sub>2</sub> under the internal pressure of graphene. Note that the simulation employs generic force-field parameters of C and O atoms, and as such the simulation severely underestimates  $\pi$ - $\pi$  attraction between the layers. Therefore, we expect that MD

simulation with a more realistic force field will predict even more facile CO<sub>2</sub> condensation. The simulation, however, fails to model the introduction of CO<sub>2</sub> between the graphene layers through the edges of BLG.

#### 7.1.4 Conclusion

To conclude, we have shown that multilayers of CO<sub>2</sub> can be reversibly captured by CVD-grown BLG and TLG. The amount of CO<sub>2</sub>-loading increases with temperature. It has been previously assumed that CO<sub>2</sub> intercalation in graphene is an adsorption occurring on defects or functional groups, forming a monolayer or sub-monolayer of CO<sub>2</sub>. Our result shows that it is not the case. Rather, CO<sub>2</sub>-loading is mediated by the thermal fluctuation of graphene layers and also by the high-pressure induced condensation. Although we did not carry out the experiment on graphene oxides or functionalized graphene oxide, we do not see any reason why the intercalation mechanisms for graphene oxide and CVD-graphene should be different. It is unclear at the moment if the method can be scaled up such that it can sequester practical amount of CO<sub>2</sub> in atmosphere. The CO<sub>2</sub>-loading can modulate the inter-layer distance in BLG (up to 3 nm), thereby continuously tune its electronic band structure all the way from the BLG to two MLG. Currently, no existing technique can continuously tune the gap-distance in multilayer graphene. Our method may provide a new way of manipulating band structure of graphene for the graphene-based nanoelectronics devices and sensors.

## 7.1.5 References

- 1 Wu, Z. S., Parvez, K., Feng, X. & Müllen, K. Graphene-based in-plane micro-supercapacitors with high power and energy densities. *Nature Communications* **4**, 2487, doi:10.1038/ncomms3487 (2013).
- 2 Schwierz, F. Graphene transistors. *Nature Nanotechnology* **5**, 487-496, doi:10.1038/nnano.2010.89 (2010).
- 3 Yasaei, P. *et al.* Chemical sensing with switchable transport channels in graphene grain boundaries. *Nature Communications* **5**, 4911, doi:10.1038/ncomms5911 (2014).
- 4 Koppens, F. H. L. *et al.* Photodetectors based on graphene, other two-dimensional materials and hybrid systems. *Nature Nanotechnology* **9**, 780-793, doi:10.1038/nnano.2014.215 (2014).
- 5 Liang, Y. *et al.* Co<sub>3</sub>O<sub>4</sub> nanocrystals on graphene as a synergistic catalyst for oxygen reduction reaction. *Nature Materials* **10**, 780-786, doi:10.1038/nmat3087 (2011).
- 6 Hsu, H.-C. *et al.* Graphene oxide as a promising photocatalyst for CO<sub>2</sub> to methanol conversion. *Nanoscale* **5**, 262-268, doi:10.1039/C2NR31718D (2013).
- 7 Ghosh, A. *et al.* Uptake of H<sub>2</sub> and CO<sub>2</sub> by Graphene. *The Journal of Physical Chemistry C* **112**, 15704-15707, doi:10.1021/jp805802w (2008).
- 8 Ying, W. *et al.* Ionic Liquid Selectively Facilitates CO<sub>2</sub> Transport through Graphene Oxide Membrane. *ACS Nano* **12**, 5385-5393, doi:10.1021/acsnano.8b00367 (2018).
- 9 Yoon, H. W. *et al.* Origin of CO<sub>2</sub>-philic Sorption by Graphene Oxide Layered Nanosheets and Their Derivatives. *The Journal of Physical Chemistry Letters* **11**, 2356-2362, doi:10.1021/acs.jpcllett.0c00204 (2020).
- 10 Li, X. *et al.* Enhanced NH<sub>3</sub>-Sensitivity of Reduced Graphene Oxide Modified by Tetra- $\alpha$ -Iso-Pentylloxymetallophthalocyanine Derivatives. *Nanoscale research letters* **10**, 373-373, doi:10.1186/s11671-015-1072-3 (2015).
- 11 Novikov, S. *et al.* Graphene based sensor for environmental monitoring of

- NO<sub>2</sub>. *Sensors and Actuators B: Chemical* **236**, 1054-1060, doi:<https://doi.org/10.1016/j.snb.2016.05.114> (2016).
- 12 Ren, Y. *et al.* Detection of sulfur dioxide gas with graphene field effect transistor. *Applied Physics Letters* **100**, 163114, doi:10.1063/1.4704803 (2012).
- 13 Shin, D. *et al.* Growth dynamics and gas transport mechanism of nanobubbles in graphene liquid cells. *Nature Communications* **6**, 6068, doi:10.1038/ncomms7068 (2015).
- 14 Cervený, S., Barroso-Bujans, F., Alegría, Á. & Colmenero, J. Dynamics of Water Intercalated in Graphite Oxide. *The Journal of Physical Chemistry C* **114**, 2604-2612, doi:10.1021/jp907979v (2010).
- 15 Kim, H. *et al.* Aqueous Rechargeable Li and Na Ion Batteries. *Chemical Reviews* **114**, 11788-11827, doi:10.1021/cr500232y (2014).
- 16 Manthiram, A., Chung, S.-H. & Zu, C. Lithium–Sulfur Batteries: Progress and Prospects. *Advanced Materials* **27**, 1980-2006, doi:10.1002/adma.201405115 (2015).
- 17 Ji, K. *et al.* Lithium intercalation into bilayer graphene. *Nature Communications* **10**, 275, doi:10.1038/s41467-018-07942-z (2019).
- 18 Fu, Q. & Bao, X. Surface chemistry and catalysis confined under two-dimensional materials. *Chem. Soc. Rev.* **46**, 1842-1874, doi:10.1039/C6CS00424E (2017).
- 19 Algara-Siller, G. *et al.* Square ice in graphene nanocapillaries. *Nature* **519**, 443-445, doi:10.1038/nature14295 (2015).
- 20 Yuk, J. M. *et al.* High-Resolution EM of Colloidal Nanocrystal Growth Using Graphene Liquid Cells. *Science* **336**, 61, doi:10.1126/science.1217654 (2012).
- 21 Narayanan, S. *et al.* On the structure and chemistry of iron oxide cores in human heart and human spleen ferritins using graphene liquid cell electron microscopy. *Nanoscale* **11**, 16868-16878, doi:10.1039/C9NR01541H (2019).
- 22 Rodríguez-García, S. *et al.* Role of the Structure of Graphene Oxide Sheets on the CO<sub>2</sub> Adsorption Properties of Nanocomposites Based on Graphene Oxide and Polyaniline or Fe<sub>3</sub>O<sub>4</sub>-Nanoparticles. *ACS Sustainable Chemistry*

- & *Engineering* **7**, 12464-12473, doi:10.1021/acssuschemeng.9b02035 (2019).
- 23 Khajeh, M. & Ghaemi, A. Nanoclay montmorillonite as an adsorbent for CO<sub>2</sub> capture: Experimental and modeling. *Journal of the Chinese Chemical Society* **67**, 253-266, doi:10.1002/jccs.201900150 (2020).
- 24 Loring, J. S. *et al.* In Situ Molecular Spectroscopic Evidence for CO<sub>2</sub> Intercalation into Montmorillonite in Supercritical Carbon Dioxide. *Langmuir* **28**, 7125-7128, doi:10.1021/la301136w (2012).
- 25 Bhatti, U. H. *et al.* Practical and inexpensive acid-activated montmorillonite catalysts for energy-efficient CO<sub>2</sub> capture. *Green Chemistry*, doi:10.1039/D0GC01887B (2020).
- 26 Snæbjörnsdóttir, S. Ó. *et al.* Carbon dioxide storage through mineral carbonation. *Nature Reviews Earth & Environment* **1**, 90-102, doi:10.1038/s43017-019-0011-8 (2020).
- 27 Kim, D. *et al.* Intercalation of Gas Molecules in Graphene Oxide Interlayer: The Role of Water. *The Journal of Physical Chemistry C* **118**, 11142-11148, doi:10.1021/jp5026762 (2014).
- 28 Xu, H. *et al.* Highly selective electrocatalytic CO<sub>2</sub> reduction to ethanol by metallic clusters dynamically formed from atomically dispersed copper. *Nature Energy* **5**, 623-632, doi:10.1038/s41560-020-0666-x (2020).
- 29 Enejekwu, F. M. *et al.* A comparative study of mechanisms of the adsorption of CO<sub>2</sub> confined within graphene–MoS<sub>2</sub> nanosheets: a DFT trend study. *Nanoscale Advances* **1**, 1442-1451, doi:10.1039/C8NA00314A (2019).
- 30 Lee, H. & Park, J. Y. Height determination of single-layer graphene on mica at controlled humidity using atomic force microscopy. *Review of Scientific Instruments* **90**, 103702, doi:10.1063/1.5098483 (2019).
- 31 Berashevich, J. & Chakraborty, T. On the Nature of Interlayer Interactions in a System of Two Graphene Fragments. *The Journal of Physical Chemistry C* **115**, 24666-24673, doi:10.1021/jp2095032 (2011).
- 32 Dagdeviren, O. E. & Schwarz, U. D. Accuracy of tip-sample interaction measurements using dynamic atomic force microscopy techniques: Dependence on oscillation amplitude, interaction strength, and tip-sample distance. *Review of Scientific Instruments* **90**, 033707,

- doi:10.1063/1.5089634 (2019).
- 33 Hölscher, H. Quantitative measurement of tip-sample interactions in amplitude modulation atomic force microscopy. *Applied Physics Letters* **89**, 123109, doi:10.1063/1.2355437 (2006).
- 34 Lust, M., Pucci, A., Akemann, W. & Otto, A. SERS of CO<sub>2</sub> on Cold-Deposited Cu: An Electronic Effect at a Minority of Surface Sites. *The Journal of Physical Chemistry C* **112**, 11075-11077, doi:10.1021/jp8032403 (2008).
- 35 Akemann, W. & Otto, A. Roughness induced reactions of N<sub>2</sub> and CO<sub>2</sub> on noble and alkali metals. *Surface Science* **272**, 211-219, doi:[https://doi.org/10.1016/0039-6028\(92\)91441-D](https://doi.org/10.1016/0039-6028(92)91441-D) (1992).
- 36 Chen, Y.-C. *et al.* Direct growth of mm-size twisted bilayer graphene by plasma-enhanced chemical vapor deposition. *Carbon* **156**, 212-224, doi:<https://doi.org/10.1016/j.carbon.2019.09.052> (2020).
- 37 Pezzini, S. *et al.* 30°-Twisted Bilayer Graphene Quasicrystals from Chemical Vapor Deposition. *Nano Letters* **20**, 3313-3319, doi:10.1021/acs.nanolett.0c00172 (2020).
- 38 Liu, L. *et al.* Graphene Oxidation: Thickness-Dependent Etching and Strong Chemical Doping. *Nano Letters* **8**, 1965-1970, doi:10.1021/nl0808684 (2008).
- 39 Mishra, A. K. & Ramaprabhu, S. Carbon dioxide adsorption in graphene sheets. *AIP Advances* **1**, 032152, doi:10.1063/1.3638178 (2011).
- 40 Li, W., Yang, H., Jiang, X. & Liu, Q. Highly selective CO<sub>2</sub> adsorption of ZnO based N-doped reduced graphene oxide porous nanomaterial. *Applied Surface Science* **360**, 143-147, doi:<https://doi.org/10.1016/j.apsusc.2015.10.212> (2016).
- 41 Akemann, W. & Otto, A. The effect of atomic scale surface disorder on bonding and activation of adsorbates: vibrational properties of CO and CO<sub>2</sub> on copper. *Surface Science* **287-288**, 104-109, doi:[https://doi.org/10.1016/0039-6028\(93\)90751-5](https://doi.org/10.1016/0039-6028(93)90751-5) (1993).
- 42 Santos, C. N. *et al.* Terahertz and mid-infrared reflectance of epitaxial graphene. *Scientific Reports* **6**, 24301, doi:10.1038/srep24301 (2016).
- 43 Hao, L. & Sheng, L. Optical conductivity of multilayer graphene. *Solid State*



# 국문 초론

## 적외선 산란형 근접장 주사 광학 현미경을 이용한 그래핀 표면위 화학 반응 연구

서울대학교 대학원

화학부 물리화학전공

정규일

본 논문은 주사탐침현미경 기반의 적외선 산란형 근접장 주사 광학 현미경 (IR-sSNOM)을 사용하여 그래핀 표면 위 화학반응에 중점을 둔다.

그래핀 표면의 물리적 및 화학적 고유한 특성에 대해 다양한 연구가 수행되어 왔다. 이러한 발전과 함께, 특히 손쉽게 다층 그래핀의 겹쳐진 각도나 외부에서 인가되는 전기장 또는 화학적 불순물 추가를 통해 띠 간격 조절이 가능해 각광을 받아왔다. 그러나 이런 그래핀의 특성을 분석하는데 사용되는 일반적인 적외선 분광 기법에는 치명적인 한계가 있다. 아베 회절 한계로 인해 그래핀 표면의 나노 화학 반응을 연구

하는 것이 불가능하다. 유감스럽게도 그래핀분석에 가장 많이 활용되는 라만 분광 기법에도 동일한 문제가 있다. 또한 이 라만 분광 기법은 D, G 및 2D 대역 스펙트럼의 변화만 감지하므로 직접적인 화학 분자의 정보를 알지 못한다.

이러한 관점에서 저는 두가지의 목표로 이 연구를 진행하고자 한다. 첫째, 분광학적 시각에서 적외선 산란형 근접장 주사 광학 현미경은 고감도의 나노 해상도를 가지는 것으로 잘 알려져 있다. 이 분광 기기를 이용하면 그래핀 10um 미만의 영역의 IR 스펙트럼을 얻을 수 있다. 또한 주사 터널 현미경과 달리 시료 조건에 큰 제한이 없다. 이러한 점에서 이 적외선 산란형 근접장 주사 광학 현미경은 그래핀 표면 위 반응을 분석하는데 이상적인 도구이다. 둘째, 이러한 그래핀 표면 반응 연구는 유기 화학의 원형 모델이 될 뿐만 아니라 그래핀의 전자 응용으로 연구 할 가치가 있다. 이 유기 화학의 원형 모델 시스템 연구를 통해 pi-pi 상호 작용의 메커니즘뿐만 아니라 그래핀 촉매 메커니즘에 대해 이해할 수 있을 것이다. 이러한 그래핀 표면 반응을 연구를 통해 화학 분야에 새로운 통찰력을 가져올 것이라고 확신한다

**주요어** : 적외선 산란형 근접장 주사 광학 현미경, 플라즈몬, 그래핀, 무아래 패턴, 산화환원 반응, 이산화탄소 증간 삽입

**학 번** : 2014-21226